Old Dominion University

ODU Digital Commons

External Aerodynamics of Heavy Ground Vehicles: Computations and Wind Tunnel Testing

Ilhan Bayraktar
Old Dominion University

Recommended Citation

EXTERNAL AERODYNAMICS OF HEAVY GROUND VEHICLES:

COMPUTATIONS AND WIND TUNNEL TESTING

by

Ilhan Bayraktar
B.S.M.E., June 1995, Istanbul Technical University
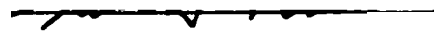M.S.M.E., March 1998, Istanbul Technical University

A Dissertation Submitted to the Faculty of
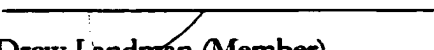Old Dominion University in Partial Fulfillment of the
Requirements for the Degree of

DOCTOR OF PHILOSOPHY
AEROSPACE ENGINEERING

OLD DOMINION UNIVERSITY
May 2002

Approved by:

Oktay Baysal (Director)

Osama A. Kandil (Member)

Drew Landman (Member)

John C. Lin (Member)

ABSTRACT

EXTERNAL AERODYNAMICS OF HEAVY GROUND VEHICLES: COMPUTATIONS AND WIND TUNNEL TESTING

Ilhan Bayraktar
Old Dominion University, 2002
Director: Dr. Oktay Baysal

Aerodynamic characteristics of a ground vehicle affect vehicle operation in many ways. Aerodynamic drag, lift and side forces have influence on fuel efficiency, vehicle top speed and acceleration performance. In addition, engine cooling, air conditioning, wind noise, visibility, stability and crosswind sensitivity are some other tasks for vehicle aerodynamics. All of these areas benefit from drag reduction and changing the lift force in favor of the operating conditions. This can be achieved by optimization of external body geometry and flow modification devices. Considering the latter, a thorough understanding of the airflow is a prerequisite.

The present study aims to simulate the external flow field around a ground vehicle using a computational method. The model and the method are selected to be three dimensional and time-dependent. The Reynolds-averaged Navier Stokes equations are solved using a finite volume method. The Renormalization Group (RNG) k-ε model was elected for closure of the turbulent quantities. Initially, the aerodynamics of a generic bluff body is studied computationally and experimentally to demonstrate a number of relevant issues including the validation of the computational method. Experimental study was conducted at the Langley Full Scale Wind Tunnel using pressure probes and force measurement equipment. Experiments and computations are conducted on several

geometric configurations. Results are compared in an attempt to validate the computational model for ground vehicle aerodynamics.

Then, the external aerodynamics of a heavy truck is simulated using the validated computational fluid dynamics method, and the external flow is presented using computer visualization. Finally, to help the estimation of the error due to two commonly practiced engineering simplifications, a parametric study on the tires and the moving ground effect are conducted on full-scale tractor-trailer configuration. Force and pressure coefficients and velocity distribution around tractor-trailer assembly are computed for each case and the results compared with each other.

Finally, this study demonstrates that it is possible to apply computational fluid dynamics for ground vehicle aerodynamics with substantial detail and fidelity. With the latest developments on computing power, computational fluid dynamics can be applied on real-life transportation problems with reasonable turn-around times, reliability, ease of accessibility and affordability. The next step is deemed to be considering such a computational methodology for analysis within an automated optimization process in improving aerodynamic designs of heavy ground vehicles.

ACKNOWLEDGMENTS

I would like to express gratitude and appreciation to my advisor Dr. Oktay Baysal for his invaluable guidance, encouragement and advice throughout the entire course of this study. I wish to sincerely thank my guidance and dissertation committee members, Dr. Osama Kandil, Dr. Drew Landman and Dr. John C. Lin for their valuable time and suggestions.

I also acknowledge the support of Langley Full Scale Wind Tunnel (LFST) and I am very thankful to everybody who works there. This dissertation would not be complete without experimental data that I got from there.

I am grateful to all my family members and especially to my wife, Tuba Bayraktar, whose support and encouragement have always been a source of inspiration for me.

Finally, I would like to thank all of my colleagues, especially Bulent Imamoglu and Ilker Turkgeldi, for their friendship and support.

Ilhan Bayraktar

May 2002

TABLE OF CONTENTS

LIST OF TABLES

LIST OF FIGURES

LIST OF SYMBOLS

[A]   coefficient matrix

$C_{\varepsilon_1}, C_{\varepsilon_2}$ coefficients used in k-ε calculation

C_D drag coefficient

C_L lift coefficient

E   total energy

H   stagnation enthalpy

I   turbulence intensity

k   kinetic energy constant

$\dot{m}_{ip}$ mass transfer between integration points

$\hat{n}_j$ surface outward normal vector

N_x normal force along the x-axis (longitudinal axis)

N_z normal force along the z-axis (vertical axis)

p' first derivative of pressure

P   Pressure

S_E energy equation constant

S_M momentum equation constant

t time

u x-component of velocity

U velocity

U_i velocity subscript array variable j

$\overline{U}$ average velocity

v y-component of velocity

w z-component of velocity

x_j location with subscript array variable j

$[X]$ solution vector

Greek Symbols

α backlight angles

β blending term used to improve the accuracy of the upwind difference scheme

Γ circulation

ε dissipation constant

μ_t eddy viscosity

μ_{eff} effective viscosity

ρ density

σ shear

σ_ε dissipation shear constant

σ_k kinetic energy shear constant

ϕ arbitrary variable for demonstration of discretization

ϕ_{ip} arbitrary variable evaluated at integration point

ϕ_n arbitrary variable defined at node n

ϕ_{NAC} arbitrary variable corrected with the numerical advection term

Other Symbols

$\otimes$ tensor product

∇ gradient operator

Δ delta operator

Acronyms

CAD   computer aided drafting

CFD   computational fluid dynamics

CPU   central processing unit

GUI   graphical user interface

ILU   incomplete lower upper

LES   large eddy simulation

LFST   Langley Full-Scale wind Tunnel

MG   multigrid

MPI   message passing interface

MPICH   message passing interface chameleon

NAC   numerical advection correction

NASA   National Aeronautics and Space Administration

QUICK   quadratic upwind interpolation for convective kinematics

RANS   Reynolds averaged Navier-Stokes

RMS   root mean square

RSM   reynolds stress model

RSM   Reynolds stress model

SSG   nonlinear model of Speziale, Sarkar and Gatski,

SST   shear stress transport

UDS   upwind difference scheme

CHAPTER 1

INTRODUCTION†

1.1   GROUND VEHICLE AERODYNAMICS

One of the objectives considered in designing the new generation heavy trucks is fuel efficiency. This can be achieved by improving the combustion process in the diesel engine and by reducing the overall drag force on the truck in motion. Considering the latter, a thorough understanding of the airflow, both in and around the truck, is necessary.

The fluid flow in and around a ground vehicle in motion may be grouped into the following two major categories. The external flow includes the undercarriage flow, the flow in the gap between the tractor and the trailer(s) and the wake behind the truck. The external flow is estimated to be responsible for about 85% of the drag force. It generates the wake that the nearby road vehicles experience and carries the splashed water or mud to the truck's immediate vicinity. The internal flows include the under-the-hood flow and the flow inside the cabin. The airflow that enters through the front grill starts the under-the-hood flow; after it cools the engine block, it is diverted by the bulkhead to the wheel wells.

Both the external and the internal flows are highly turbulent, dominated by large separation regions, large and small vortices and complex recirculation regions (Hucho, 1998). Due to one or more of the aforementioned factors, some of these flows are also unsteady. Therefore, they require time-accurate solutions of the viscous-flow equations on computational domains with moving boundaries or even dynamic meshes (Baysal, 1999, Baysal and Luo, 1999,).

---

† The format of this dissertation is based on the *ASME Journal of Fluids Engineering*.

Bluff body flows get attention in many areas in vehicle design, missile configuration and building and railroad aerodynamics. In addition, it is necessary in many vehicle designs to lessen the length to reduce weight. Furthermore, it is essential in ground vehicle aerodynamics to satisfy a design principle, which is the maximum utilization of the enclosed vehicle volume. Because of this design concept, bluff body shapes widely appear in many cases.

Bluff body wakes are of particular interest as low pressures can develop in this region, resulting in base drag that can be a significant portion of the total body drag. Drag force, which is generated by the vortices behind a bluff body, is also time dependent. If the frequency of this unsteady force matches with the natural frequency of the bluff body, it can induce noise and vibration. Flow induced vibration of the bluff body can take the form of vortex resonance, galloping or flutter depending on the flow conditions and geometry of the body. Therefore, studying of such flow structures is important to the design of safe products.

Most of the studies into subsonic bluff body flows (square and circular cylinder studies) are simple two-dimensional configurations. Many practical engineering problems, such as heat exchanger flows, can be analyzed in two dimensions; however, many wake flows require three-dimensional analysis. For example, ground vehicles, buildings and aircraft fuselage design require axisymmetric or a three dimensional analysis.

The flowfield around a ground vehicle, which is being investigated in this study, is a three dimensional, turbulent and unsteady phenomenon. Typical tractor-trailer configurations produce several stagnation points, separations, secondary flow regions and large wakes. In addition, under-the-hood and underbody flows make the external flowfield

even more difficult to handle. These all increase the total vehicle drag coefficient and eventually influence the fuel consumption unfavorably.

It has been reported that heavy trucks consume approximately 68% of all commercial truck fuel used in United States, even though they comprise less than 17% of the commercial vehicle fleet. Nearly 70% of the fuel consumption of these heavy trucks occurs during trips longer than 100 miles (Bradley, 2000). Therefore, the heavy trucks stand to benefit most from any technology that will improve fuel efficiency.

Fuel consumption for heavy trucks can be reduced by external shape modification. Aerodynamically improved external geometry decreases the drag force on the vehicle in motion. Characteristics of such vehicle aerodynamics can be itemized as follows; (i) Heavy trucks have a relatively high drag coefficient, which is usually greater than 0.5 (Bradley, 2000), (ii) they have large frontal areas (iii) and they are operated mostly at highway speeds. Detailed research in these areas could lead to drag reduction and considerable fuel savings.

There are numerous studies that have been conducted either with entire trucks or local geometries and their resulting flow characteristics. Until recently, most of these studies have been based upon wind tunnel experiments. This is mainly because there was no better method available for a long time. Therefore, most of the design improvements were achieved from these limited quantitative data from traditional methods. Recent improvements on computer speed and architecture provide a new opportunity for the aerodynamic development of ground vehicles. However, most computational methods have yet to be proven on ground vehicle aerodynamics.

1.2   MOTIVATION AND OBJECTIVE OF THE STUDY

Road vehicles are the most common transportation utilities on Earth. There are millions of road vehicles that are used to transport of people and goods everyday. Almost all

of these vehicles consume petroleum products, which are not renewable and will be depleted in the future. Therefore, the primary motivation for this study is fuel efficiency.

Fuel efficiency can be obtained by not only improving the combustion process, but also reducing the overall aerodynamic resistance of the vehicle in motion. In addition, a lowered aerodynamic resistance increases vehicle acceleration capability and the top speed. Aerodynamic characteristics also play an important role in vehicle control, stability, wind noise, interaction with other vehicles and road safety.

Every type of road vehicle uses aerodynamics in different ways. For example, NASCAR class racecars use spoilers on the rear end to gain an aerodynamic advantage. They even use another cars' wake to lessen drag. Open wheel racecars like NASCAR cars also have wings, strakes, wickers and many other aerodynamic devices. They typically use aerodynamics to increase negative lift and improve vehicle stability at high speed (Katz, 1995). In contrast, passenger cars, vans and trucks are not designed for negative lift. The aerodynamic design goal for those kind of vehicles is to reduce the drag force. Therefore, they are not associated with such aerodynamic devices. Moreover, solar cars present another interesting aerodynamic design objective. Since their top velocity is relatively low, they are built on a zero-lift principle, and unlike passenger cars, drag minimization is the primary variable for optimizing the external geometry (Hucho, 1998).

Historically, aerodynamics has not been a big concern in the vehicle design process. Increasing fuel prices and environmental pollution have made aerodynamics more important in the last half of the 20th century. First improvement was accomplished by moving from a carriage-like body to a three-volume body (pontoon) with reduction of the drag coefficient from $c_D \approx 0.8$ to $c_D \approx 0.45$. The next development in drag reduction started at the beginning of the 1970s. The first oil crisis during the winter of 1973-74 made the automobile industry

ready to accept arguments from aerodynamicists, and so a trend to lower drag became rather pronounced. Presently, an average mid-size car has $c_D \approx 0.30$ value and it is believed that this value still can be improved by applying basic aerodynamic principles (Hucho, 1993).

The objectives of this dissertation are to investigate the principles in ground vehicle aerodynamics and simulate the external flow using a computational method. Efforts are especially directed towards code validation, force coefficient calculation, rear end vehicle configuration and full-scale heavy truck simulation. This dissertation is founded on numerical calculations; however, an attempt at wind tunnel verification is also made.

The first part of the present study is a continuation of previous bluff body research in vehicle aerodynamics. Previous bluff body research, which is discussed in Chapter 2, addresses the relationship between drag coefficient and rear end vehicle configuration. The present study examines this relationship in detail using a Computational Fluid Dynamics method. Later, the same method will be applied to a full-scale heavy tractor-trailer configuration. A parametric study is conducted to understand the effects of a moving ground and tires. Results are presented using numerical visualization techniques and compared with each other.

1.3 ROADMAP OF DISSERTATION

This dissertation is structured in seven chapters. The background, a short description of the methodology, motivation and objectives have been presented in this chapter. Chapter 2 is devoted to literature survey, a detailed review of the research work conducted in the area. Chapter 3 briefly discusses the numerical tools, solution procedure and turbulence modeling that are being used in this dissertation. Then, Chapters 4 and 5 investigate bluff body aerodynamics on an Ahmed Body. Presented in Chapter 4 are the experimental measurements from the wind tunnel, and in Chapter 5 the numerical results and their

comparison with experimental measurements are provided. Chapter 6 investigates heavy truck aerodynamics using this methodology. Finally, conclusions of the present study and recommendations for future enhancement of the work are given in Chapter 7.

CHAPTER 2

LITERATURE SURVEY

The first vehicle that moved by its own gasoline power was built more than 100 years ago. The people who built it certainly did not think about aerodynamics; interest in the aerodynamic design of road vehicles developed much later. The first efforts to modify automobile aerodynamics were simply to transfer shapes from naval and aeronautical applications. These efforts could not succeed mainly because the approach of directly transplanting (with almost no change) shapes that had been developed for aeronautical and marine purposes was not suitable. There were different functional, economical and aesthetic design concepts involved in ground vehicle design. In addition, aerodynamic benefits were not needed at that time. Those preliminary modifications could only be adapted if some important changes in car design were considered together, e.g., engine location, or layout of the passenger compartment.

Development of ground vehicle aerodynamics in the automobile industry has been discussed in many articles (Gleason et al. 1998, Hucho 1998, Sumantran et al. 1995). Therefore, acknowledging the danger of being superficial, only critical events in the past will be highlighted. If we outline them in chronological order:

1.   First, Klemperer (1922) recognized that the pattern of flow around half a body of revolution is significantly changed when that half body is brought close to the ground in 1922 (Figure 2.1).

2.   Kamm et al. (1934) and Koenig-Fachsenfeld (1951) conducted rear body end truncation studies.

3. Hucho et al. (1976) introduced "detailed optimization" into vehicle development.

4. Morel (1978) and Ahmed et al. (1984) investigated detailed flow patterns at car rear ends.

5. T. Han (1989) implemented CFD methods to ground vehicle aerodynamics.

6. Today, aerodynamic design analysis on "add-on" devices such as mirrors, air dams, fairings and wings to passenger cars, trucks and race cars are getting attention.

With these six steps, aerodynamics has been implemented in the vehicle design procedure.
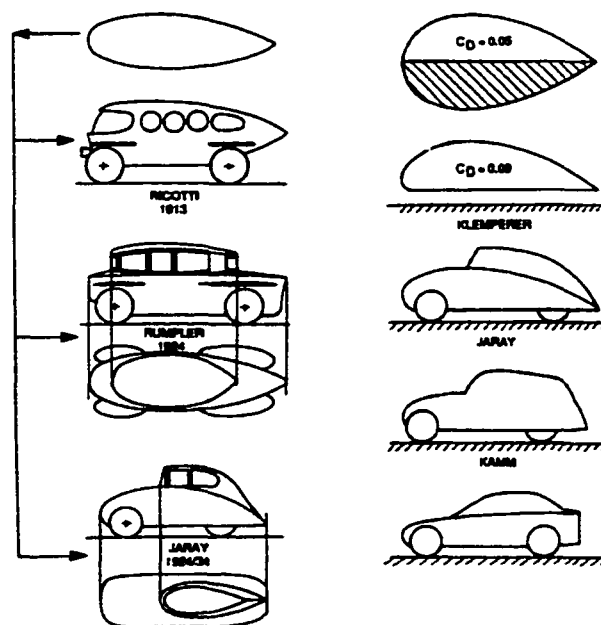
Figure 2.1. Historical development of vehicle aerodynamics (with permission, from the Annual Review of Fluid Mechanics, Volume 25, ©1993, by Annual Reviews www.AnnualReviews.org).

Figure 2.1 shows first examples of early aerodynamic studies. In the first half of the century, vehicle aerodynamicists worked on streamlining the cars. Many streamlined vehicles

were tested under impression of marine and aviation applications (Hucho and Sovran, 1993). In the 1930s, a parametric study on front and rear end configurations and their interactions was investigated by Lay (1933). That study revealed a strong interaction between front and rear end design. Therefore, front and rear end configurations got most of the attention at the time. In the 1960s, detail optimization was introduced to reduce the drag force by modifying small components on the vehicle. Details such as radii of edges and pillars, camber of panels and size and location of spoilers were changed and significant results were obtained (Hucho, 1998). In the 1970s, total shape optimization also came into the play. In this optimization process, the aerodynamic development starts on the main dimensions of vehicle, such as length, height and width, and then goes through the external shaping process. In day-to-day operations, of course these two optimization strategies could not be strictly separated. Actually, today both detail and shape optimization strategies are successfully used on the aerodynamic vehicle development process.

Higher fuel price, increased operation speed in average and higher comfort standards have made aerodynamics an even more important design variable than before. Current fuel prices are much higher than those of 50 years ago, and average road vehicle speed has been doubled in the last 40 years. Although high operating speed increases aerodynamic forces exponentially, drag coefficient has dropped in half in last five decades. Figure 2.2 shows average drag coefficient change for ground vehicles in the last century. User comfort has also played a role in this aerodynamic improvement. Wind noise has become as important issue as engine noise at high speed. Quiet, fuel-efficient and environment friendly production vehicles have become more attractive in these days.
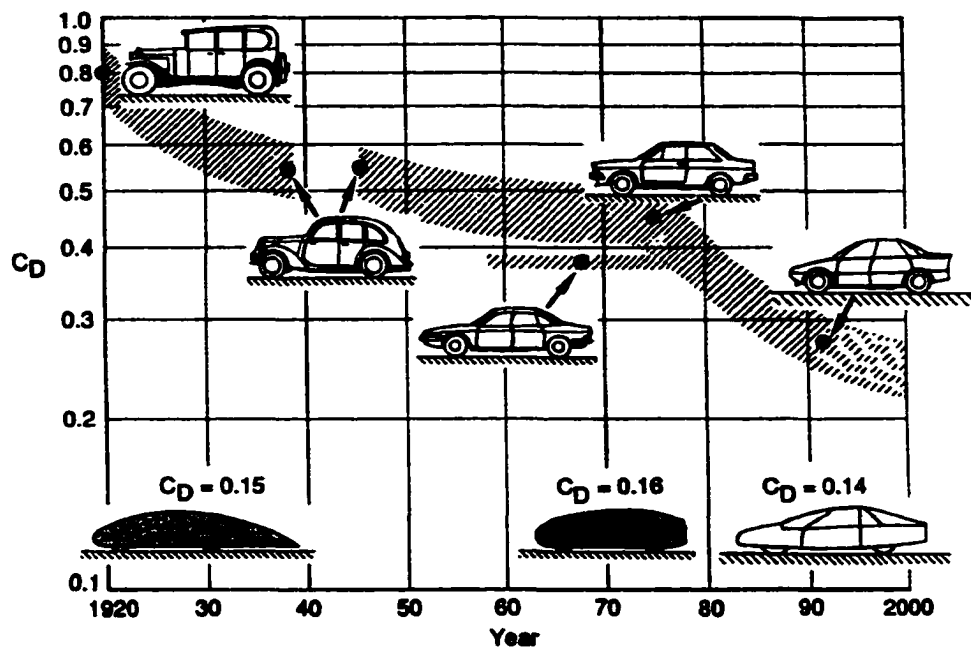
Figure 2.2. Drag coefficient improvement in history (with permission, from the Annual Review of Fluid Mechanics, Volume 25, ©1993, by Annual Reviews www.AnnualReviews.org).

In this section, the literature on ground vehicle aerodynamics is reviewed and underlying concepts highlighted. Although for today's ground vehicle aerodynamics have been extensively investigated under many sub-titles, for the benefit of this study, the literature review is classified as follows:

- Bluff Body Aerodynamics

- External Car Aerodynamics

- External Truck Aerodynamics

As the primary concern of this dissertation is external truck aerodynamics, the survey of literature in this particular area has been covered more extensively than the other areas mentioned above. Nevertheless, it is also intended to provide the reader with an informative review of the work conducted in the other areas, where the present study will broaden the possibilities.

2.1 BLUFF BODY AERODYNAMICS

In general, there are two common bluff body geometries that have been used as a benchmark case in the early automotive aerodynamics literature. The first generic bluff body case for ground vehicle aerodynamics was introduced by Morel (1978), and then Ahmed et al. (1984) modified this geometry and published similar bluff body study. Both geometries are almost the same size and shape, except the first one is slightly longer than the second. Later, more complex geometries, like Asmo II Body, were introduced. However, detailed geometry definition and easy manufacturability made Ahmed Body the first choice for most bluff body studies in ground vehicle aerodynamics.

Each bluff body research simplified and investigated a ground vehicle in different ways. The studies, which have been conducted by Morel (1978) and Ahmed et al. (1984) investigated rear end configuration on a bluff body model using time averaged measurement technique, and reported drag coefficient change and flow characteristics on the base. They both revealed the drag breakdown at ~30-deg backlight angle. Ahmed et al. (1984) also measured local drag from each surface and represented afterbody wake structure with ten hole directional probe measurements and oil visualization. Then, Han (1989) investigated Ahmed's model using steady Reynolds-averaged Navier-Stokes solver with k-ϵ model. Although his calculations predicted the location of separation and trailing vortices, calculations of pressure coefficient on the base did not match because of the lack of accuracy of the turbulence modeling. Later, the same model was experimentally studied by Sims-Williams and Domini (1998) with several techniques including twin hot-wire probes in the wake region. They investigated the flow unsteadiness at the critical backlight angle and pressure distribution on the longitudinal centerline of the model. Anagnost et al. (1997) presented drag, lift and pressure distribution for Morel Body, which is similar to Ahmed

Body, using a numerical method. They illustrated the simulation of fluid flow over the Morel body at different backlight angles, and predicted vortex flow phenomena. Original Ahmed body geometry later investigated by Baysal and Bayraktar (2001) solving the time-dependent, three-dimensional, Reynolds-averaged Navier Stokes (RANS) equations on flow-adapted unstructured meshes. The solutions were obtained after an extensive mesh refinement study and on a parallel computer. They presented pressure, lift and drag coefficients for several backlight angles using RNG k-ε turbulence modeling method. The unsteady wake flow, generated by virtue of the blunt base, was presented using computational flow visualization, and power spectral analysis was conducted on the recorded force data on the model. In addition, Bayraktar et al. (2001) also conducted an experimental study on an automobile-size Ahmed body model. In order to examine aerodynamics of a ground vehicle, wind averaged drag coefficient and Reynolds number dependencies were investigated.

Several other studies investigated similar bluff body structures for the variables other than backlight angle. Wake structure of a bluff body investigated by Duell and George (1992) in terms of ground clearance, aspect ratio of body and ground plane movement. Free stagnation point was measured with a hot wire anemometer and power spectral density analysis was conducted on several points in the wake using microphones. It was determined that modifying unsteady wake with insertion of a splitter plate cause a 75% reduction in the base pressure fluctuations, and a 6% cut in overall drag. Ground clearance and ground type (moving or stationary) for a bluff body, which represents an automobile, then investigated by Kim and Geropp (1998). Top and bottom pressure distributions were measured and Strouhal number was calculated for each ground clearance configuration. Measurements showed that the low ground clearance diminishes the periodic flow behind the model, and

the effect increases with a moving ground plane. Another bluff body study was conducted by Baysal and Bayraktar in 2001. Flowfield around different backlight angle configurations were computed and unsteady flow in the wake region was visualized. Similarly, Khalighi et al. (2001) have studied a small bluff body geometry in terms of ground vehicle aerodynamics, and reported the flow behavior in the wake region. Differently, model base configuration was altered using panels instead of backlight angle. Study reported up to 20% drug reduction with the drag reduction panels on the base. Another bluff body study in ground vehicle aerodynamics area was conducted for a wheel located within a wheelhouse cavity by Axon et al. in 1999. Three dimensional steady Navier-Stokes model was employed and both fixed and rotating wheel on moving ground were considered. Computational results compared with experimental measurements, and it was found that the rotating wheel produced more drag than the stationary wheel whilst wheelhouse cover drag decrease when the ground plane was moving compared to when it was stationary.

The latest improvements in computation power have introduced more sophisticated numerical methods into bluff body aerodynamics. It is still not possible to apply Large Eddy Simulation and Direct Numerical Simulation on the real industrial problems, but there are studies that are being conducted on simple geometries. For example, flow around a surface mounted cube was investigated with Large Eddy Simulation by Krajnovic and Davidson (2001a). Time averaged velocities and turbulent stresses were computed and compared with experiments. Drag and lift coefficients are presented along with other global quantities. Similarly, flowfield around a square cylinder at ground proximity was studied by Hwang et al. (2001). Unsteady, incompressible Navier-Stokes code with k-ω SST turbulence model was employed in the study and results from several ground proximity cases were reported. Finally, Large Eddy Simulation was applied to a simple bluff body in ground proximity by

Krajnovic and Davidson (2001b). Wake flow and base pressure coefficient were presented. Strouhal number was calculated for wake flow and compared with an experiment.

2.2 EXTERNAL CAR AERODYNAMICS

Ground vehicle aerodynamics has mostly been applied on automobiles. Especially in the early stages of the automotive industry, almost all the attention was focused on automobile aerodynamics. Though the present study focuses on heavy truck aerodynamics, computational examples from the last decade in external car aerodynamics are considered necessary to be mentioned.

One of the first published computational studies on certain automobile configuration was the Simulation of Corvette ZR-1 by Summa (1992). Potential flow and boundary layer schemes with simple, thin-shear-layer wake models were used in the calculations. Steady yaw effects and unsteady pitching motion were simulated, and centerline pressure distribution was reported. Faster design process in computational methods allowed parametric studies on specific automobile models. Aoki et al. (1993) tested several rear end configurations using the finite volume technique. Different configurations resulting different flow features in the wake region were simulated with computer visualization, and their effect on drag coefficient was discussed.

Later, increase in the number of computational studies made validation and accuracy investigation more important. Accuracy in drag prediction on automobiles was investigated by Ramnefors et al. in 1994. Both two dimensional and three-dimensional calculations were performed. Numerical scheme effect and mesh accuracy and its outcome on drag coefficient were investigated. Similarly, Okumura and Kuriyama (1995) compared the drag coefficients from different numerical schemes with experimental measurements and conducted a practical aerodynamic simulation on different yaw angle and door mirror

configuration. Investigation on other add-on devices continued with lateral tapering around the wheels by Horinouchi et al. (1995). In addition, front-end cooling grill configuration was investigated by Hytopoulos et al. (1998). Different configurations were studied with different inlet speeds, and numerical results and experimental measurements were compared. Later, Baysal and Meek (2002) investigated a NASCAR racecar model using a computational method. Both pressure and force coefficients for the model were reported with experimental results.

Both full body simulations and detailed investigations on add-on devices are still in the spotlight in automobile aerodynamics. As a continuation of this effort, several computational and experimental studies have been and are being conducted in the area.

2.3 EXTERNAL TRUCK AERODYNAMICS

Drag reduction studies of heavy trucks were started as a safety concern. Interaction between trucks and small vehicles in crosswinds was the primary matter. Then, special interest on external heavy truck aerodynamics gained more importance with the oil crisis in 1970s. Higher fuel prices forced industry to study on aerodynamic drag reduction methods.

With this impetus, experimental and analytical research projects were instigated. Two studies by Bauer and Servais (1974) and Mason (1975) can be given as the first examples of the drag reduction efforts for heavy trucks. Both studies conducted wind tunnel tests and reported drag coefficient difference for each model. The study by Bauer et al. was conducted with 5% scale wind tunnel models, and the results reported 30-65% drag reduction with 20-40% fuel efficiency depend on vehicle speed and weight. In addition, research by Mason developed an effective and practical add-on device (an air deflector) to reduce the aerodynamic drag on tractor-trailer configuration. The study was conducted on 1/16 and 1/7 scale models with different free stream velocity, and up to 30-35% drag

reduction was obtained. Another air deflector study was conducted by Kettinger (1982). Wind averaged drag coefficient was calculated for different deflector configurations and drag reduction was reported for different Reynolds numbers.

After body configuration also got into attention in aerodynamic development process. An aerodynamic full-scale boattail configuration was tested by Lanser et al. in 1991. Wind averaged drag coefficients and pressure distribution on centerline were presented for different boattail and yaw angle configurations. Results indicated that aerodynamic boattail reduced wind averaged drag coefficient about 9.8%. Similarly, a computational study was conducted on a boattail configuration by Hassan et al. (1995). The computation was performed on several boattail configurations, and the aerodynamic drag was reduced by 12.7%. Base flow investigation on tractor-trailer configuration with aerodynamic boattail device continued with the study by Gutierrez et al. (1996). Both computational and experimental methods were used in the study. Several boattail geometries were tested at 1/8 scale in a low speed wind tunnel, and pressure distribution, velocity contours and drag coefficients from both computational and experimental methods were compared. Another computational calculation was performed by Elankumaran (1997). Different boattail configurations with the length allowed by the Federal Regulations for US highways (see Appendix B) were investigated, up to 14% drag reduction obtained and computational visualization was performed in the wake region. Latest boattail study with simplified tractor-trailer geometry was published by McCallen et al. (2000). The study was conducted with numerical simulation with an experimental validation. Unsteady RANS and LES methods were employed for numerical calculations and the results presented with PIV (Particle Image Velocimetry) measurements.

Another interesting research was conducted on boundary layer control for drag reduction of a tractor-trailer model. The study conducted by Modi et al. (1992) investigated momentum injection and tripped boundary layer using judiciously located fences to interfere the flow and recover the pressure. Flow visualization study was conducted in a water channel, and drag measurements were indicated around 26% and 31% reduction on the configurations with momentum injection cylinders and fences. The same concept was also used later on automotive aerodynamics and a 35% reduction in drag coefficient was measured on an automobile model (Englar, 2000).

In recent years, computational simulations on truck aerodynamics started to be applied not only on partial or simplified geometries, but on also more complicated and full tractor-trailer combinations. Computational simulation for the external aerodynamics of heavy trucks was investigated in this manner by Baysal and Bayraktar (2000). The study was conducted on a 3D tractor-trailer combination, and external flow was presented using computer visualization. A parametric study was conducted on two commonly practiced engineering simplifications, which are tire and ground effects. Calculated total drag change was computed with and without tires (-6% drag error), and with and without ground plane motion (+9 drag error). Another parametric study was conducted by McLandress et al. (2001). The computational study aimed to design optimum aerodynamic shapes, such as grill bars, sun-visors, and profiles of hoods, windshields and roofs. A 2D design of a sun-visor was given as an example with an experimental validation. The study was also a sample of a rapid computational design and testing procedure, which evaluated 22 cases in 30 days.

CHAPTER 3

COMPUTATIONAL METHODOLOGY

Computers have been used to solve fluid flow problems for many years. Numerous programs have been written to solve either specific problems or specific classes of problems. From the mid-1970s, the complex mathematics required to generalize the algorithms began to be understood, and general-purpose CFD solvers were developed. The first commercial CFD software packages began to appear in the early 1980s and required what were then very powerful computers, as well as an in-depth knowledge of fluid dynamics and large amounts of time to set up simulations.

Consequently, CFD was a tool used almost exclusively in research. Recent advances in computing power, together with powerful graphics and interactive 3D manipulation of models, mean that the process of creating a CFD model and analyzing the results is much less labor-intensive, reducing the time and therefore the cost. Advanced solvers contain algorithms, which enable robust solution of the flow field in a reasonable time.

Because of these factors, Computational Fluid Dynamics is now an established industrial design tool, helping to reduce design timescales and improving processes throughout the engineering world. CFD provides a cost-effective and accurate alternative to scale model testing, with variations on the simulation being performed quickly, offering obvious advantages.

The set of equations that describe the processes of momentum, heat and mass transfer are known as the Navier-Stokes equations. These are partial differential equations,

which were derived in the early nineteenth century. They have no known general analytical solution but can be discretized and solved numerically.

There are a number of different solution methods that are used in CFD codes. The most common, and the one which has been used in the present dissertation, is the finite volume technique. In this technique, the region of interest is divided into small sub-regions, called control volumes. The equations are discretized and solved iteratively for each control volume. As a result, an approximation of the value of each variable at specific points throughout the domain can be obtained. In this way, one derives a full picture of the behavior of the flow.

3.1 MATHEMATICAL FORMULATION

The set of equations solved for the present study are the Navier-Stokes equations in their conservation form. The general form of the mass conservation equation, which is valid for incompressible as well as compressible one-phase flows, can be written as follows:

$$\frac{\partial \rho}{\partial t} + \frac{\partial}{\partial x_i}(\rho u_i) = 0 \tag{3.1}$$

Similarly, conservation of momentum in the i direction in an inertial (non-accelerating) reference frame is described by:

$$\frac{\partial}{\partial t}(\rho u_i) + \frac{\partial}{\partial x_j}(\rho u_i u_j) = -\frac{\partial p}{\partial x_i} + \frac{\partial \tau_{ij}}{\partial x_j} + \rho g_i + F_i \tag{3.2}$$

where p is the static pressure, τ_{ij} is the stress tensor (described below), and ρg_i and F_i are the gravitational body force and external body forces in the i direction, respectively.

The stress tensor τ_{ij} is given by,

$$\tau_{ij} = \left[\mu \left(\frac{\partial u_i}{\partial x_j} + \frac{\partial u_j}{\partial x_i} \right) \right] - \frac{2}{3} \mu \frac{\partial u_l}{\partial x_l} \delta_{ij} \tag{3.3}$$

where μ is the molecular viscosity and the second term on the right hand side is the effect of volume dilatation. In addition, conservation of energy is written by:

$$\frac{\partial}{\partial t}(\rho E) + \frac{\partial}{\partial x_i}\left(u_i\left(\rho E + p\right)\right) = \frac{\partial}{\partial x_i}\left(k_{\text{eff}}\frac{\partial T}{\partial x_i} + u_j\left(\tau_{ij}\right)_{\text{eff}}\right) + S_h \qquad (3.4)$$

$$E = h - \frac{p}{\rho} + \frac{u_i^2}{2} \qquad (3.5)$$

and for incompressible flow,

$$h = \frac{p}{\rho} \qquad (3.6)$$

where k_{eff} is the effective conductivity $(k + k_t)$ where k_t is the turbulent thermal conductivity, defined according to the turbulence model being used). The terms on the right-hand side of Equation 3.4 represent energy transfer due to conduction and viscous dissipation, respectively. S_h covers any other volumetric heat sources, that could exist. Equations (3.1)-(3.4) will be solved by a finite volume method. This approach involves discretization of the integral form of the governing equations, which are solved over a number of (finite) volumes within the fluid domain.

3.2 DISCRETIZATION METHOD

Analytical solutions to the Navier-Stokes equations exist for only the simplest flows under ideal conditions. Solutions for real fluid flow cases need a numerical approach, where the equations are replaced by algebraic approximations, which may be solved using a numerical method.

The finite volume method has been used in the present dissertation. This approach involves discretization of the integral form of the governing equations, which are solved over a number of (finite) volumes within the fluid domain. The Figure 3.1 shows a typical

mesh with unit depth, on which one surface of the finite volume is represented by the shaded area.
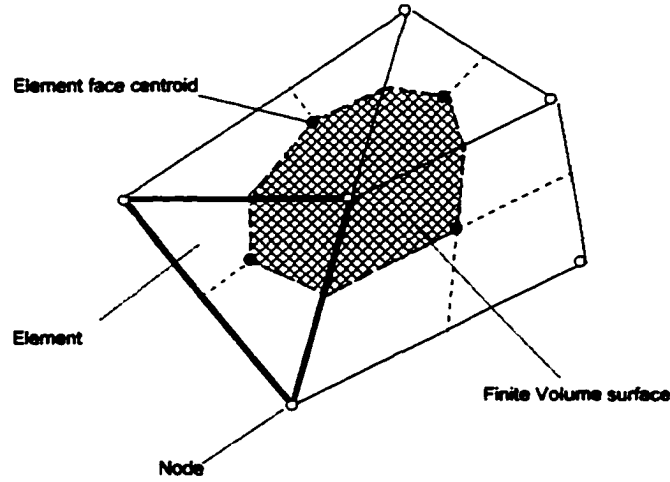
Figure 3.1 Typical mesh of finite volume discretization.

It is clear that each node is surrounded by a set of surfaces, which comprise the finite volume. All the solution variables and fluid properties are stored at the element nodes. Each node is surrounded by a set of surfaces, which comprise the finite volume. All the solution variables and fluid properties are stored at the element nodes. To demonstrate the method, consider the general scalar equation for the variable ϕ with no sources:

$$\frac{\partial(\rho\phi)}{\partial t} + \frac{\partial(\rho U_j \phi)}{\partial x_j} - \frac{\partial}{\partial x_j}\left(\mu_{eff} \frac{\partial\phi}{\partial x_j}\right) = 0 \tag{3.7}$$

This can be integrated over the control volume to give,

$$\frac{\partial}{\partial t}\int_V \rho\phi dV + \int_A \rho U_j \hat{n}_j \phi dA - \int_A \mu_{eff} \frac{\partial\phi}{\partial x_j}\hat{n}_j dA = 0 \tag{3.8}$$

where $\hat{n}_j$, is the surface outward normal vector and A and V are the outer surface area and volume, respectively. The first step in solving these continuous equations numerically is to approximate them using discrete functions.
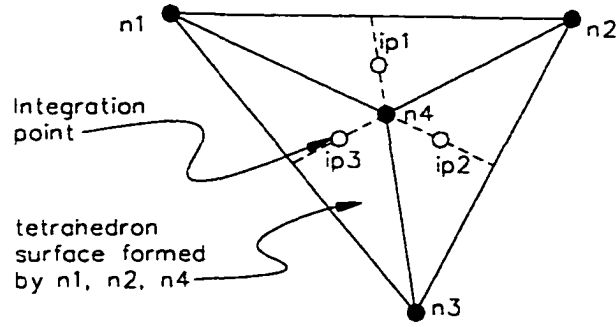
Figure 3.2. Mesh element on the surface

Now consider an isolated mesh element on the surface such as the one shown in Figure 3.2. The surface integrals are evaluated using integration points, ip_n, which are located at the center of each surface segment in a 3D element surrounding the finite volume. Using this notation, the advection (or transport) term can be approximated by,

$$\int_{ip} \rho U_j \hat{n}_j \phi dA = \sum_{ip} \dot{m}_{ip} \phi_{ip} \tag{3.9}$$

where $\dot{m}_{ip} = \rho U_j \hat{n}_j \Delta A$ is the discrete mass flow through a surface of the finite volume, ΔA is the surface area, ϕ_{ip} is the discrete value of ϕ at the integration point and the sum is over all surfaces of the finite volume. To complete the discretization of the advection term, the variable ϕ_{ip} must be related to the dependent variables stored at the nodes of the element, ϕ_n.

Many difference schemes developed for CFD are based on series expansion approximations (such as the Taylor series) for continuous functions. The upwind difference scheme (UDS) has been employed in this study. In the upwind difference scheme, the variable at ip is set equal to the upstream nodal variable at n as transported variables move with flow. The upwind difference scheme can be presented as

$$\phi_{ip} = \phi_n \tag{3.10}$$

The use of more expansion terms in the difference scheme brings more accuracy to the approximation. However, it should be noted that higher order schemes increase the computational load. The order of the scheme used is denoted by the order of the largest term in the truncated part of the series expansion. UDS as expressed in equation (3.10) is only first-order accurate, but it is usually very robust (numerically stable). However, this scheme, and others like it, can be susceptible to a phenomenon known as numerical diffusion or "gradient smearing" (see section 3.4.1 below).

Generally, the higher order schemes are more accurate because of the reduction in the truncation error. However, they may incur high computational penalties, because they require the evaluation of more terms than lower order schemes, and they can be less robust. They may display non-physical over and under-shoots in the solution generally attributed to a phenomenon called numerical dispersion (see section 3.4.2 below).

The basic discretization technique adopted in the present higher-order calculations is a conventional UDS with numerical advection correction (NAC) (AEA Tech., 1999) for the advection terms in the momentum and energy equations. NAC improves the accuracy of the UDS scheme by including a blending term in the discretization in the following way:

$$\phi_{ip} = \phi_n + \beta \phi_{NAC} \tag{3.11}$$

This gives a family of higher order accurate discretization. When $\beta = 1.0$, the full NAC discretization is implemented. With this value of β, the scheme is second-order accurate and is much better able to preserve large gradients and total pressure in the solution.

The pressure-velocity coupling in the mass and momentum equations is handled by the introduction of a fourth order "pressure redistribution" term in the discredized equations to overcome the problem of checkerboard oscillations which are found when the

variables are co-located. The method is similar to that used by Rhie and Chow (1982), with a number of extensions which improve the robustness of the discretization when the pressure varies rapidly or is affected by body forces.

The linear set of equations that arise by applying the Finite Volume Method to all elements in the domain are discrete conservation equations. The system of equations can be written in the form:

$$\sum_{nb_i} a_i^{nb} \phi_i = b_i \qquad (3.12)$$

where ϕ is the solution, b the right hand side, a the coefficients of the equation, i is the identifying number of the finite volume or node in question and nb means " neighbor," but also includes the central coefficient multiplying the solution at the ith location. The node may have any number of such neighbors, so that the method is equally applicable to both structured and unstructured meshes. The set of these, for all finite volumes, constitutes the whole linear equation system. For a scalar equation (e.g., enthalpy or turbulent kinetic energy), each a_i^{nb}, ϕ_{nb} and b_i is a single number. For the coupled, 3D mass-momentum equation set they are a (4 x 4) matrix or a (4 x 1) vector, which can be expressed as:

$$a_i^{nb} = \begin{bmatrix} a_{uu} & a_{uv} & a_{uw} & a_{up} \\ a_{vu} & a_{vv} & a_{vw} & a_{vp} \\ a_{wu} & a_{wv} & a_{ww} & a_{wp} \\ a_{pu} & a_{pv} & a_{pw} & a_{pp} \end{bmatrix}_i^{nb} \qquad (3.13)$$

and

$$\phi_i = \begin{bmatrix} u \\ v \\ w \\ p \end{bmatrix}_i \qquad (3.14)$$

$$b_i = \begin{bmatrix} b_u \\ b_v \\ b_w \\ b_p \end{bmatrix}_i \qquad\qquad (3.15)$$

It is at the equation level that the coupling in question is retained, and at no point are any of the rows of the matrix treated any differently (e.g. different solution algorithms for momentum versus mass). The advantages of such a coupled treatment over a non-coupled or segregated approach are several: robustness, efficiency, generality and simplicity. These advantages all combine to make the coupled solver an extremely powerful feature of any CFD code. The principal drawback is the high storage needed for all the coefficients.

3.3 COUPLED SOLUTION METHOD

Segregated solvers employ a solution strategy where the momentum equations are first solved, using a guessed pressure, and an equation for a pressure correction is obtained. Because of the 'guess-and-correct' nature of the linear system, a large number of iterations is typically required in addition to the need for judiciously selecting relaxation parameters for the variables.

A coupled solution approach (AEA Tech., 1999), which solves the hydrodynamic equations (for the state variables u, v, w, p) as a single system, has been used in the present study. This solution approach uses a fully implicit discretization of the equations at any given time step. For steady state problems, the time-step behaves like an "acceleration parameter" to guide the approximate solutions in a physically based manner to a steady-state solution. This reduces the number of iterations required for convergence to a steady state, or to calculate the solution for each time step in a time-dependent analysis.

3.3.1 General Solution

The overall solution process consists of two numerically intensive operations. For each time step:

1. The non-linear equations are linearized (coefficient iteration).

2. The linear equations are solved (equation solution iteration).

The time step iteration is controlled by the physical time step (global) or local time step factor (local) setting to advance the solution in time for a steady state simulation. In this case, there is only one linearization (coefficient) iteration per time step. For transient analyses, the time step and coefficient iterations can be changed.

3.3.2 Linear Equation Solution

Multigrid (MG) accelerated Incomplete Lower Upper (ILU) factorization technique has been used for solving the discrete system of linearized equations. It is an iterative solver whereby the exact solution of the equations is approached during the course of several iterations.

The linearized system of discrete equations described above can be written in the general matrix form

$$[A][\phi] = [b] \tag{3.16}$$

where $[A]$ is the coefficient matrix, $[\phi]$ the solution vector and $[b]$ the right hand side. The above equation can be solved iteratively by starting with an approximate solution, ϕ^n, that is to be improved by a correction, ϕ', to yield a better solution, ϕ^{n+1}, i.e.

$$\phi^{n+1} = \phi^n + \phi' \tag{3.17}$$

where ϕ' is a solution of

$$A\phi' = r^n \tag{3.18}$$

with r^n, the residual, obtained from,

$$r^n = b - A\phi^n \tag{3.19}$$

Repeated application of this algorithm yields a solution of the desired accuracy.

Iterative solvers, such as ILU, by themselves tend to rapidly decrease in performance as the number of computational mesh elements increases, or if there are large element aspect ratios present. The performance of the solver can be greatly improved by employing a technique called "multigridding."

3.3.3   Algebraic Multigrid Technique

The convergence behavior of many matrix inversion techniques can be greatly enhanced by the use of a technique called "multigridding." The process of multigridding involves carrying out early iterations on a fine mesh and later iterations on progressively coarser virtual ones. The results are then transferred back from the coarsest mesh to the original fine mesh.

From a numerical standpoint, the multigrid approach offers a significant advantage. For a given mesh size, iterative solvers are only efficient at reducing errors, which have a wavelength of the order of the mesh spacing. So, while shorter wavelength errors disappear quite quickly, errors with longer wavelengths, of the order of the domain size, can take an extremely long time to disappear. The multigrid method bypasses this problem by coarsening virtual mesh spacing during the course of the iterations, and then re-refining the mesh to still obtain an accurate solution. This technique significantly improves the convergence rates. The current solver uses a particular implementation of algebraic multigrid called additive correction. This approach is ideally suited to the solver implementation, because it takes advantage of the fact that the discrete equations are representative of the balance of conserved quantities over a finite volume. The coarse mesh equations can be created by merging of the original finite volumes to create larger ones as shown in Figure

3.3. (Figure 3.3 shows the merged coarse finite volume meshes to be regular, but in general, their shape becomes very irregular.) The coarse mesh equations thus impose conservation requirements over a larger volume and in so doing reduce the error components at longer wavelengths.
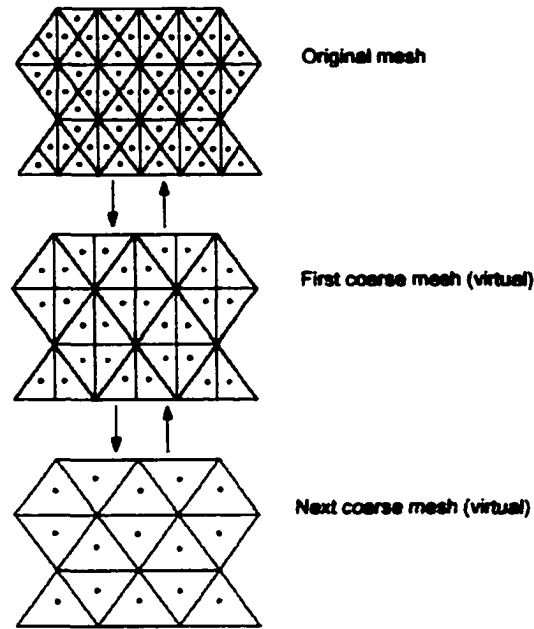
Figure 3.3 Multigrid algorithm.

3.4 DISCRETIZATION EFFECTS

All numerical approximation schemes are subject to a degree of error. Some errors are because of truncation of additional terms in series expansions. Others as a result of the order of the differencing scheme used for the approximation. Many of these effects can be significantly reduced or eliminated altogether by understanding why they occur and when they are likely to affect the accuracy of the solution.

3.4.1 Numerical Diffusion

Numerical diffusion is usually exhibited by difference equations whose advection term has been approximated using an odd-order scheme, for instance UDS, which is first

order accurate. Consider a three-dimensional Cartesian coordinate system. On a mesh of quadrilateral elements, the flow direction may be normal to the faces of each element. In this case, the flow from one element to the next can be accurately represented to the limit of the mesh size. In a case where the flow is not normal to the faces of the elements, perhaps in a region where the flow is recirculating, the flow must move from one element into more than one element downstream. Consequently, some flow moves into each of the adjacent elements as shown in Figure 3.4.

is more
accurate than
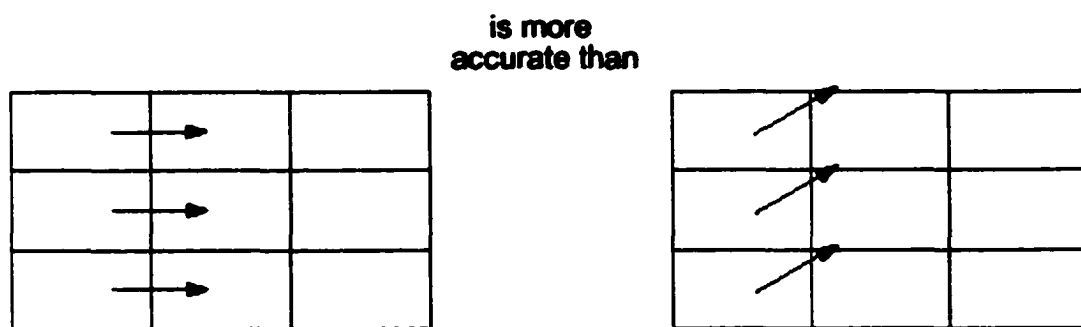
Figure 3.4 Flow direction and accuracy on a structured mesh.

The effect of this over a whole flow domain is that the features of the flow are smeared out. Figure 3.5 illustrates this effect. If a step function is used to define the inlet profile but not aligned with the mesh, the step is progressively smeared out as flow moves through the domain. This phenomenon is therefore sometimes called "gradient smearing."
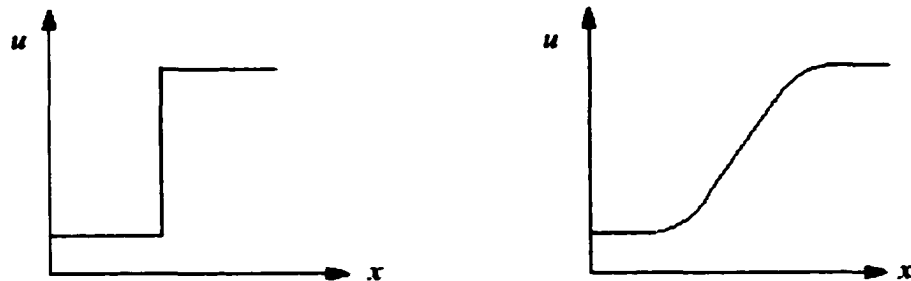
Figure 3.5 Gradient smearing effect.

The effect varies according to the alignment of the mesh with the flow direction. It is therefore relatively straightforward to achieve highly accurate solutions to simple flow problems, such as flow in a duct where alignment of the mesh with the predominant flow is relatively simple. However, for situations in which the flow is predominantly not aligned with the mesh, numerical diffusion effects limit the accuracy of the solution.

Consider a similar flow modeled on a totally unstructured tetrahedral mesh, as shown in Figure 3.6. With this type of mesh, there is no flow direction, which is more or less prone to numerical diffusion than any other. Consequently, the inaccuracy for simple unidirectional flows is greater than for a mesh of hexahedral elements aligned with the flow. However, the numerical diffusion errors for a mesh of tetrahedral are consistent, and of the same order, throughout the flow domain. This means that for real flows, tetrahedral control volumes will not exhibit additional inaccuracies in areas such as recirculation, because there is no single flow direction which may be aligned with the mesh.
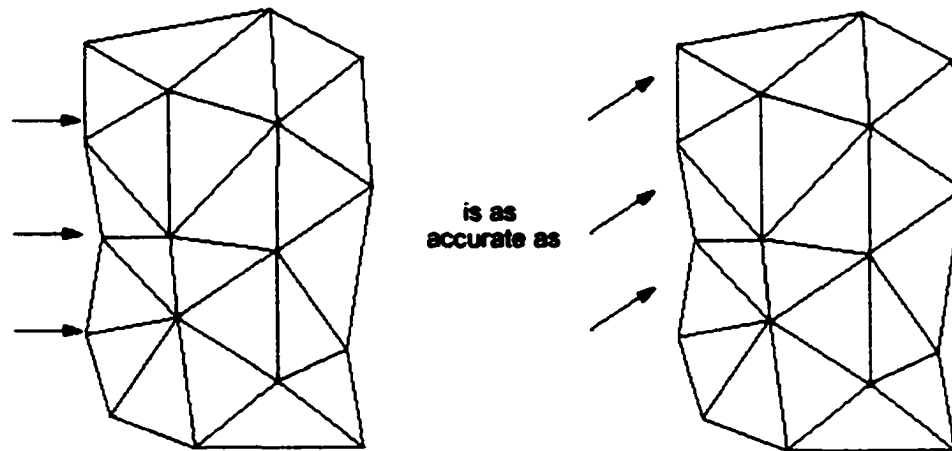
Figure 3.6 Flow direction and accuracy on unstructured mesh.

It is a fact that using the UDS scheme with tetrahedral element meshes will produce solutions that exhibit a larger degree of numerical diffusion than would exist from a solution

obtained with a similarly refined mesh of hexahedral elements. However, this difference diminishes rapidly as the advective discretization is made more second-order accurate, and by working towards a grid independent solution. In order to minimize the effects of numerical diffusion in the present study, computational calculations are started by using UDS and mesh refinement for initial results, and then switched to the second-order discretization. In addition, hybrid mesh (Figure 3.7), structured in the boundary layer region and unstructured in the rest of the domain, is used to minimize this problem.

Tetrahedral (unstructured) volume mesh

Inflated (structured) volume mesh
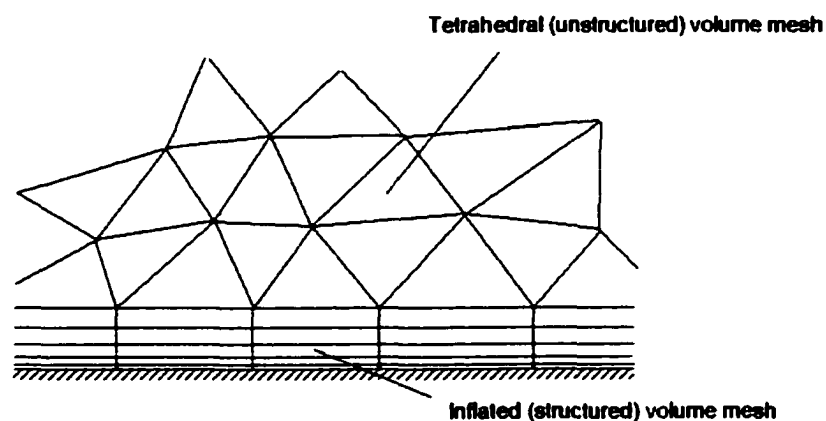
Figure 3.7 Hybrid mesh structure.

3.4.2 Numerical Dispersion

Numerical dispersion is usually exhibited by discretized equations whose advection term has been approximated using schemes that are even-order accurate. When numerical advection correction is fully implemented (with a value of $\beta=1.0$ in Equation 3.11) the scheme is second-order accurate. This can lead, in some cases, to numerical dispersion.

Dispersion results in oscillations or "wiggles" in the solution particularly where there are steep flow gradients (e.g., across a shock). Again the effects can be illustrated using the step function as shown in the Figure 3.8; just before and just after the step, the solution exhibits oscillations which are the direct result of numerical dispersion.
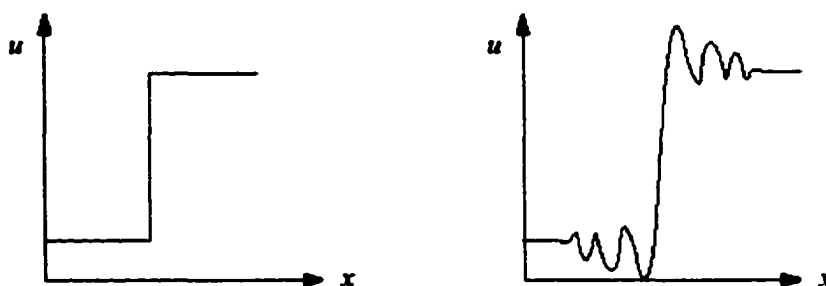
Figure 3.8 Numerical dispersion.

3.4.3 Rhie-Chow Discretization Errors

Rhie-Chow (1982) interpolation scheme has been used to locate the solution of the pressure and velocity fields at the same nodal locations in the mesh. The Rhie-Chow term, or equivalently, 4th-order smoothing of pressure, has for many years provided a reliable way to permit physically sensible solutions on co-located meshes (versus staggered meshes). For the vast majority of general flows, this treatment ties together the pressure fields to yield smooth solutions, while only minimally affecting the mass carrying velocities.

The adjustment to the mass carrying velocities appears as a 3rd-order zero term multiplying a higher derivative of pressure. For some analytical flow fields, on coarse meshes, the error introduced by the Rhie-Chow term can appear as non-negligible and, in fact, produce very spurious velocity fields.

The higher derivative of pressure mentioned above is not zero in these cases and does therefore dominate the mass carrying velocity (which should be zero). As the exact velocities are zero any disruption becomes very visible if scaled by the computed velocity field. However, comparing the resultant non-zero velocities to the velocity scale implied by the static head of the pressure field will show that they are small. And very importantly, they

will diminish by third order under mesh refinement (for a uniform mesh). For example, reducing the element size by a factor of 2 will reduce the error by a factor of 8.

In summary, whereas this effect can look very alarming under certain circumstances, it is in fact not a problem for most general flows (with a non-zero velocity scale), and can be made arbitrarily small for these benchmark flows by mesh refinement.

3.5 REYNOLDS AVERAGED APPROACH VERSUS LARGE EDDY SIMULATION

There are two methods being employed to transform the Navier-Stokes equations in such a way that the small-scale turbulent fluctuations do not have to be directly simulated: ``Reynolds averaging" and "filtering." Both methods introduce additional terms in the governing equations that need to be modeled in order to achieve "closure."

The Reynolds-averaged Navier-Stokes (RANS) equations represent transport equations for the mean flow quantities only, with all the scales of the turbulence being modeled. The approach of permitting a solution for the mean flow variables greatly reduces the computational effort. If the mean flow is steady, the governing equations will not contain time derivatives and a steady-state solution can be obtained economically. A computational advantage is seen even in transient situations, since the time step will be determined by the global unsteadiness in the mean flow rather than by the turbulence. The Reynolds-averaged approach is generally adopted for practical engineering calculations, and it uses turbulence models such as Spalart-Allmaras, k-ε and its variants and the RSM.

Large eddy simulation (LES) provides an alternative approach in which the large eddies are computed in a time-dependent simulation that uses a set of "filtered" equations. Filtering is essentially a manipulation of the exact Navier-Stokes equations to remove only the eddies that are smaller than the size of the filter, which is usually taken as the mesh size.

Like Reynolds averaging, the filtering process creates additional unknown terms that must be modeled in order to achieve closure. Statistics of the mean flow quantities, which are generally of most engineering interest, are gathered during the time-dependent simulation. The attraction of LES is that, by modeling less of the turbulence (and solving more), the error induced by the turbulence model will be reduced. One might also argue that it ought to be easier to find a "universal" model for the small scales, which tend to be more isotropic and less affected by the macroscopic flow features than the large eddies.

It should, however, be stressed that the application of LES to industrial fluid simulations is in its infancy. As highlighted in a review publication (Galperin and Orszag 1993), typical applications to date have been for simple geometries. This is mainly because of the large computer resources required to resolve the energy-containing turbulent eddies. Most successful LES has been done using high-order spatial discretization, with great care being taken to resolve all scales larger than the inertial subrange. The degradation of accuracy in the mean flow quantities with poorly resolved LES is not well documented. In addition, the use of wall functions with LES is an approximation that requires further validation.

Therefore, Reynolds-averaged approach is employed in this dissertation. The LES approach, briefly described in here, should become more feasible for industrial problems when the computational resources become significantly more powerful than what is available today. The rest of this section will deal with the computational procedure using the Reynolds-averaged approach, which is explained in Appendix C.

3.5.1 Eddy Viscosity Models

One proposal suggests that turbulence consists of small eddies which are continuously forming and dissipating, and in which the Reynolds stresses are assumed to be

proportional to mean velocity gradients. This defines an "eddy viscosity model." The effect of the Reynolds stress contribution is then described by the addition of a turbulence component of viscosity so that

$$\mu_{\textit{eff}} = \mu + \mu_t \qquad (3.20)$$

where $\mu_{\textit{eff}}$ is the "effective viscosity" and μ_t is the "turbulence viscosity" contribution from the Reynolds stress.

3.5.1.1   Zero Equation Models

Very simple eddy viscosity models compute a global value for μ_t from the mean velocity and a geometric length scale using an empirical formula. Because no additional transport equations are solved, these models are termed "zero equation." Simple to implement and use, zero-equation models can produce approximate results very quickly and provide a good initial guess for simulations using more advanced turbulence models.

The zero equation model is a simple eddy-viscosity concept which uses an algebraic equation to calculate the viscous contribution from turbulent eddies.

The turbulence viscosity is modeled as the product of a turbulent velocity scale, U_t, and a turbulence length scale, l_t, as proposed by Prandtl and Kolmogorov,

$$\mu_t = \rho f_\mu U_t l_t \qquad (3.21)$$

where f_μ ($=0.01$) is a proportionality constant. The velocity scale is taken to be the maximum velocity in the fluid domain. The length scale is derived using the formula:

$$l_t = \frac{V_D^{1/3}}{7} \qquad (3.22)$$

where V_D is the fluid domain volume.

3.5.1.2   Two Equation Models

Two-equation models are much more sophisticated than the zero equation models. Both the velocity and length scale are solved using separate transport equations (hence the term "two-equation"). An example of this type is the k-ε model, where k is the turbulence kinetic energy, and ε is the turbulence eddy dissipation. The k-ε model is a significant advancement over zero equation models because the turbulence viscosity can vary locally. It can also preserve flow history effects.

Two-equation turbulence models are very widely used, as they offer a good compromise between numerical effort and computational accuracy. The k-ε two-equation model has been built into most general-purpose computational fluid dynamic solvers. This model uses the gradient diffusion hypothesis to relate the Reynolds stresses to the mean velocity gradients and the turbulent viscosity. The turbulent viscosity is modeled as the product of a turbulent velocity and turbulent length scale.

In two-equation models, the turbulence velocity scale is computed from the turbulent kinetic energy, which is provided from the solution of its transport equation. The turbulent length scale is estimated from two properties of the turbulence field, usually the turbulent kinetic energy and its dissipation rate. The dissipation rate of the turbulent kinetic energy is provided from the solution of its transport equation. The k-ε model uses an eddy viscosity hypothesis for the turbulence and introduces two new variables into the system of equations.

The momentum equation becomes,

$$\frac{\partial \rho U}{\partial t} + \nabla \bullet (\rho U \otimes U) - \nabla \bullet (\mu_{\textit{eff}} \nabla U) = \nabla p' + \nabla \bullet (\mu_{\textit{eff}} \nabla U)^{T} + B \qquad (3.23)$$

where B is the sum of body forces, μ_{eff} is the effective viscosity accounting for turbulence and p' is the modified pressure given by,

$$p' = p + \frac{2}{3}\rho k \qquad (3.24)$$

The k-ϵ model, like the zero equation model, is based on the eddy viscosity concept, so that,

$$\mu_{eff} = \mu + \mu_t \qquad (3.25)$$

where μ_t is the turbulence viscosity. The k-ϵ model assumes that the turbulence viscosity is linked to the turbulence kinetic energy and dissipation via the relation,

$$\mu_t = C_\mu \rho \frac{k^2}{\epsilon} \qquad (3.26)$$

where C_μ is a constant. The values of k and ϵ come directly from the differential transport equations for the turbulence kinetic energy and turbulence dissipation rate,

$$\frac{\partial \rho k}{\partial t} + \nabla \bullet (\rho U k) - \nabla \bullet \left(\frac{\mu_{eff}}{\sigma_k} \nabla k \right) = P_k - \rho \epsilon \qquad (3.27)$$

$$\frac{\partial \rho \epsilon}{\partial t} + \nabla \bullet (\rho U \epsilon) - \nabla \bullet \left(\frac{\mu_{eff}}{\sigma_\epsilon} \nabla \epsilon \right) = \frac{\epsilon}{k}(C_{\epsilon 1} P_k - C_{\epsilon 2} \rho \epsilon) \qquad (3.28)$$

where $C_{\epsilon 1}$, $C_{\epsilon 2}$, σ_k and σ_ϵ are constants, which are given in Table 3.1. P_k is the shear production due to turbulence, which for incompressible flows is,

$$P_k = \mu_t \nabla U \bullet (\nabla U + \nabla U^T) - \frac{2}{3} \nabla \bullet U(\mu_t \nabla \bullet U + \rho k) \qquad (3.29)$$

Although the k-ϵ model is an industry standard, it can produce unreliable results particularly in regions of highly separated flow, due to the general assumptions of the eddy

viscosity model concept. Therefore, RNG k-ε model is selected at all computational calculations in the present dissertation.

3.5.1.3 RNG k − ε Model

The RNG k-ε model by Yakhot and Orszag (1986) is an alternative to the standard k-ε model. It is based on renormalization group analysis of the Navier-Stokes equations to develop a theory for the large scales in which the effects of the small scales are represented by modified transport coefficients. Further details of the RNG k-ε model can be found in Gatski et al. (1996).

The transport equations for turbulence generation and dissipation of the RNG k-ε model are the same as those for the standard k-ε model. The difference arises in the kinetic energy dissipation rate transport equations, where the constant $C_{\varepsilon 1}$ is replaced by a function. The function for $C_{\varepsilon 1}$ (see Equation 3.32) contains strain dependency to aid the model in dealing with flows that experience large separation and recirculation regions (Gatski et al., 1996). Since the flowfield in current study heavily involves in such flow conditions, the RNG k-ε model is chosen as the appropriate turbulence model.

In the RNG k-ε model, the transport equations for turbulence kinetic energy and turbulence dissipation rate become,

$$\frac{\partial \rho k}{\partial t} + \nabla \bullet (\rho U k) - \nabla \bullet \left(\frac{\mu_{\mathit{eff}}}{\sigma_k} \nabla k \right) = P_k - \rho \varepsilon \tag{3.30}$$

$$\frac{\partial \rho \varepsilon}{\partial t} + \nabla \bullet (\rho U \varepsilon) - \nabla \bullet \left(\frac{\mu_{\mathit{eff}}}{\sigma_\varepsilon} \nabla \varepsilon \right) = \frac{\varepsilon}{k} (C_{\varepsilon 1} P_k - C_{\varepsilon 2} \rho \varepsilon) \tag{3.31}$$

where

$$C_{\varepsilon 1} = 1.42 - f_\eta \tag{3.32}$$

and

$$f_n = \frac{\eta\left(1 - \dfrac{\eta}{4.38}\right)}{\left(1 + \beta\,\eta^3\right)}$$ (3.33)

$$\eta = \sqrt{\frac{P_k}{\rho C_\mu \varepsilon}}$$ (3.34)

where C_μ, $C_{\varepsilon 2}$, σ_k and σ_ε are constants (AEA Tech., 1999), which are listed in Table 3.1. Although the original derivation of coefficients and constants used in the RNG k-ε model were theoretical, the coefficients in the latest RNG model come from experimental results (as with the standard k-ε model).

Table 3.1 Coefficient list for k-ε and RNG k-ε models.

Model	$C_{\varepsilon 1}$	$C_{\varepsilon 2}$	C_μ	β	σ_k	σ_ε
k-ε	1.44	1.92	0.09	-	1.0	1.3
RNG k-ε	1.42-f_n	1.68	0.085	0.012	0.7179	0.7179

3.5.2 Wall Functions

Under certain turbulent flow conditions, such as fully developed flow and attached flow, the velocity profile near a wall assumes a characteristic shape. This boundary layer profile tends to contain a region where the velocity profile is logarithmic and universally expressible in terms of the wall shear stress. The assumed applicability of this profile provides a means to numerically compute the wall shear stress as a function of the velocity at a given distance from the wall. The mathematical basis is called a "wall function" and the logarithmic nature gives rise to the well known "law of the wall."
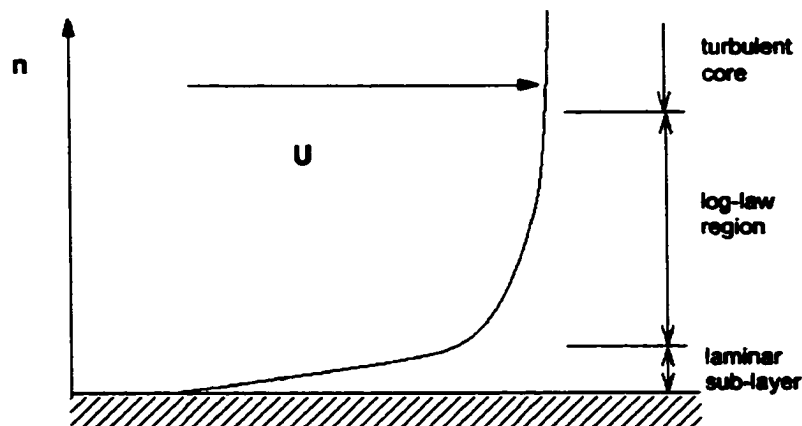
Figure 3.9 Turbulent boundary layers.

The obvious advantage of the wall function approach is that the high gradient shear layers near the wall can be modeled with a relatively coarse mesh yielding substantial savings in CPU time and storage.

Very close to the wall, the profile changes from logarithmic to linear, i.e., similar to that of laminar flow. This innermost region is sometimes called the "laminar sub-layer" (Figure 3.9). To complete the mathematical description of the boundary layer, therefore, the logarithmic function is merged with a linear one.

All turbulence models in the solver use wall functions. Under certain idealized conditions, such as fully developed, attached turbulent flow, the velocity profile assumes a characteristic shape. The boundary layer tends to contain a region where the velocity profile is logarithmic, and universally expressible in terms of the fluid shear stress, τ :

$$u = \left(\frac{\tau}{\rho}\right)^{\frac{1}{2}} \frac{1}{\kappa} \log\left(y^+ E\right) \tag{3.35}$$

where u is the near wall velocity, y^+ is the dimensionless distance from the wall, τ is the fluid shear stress, κ (=0.41) is the Von Karman constant and E (=9.793) is a log-layer constant (natural logarithms are used). If this profile reasonably approximates the velocity

distribution near the wall, it provides a means to numerically compute the fluid shear stress as a function of the velocity at a given distance from the wall. The alternative is to actually fully resolve the details of the boundary layer profile with the mesh, but this requires a prohibitively fine mesh and correspondingly large number of nodes. Thus, the advantage of the wall function approach is that the high gradient shear layers near walls can be modeled with relatively coarse meshes, yielding substantial savings in CPU time and storage.

In order to benefit from these advantages, the standard wall function is employed in the present dissertation. y^+ value is monitored for each computational calculation and kept less than 50 for the best accuracy at the wall boundaries.

3.6   BOUNDARY CONDITIONS

The equations relating to fluid flow can be closed (numerically) by the specification of conditions on the external boundary of the fluid domain. Hence, boundary conditions determine to a large extent the characteristics of the solution.

There are currently five boundary condition types in this study:

• Inlet

• Outlet

• Opening

• Wall

• Symmetry plane

Several options can be set for the various types of boundary conditions, which are related to different aspects of the boundary condition. Next, a brief description of each boundary condition is given.

3.6.1 Inlet

An inlet boundary condition is used where it is known that the flow is directed into the domain. The inlet boundary condition can be set in a number of ways, such as specifying mass flow rate, inlet velocity components or total velocity normal to boundary surface. It is depend on flow components that is known at the boundary and the particular physical model, which is being used for the simulation.

In the current study, Cartesian velocity components were given as inlet boundary condition. The component values are relative to the selected coordinate frame. The boundary velocity components were specified, with a non-zero resultant into the domain.

$$U_{Inlet} = U_{spec}i + V_{spec}j + W_{spec}k \qquad (3.36)$$

For the RNG k-ε turbulence model, the inlet turbulence quantities, k and ε, are calculated using expressions which scale the distribution at the inlet according to the turbulence intensity, I, where,

$$I = \frac{u}{U} \qquad (3.37)$$

Then, the inlet turbulence energy is calculated using,

$$k_{Inlet} = \frac{3}{2}I^2U^2 \qquad (3.38)$$

and the turbulence dissipation calculated using,

$$\varepsilon_{Inlet} = \rho C_{\mu RNG}\frac{k^2}{\mu_t} \qquad (3.39)$$

where

$$\mu_t = 1000/\mu \qquad (3.40)$$

Because the inlet flows of k and ε involve advection and diffusion,

$$Q^k_{Inlet} = Q^k_{advect} + Q^k_{diffus} \tag{3.41}$$

$$Q^\varepsilon_{Inlet} = Q^\varepsilon_{advect} + Q^\varepsilon_{diffus} \tag{3.42}$$

The advection flows are evaluated using the computed Inlet values of k and ε,

$$Q^k_{advect} = \dot{m}k_{Inlet} \tag{3.43}$$

$$Q^\varepsilon_{advect} = \dot{m}\varepsilon_{Inlet} \tag{3.44}$$

The diffusion flows are assumed negligible compared to advection and are equated to zero.

3.6.2 Outlet

An outlet boundary condition is used where it is known that flow is directed out of the domain. The hydrodynamic boundary condition specification for a subsonic outlet engages some constraint on the boundary static pressure. In the present study, relative static pressure is constrained such that the average is the standard atmospheric pressure,

$$P_{av} = \frac{1}{A}\int_S pdA \tag{3.45}$$

where the integral is over the entire outlet boundary surface. At the boundary, the relative static pressure is allowed to vary locally over the entire boundary surface, but the average value is constrained to the static atmospheric pressure.

In addition, for scalar quantities, a constant gradient constraint is imposed at the outlet boundary. The variables are extrapolated from the upstream location to the outlet boundary using the upstream gradient values.

3.6.3 Opening

An opening boundary condition allows the fluid to cross the boundary surface in either direction. In the current study, when the outlet of the boundary is relatively close to the wake region, the opening boundary condition is applied to minimize the boundary effect

in the wake region. With the opening boundary condition, all of the fluid might flow into the domain at the opening or out of the domain, or a mixture of the two might occur.

An opening boundary condition in this study is specified to atmospheric pressure value,

$$P_{Opening} = P_{spec}$$ (3.46)

The value is taken as relative total pressure for inflow and relative static pressure for outflow. Also, flow direction component for the opening boundary is set to normal to the boundary surface.

3.6.4   Wall

Walls are solid (impermeable) boundaries to fluid flow. Depending on the boundary location, there are three different wall boundary conditions used in the present dissertation:

No Slip (Stationary): The velocity of the fluid at the wall boundary is set to zero, so the boundary condition for the velocity becomes,

$$U_{Wall} = 0$$ (3.47)

On the model surface of all computational calculations, no-slip wall boundary condition is applied.

Free Slip: In this case, the velocity component parallel to the wall has a finite value (which is computed), but the velocity normal to the wall, and the wall shear stress, are both set to zero,

$$U_{n,Wall} = 0$$ (3.48)

$$\tau_w = 0$$ (3.49)

Free slip boundary condition is applied to the far field boundaries (except in and out boundary surfaces) in the computational domain of the present study.

No Slip (Moving): With this option, a velocity is specified on a boundary surface. With this specification, the fluid at the wall boundary moves at the same velocity as the wall. Therefore, the boundary condition is,

$$U_{Wall} = U_{spec}i + V_{spec}j + W_{spec}k \qquad (3.50)$$

In this case, the velocity specification defines a wall vector, which is perpendicular to the wall boundary normal. In the present study, moving wall boundary condition is used to simulate moving belt in a wind tunnel.

3.6.5   Symmetry Plane

Symmetry plane boundary condition is used when all the properties of physical flow are symmetric about some physical (flat) plane. In the present case, flow assumed to be symmetric at longitudinal symmetry plane, and symmetry plane boundary condition is applied to this surface.

The symmetry plane boundary condition imposes constraints, which "mirror" the flow on either side of it. At the symmetry boundary, the normal velocity component and the scalar variable gradients normal to the boundary are zero.

$$U_n = 0 \qquad (3.51)$$

$$\frac{\partial \phi}{\partial n} = 0 \qquad (3.52)$$

It should be noted that even a symmetrical geometry does not require that the flow is symmetrical in the domain. Therefore, in the present study, symmetry boundary condition is only used after testing its affect on the flow field.

With the definition of the boundary conditions used in this dissertation, computational methodology, governing equations for the computational method, their finite volume discretization, turbulence modeling and boundary conditions were discussed in the

current chapter. Now, this methodology needs to be validated for ground vehicle aerodynamics. Therefore, a benchmark case will be constructed in the next two chapters and the computational method and procedure will be investigated.

CHAPTER 4

EXPERIMENTAL MEASUREMENTS OF AHMED BODY AERODYNAMICS

Ahmed Body is the most common bluff body model in ground vehicle aerodynamics. Detailed geometry definition and easy manufacturability made it the final choice for the benchmark study in this dissertation. In this chapter, we describe the experimental measurements and demonstrate the results from Ahmed Body experiments.

Measurements for Ahmed body were performed at Langley Full-Scale Wind Tunnel (LFST). Old Dominion University (ODU), working under a Memorandum of Agreement with NASA Langley Research Center, operates the Langley Full-Scale Tunnel (Landman and Britcher, 1998, Landman, 2000). This facility is currently the second largest in the United States in terms of test section size and is the largest university-run wind tunnel in the world. The open jet test section is semi-elliptical in cross section with a width of 18.29 m (60 ft) and a height of 9.14 m (30 ft). The ground board is 13 m (42.5 ft) wide by 16 m (52.3 ft) long and features a turntable with a diameter of 8.7 m (28.5 ft) Vehicle drag and individual wheel down force can be measured using the current automobile balance. The overall aerodynamic layout of the facility, showing the double return design, is given in Figure 4.1. Power is supplied by two 3 MW (4000 HP) electric motors driving two 11 m (36 ft) diameter four-bladed fans. The current maximum speed is limited by a fan speed of 210 RPM, which is about 130 kph (~80 mph) in the test section. Vehicle drag and individual wheel down force are measured using the current automobile balance, which became fully operational in January of 1998 (Landman, 2000).
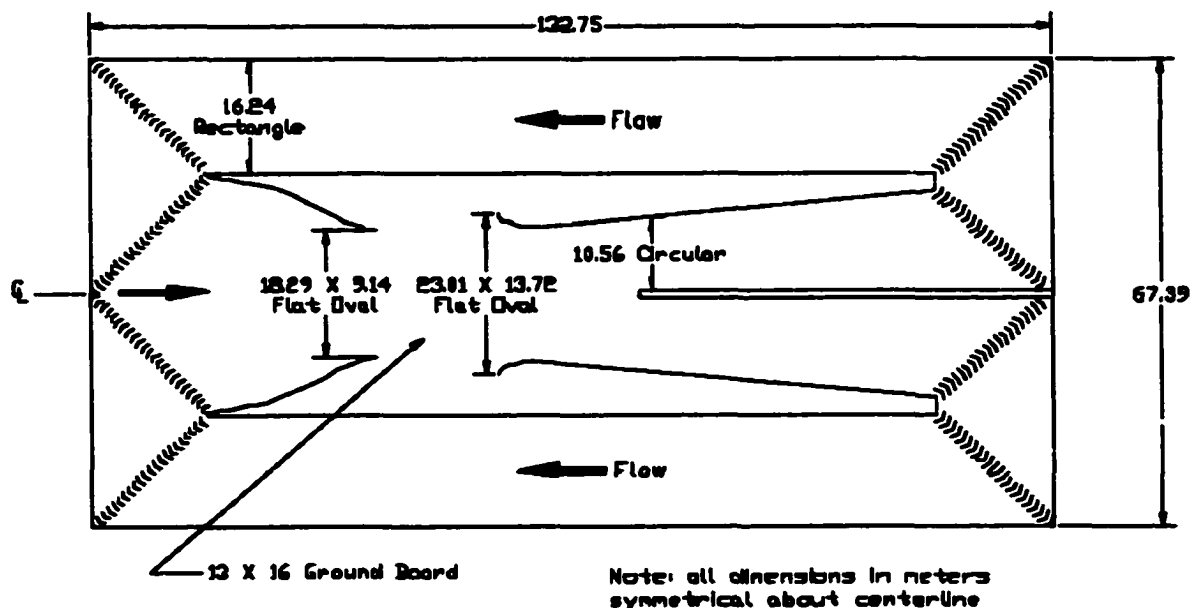
Figure 4.1 Layout of the Langley Full Scale Tunnel

4.1 MODEL SPECIFICATIONS

The experimental model, Ahmed body, consists of a steel space frame with a sheet metal skin welded on the outside surface (Figure 4.2). First, the steel frame was constructed to make the model structurally rigid. Then the skin surface was butted together from sheet metal panels and small gaps were taped with metal foil type.

Ahmed body was originally built to model a Sedan type passenger car. Backlight angle on the model characterizes the vertical angle between roof of the car and the trunk. In order to investigate different backlight angle effects on the aerodynamic behavior of the model, there were three different back panels (0-deg, 12.5-deg and 25-deg) constructed for the model. Each panel was built in same way, steel frame inside and metal sheet cover outside, and attached on the model.
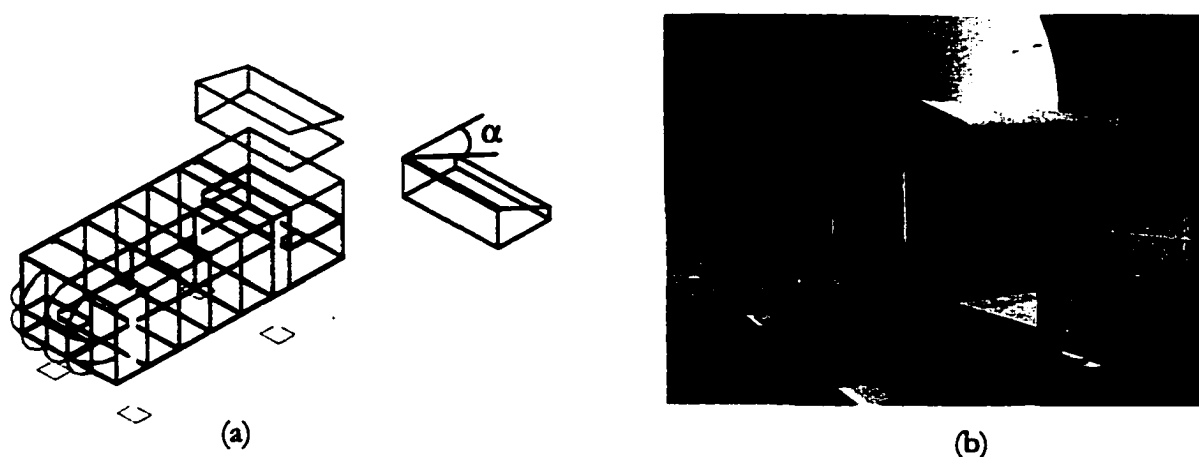
Figure 4.2 Ahmed body. (a) Experimental model steel frame and its back panel configurations and backlight angle α. (b) Model frame covered with sheet metal and mounted in the tunnel.

An Ahmed body (Ahmed et al. 1984) has been modeled experimentally at a true automotive scale in order to avoid well-known Reynolds number effects, such as varying separation points. Dimensions for the model were 4.91x1.83x1.35 m. The front surface was rounded with 0.51 m radii to minimize any separation on the front. The model was mounted on faired stands, as shown in Figure 4.2(b), at a height of 0.83 m above the ground board. In order to diminish the aerodynamic force on the model legs, each model leg was also covered with airfoil-shaped envelope. The current model is 4.7 times larger than the model that was used in the original study by Ahmed et al. (1984). The frontal area to test section area ratio is about 1.4%, representing a very small blockage (Hucho, 1998). The free jet and relatively nonexistent blockage make for a very low level of experimental uncertainty.

4.2 MEASUREMENT METHODS

Surface pressures and force coefficients (drag and lift coefficients) at full-scale Reynolds numbers were measured for all three different backlight angles: 0-deg, 12.5-deg, and 25-deg.

Pressures were measured on the centerline of the four sides and over the entire surface of the nose and the base regions. A total of 56 pressure probes were installed on the model surface. Pressure taps distributed on the longitudinal symmetry plane (16 on top, 12 on bottom), each side of the model (8 on right side, 8 on left side) and the back surfaces (12 on back). Figure 4.3 shows pressure tap connections in the model.
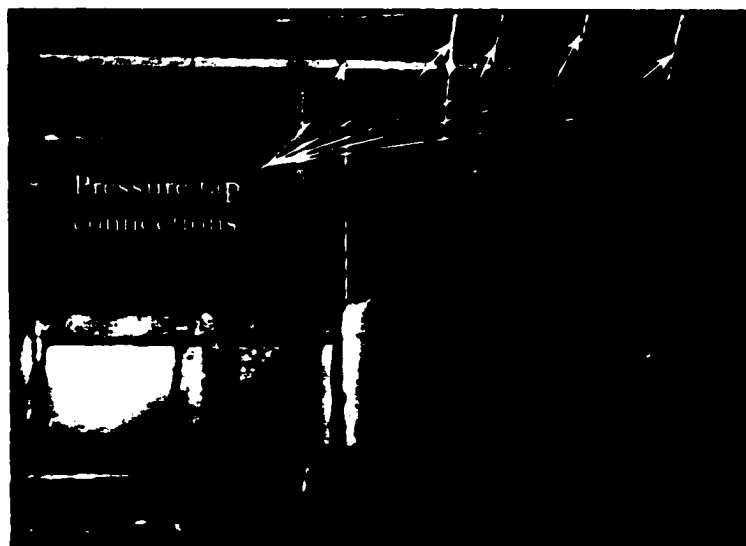
Figure 4.3 Pressure tap connections inside the model.

Pressures were measured with a Pressure Systems Inc. model 8400, 10-inch water column, electronic-scanning module. The estimated uncertainty in the pressure coefficient is ± 0.005 (Landman, 2000).

The ground board is freestanding, such that a new boundary layer begins at the leading edge with flow both over and under the planar surface. A boundary layer control suction slot was used for all runs to reduce the displacement thickness at the center of the model to about 0.5 inches. The ground board is shown to scale in Figure 4.4 with the outline of the model.

LEADING EDGE

TRAILING EDGE

AHMED BODY

FLOW DIRECTION ——▶

TOP VIEW

TURNTABLE

SUCTION SLOT LOCATION
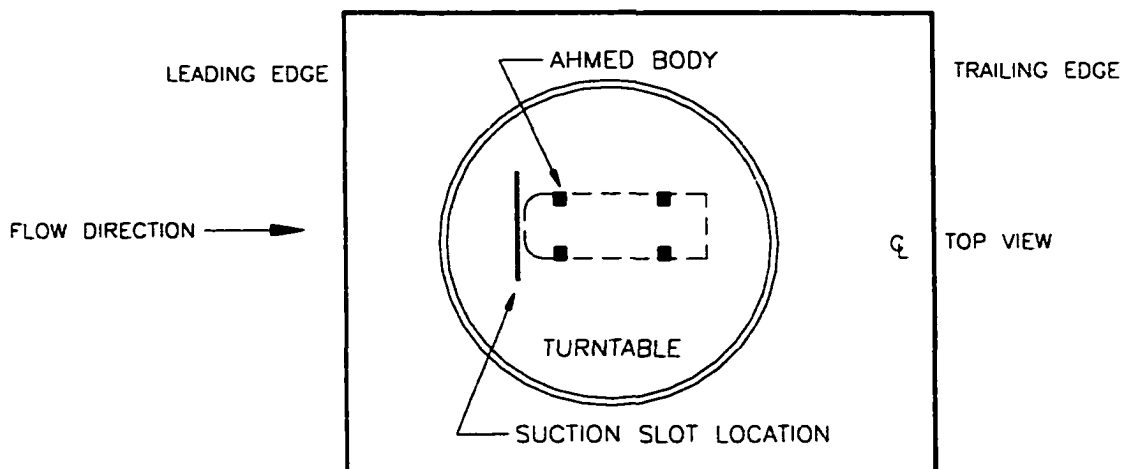
Figure 4.4 The ground board in the test section of Langley Full Scale Tunnel.

Force components on the experimental model were measured using LFST Trapeze Force Balance System. Force balance system was called the "Trapeze Balance," due to the swinging frame, which is used to measure drag. The overall concept is shown in Figure 4.5. In order to measure drag, a rigid frame is suspended on flexible elements (flexures) under the ground board turntable and is free to translate in the streamwise direction. The rigidity of the flexures in the axial direction is several orders-of-magnitude lower than a typical beam style strain gage loadcell. The frame, therefore, transfers the drag force on the model to a loadcell contacting the aft cross bar.
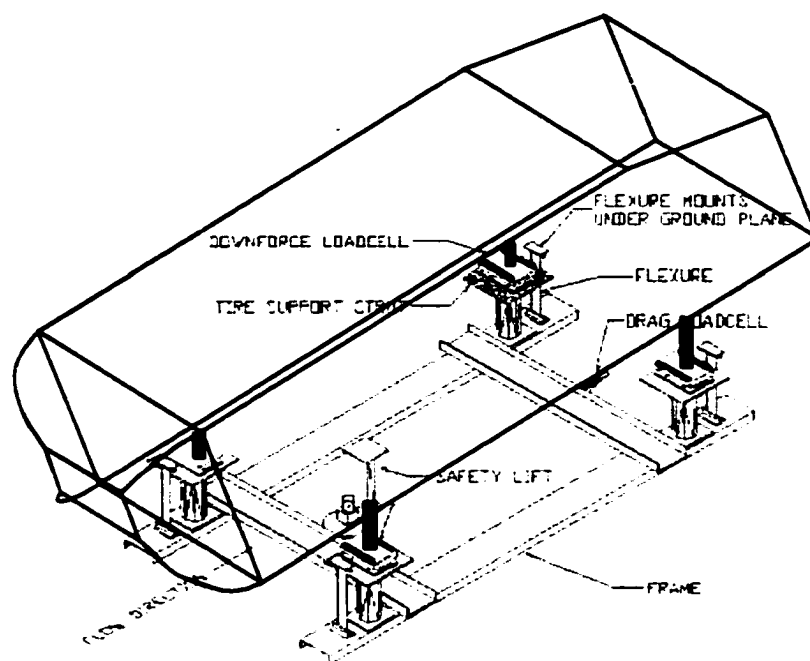
Figure 4.5 LFST Trapeze Force Balance System and the model.

This arrangement allows quick replacement of drag loadcells with load ranges chosen for maximum sensitivity up to 2.22 kN (500 lbs.). Tire support struts are rigidly mounted to the frame and support multi-element beam loadcell modules, which measure the downforce at each leg. The acceptable weight plus aerodynamic downforce is limited primarily by the flexure cross sectional area and the loadcell capacity. In this study, force coefficients were measured using the aforementioned automotive balance system and has an estimated absolute uncertainty of ± 0.003 (Landman, 2000).

Backlight angle, yaw angle and Reynolds number are counted as primary variables for the current experimental study. Backlight angle α is known as the critical design parameter for the wake flow. Therefore, three different α values (0-deg, 12.5-deg, 25-deg) and six different Reynolds numbers (2.2 M to 13.2M) were chosen for the experiments (Table 4.1).

This wide range of Reynolds number measurements also allowed us to be able to compare with both previous low Reynolds number studies (Ahmed et al. 1984, Morel 1978) and full scale car or light truck cases (Landman, 2000, Landman and Britcher, 1998).

Table 4.1 Experimental measurements for test cases with varying backlight angle, yaw angle and Reynolds number (Re number in millions: i=2.2M, ii=4.4M, iii=8.8M, iv=13.2M).

Backlight angle / Yaw angle	0-deg	±3-deg	±6-deg	±9-deg	±12-deg	±15-deg
0.0-deg	i,ii,iii,iv	i,ii,iii,iv	iii	iii	iii	iii
12.5-deg	ii,iii,iv	ii,iii,iv	iii	iii	iii	iii
25.0-deg	ii,iii,iv	ii,iii,iv	ii,iii	ii,iii	ii,iii	ii,iii

In order to calculate the wind-averaged drag coefficients, measurements have been repeated at several yaw angles (0-deg, ±3-deg, ±6-deg, ±9-deg, ±12-deg, ±15-deg). Given below is the formula to obtain the wind-averaged drag, where the arguments of the terms on the right hand side indicate the yaw angle for that particular drag value.

$$C_{D,ave} = 0.219C_D(0) + 0.185(C_D(+3) + C_D(-3))$$
$$+ 0.110(C_D(+6) + C_D(-6)) + 0.078(C_D(+12)$$
$$+ C_D(-12)) + 0.022(C_D(+15) + C_D(-15))$$

(4.1)

4.3 EXPERIMENTAL RESULTS

Experimental results were obtained from both surface pressure and force measurements. Pressure and force data collection managed by Labview© Data Acquisition Software. Figure 4.6 shows graphical user interface (GUI) for pressure and force data measurements. Data measurements were conducted using two personal computers simultaneously. Sampling time was 2.5 minutes with average standard deviation of 0.3% for pressure measurements.
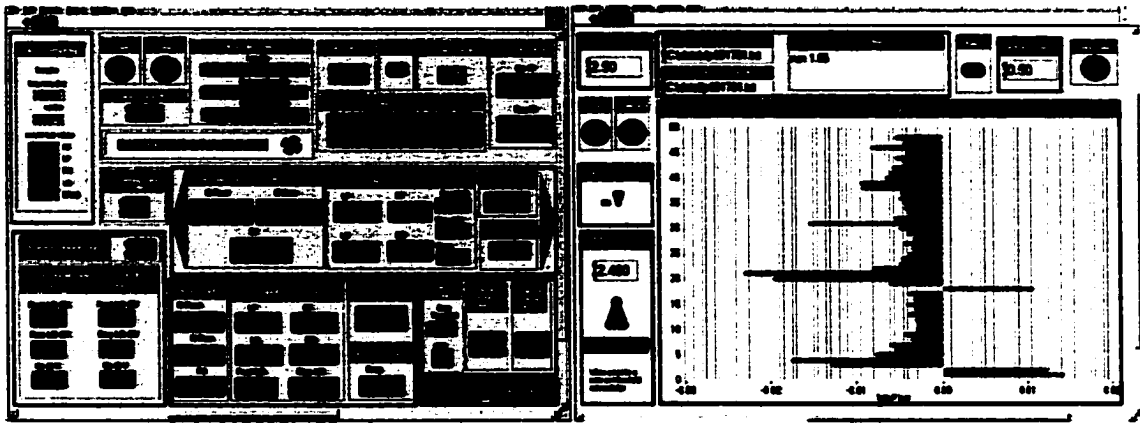
Figure 4.6 Graphical user interface (GUI) for pressure and force measurements.

Reynolds number is the one of the most important variables in vehicle aerodynamics. Figure 4.7 shows the Reynolds number effect on pressure coefficient on the top surface centerline at zero yaw angle. As clearly seen from the figure, the pressure coefficient values follow the same path at all cases. The figure shows that there is not much change (max. 0.06) in the pressure coefficient with Reynolds number. In the front region, pressure coefficient drops up to -1.45 and then recovers immediately. Then, on the top surface, the average C_p value stays around -0.1.
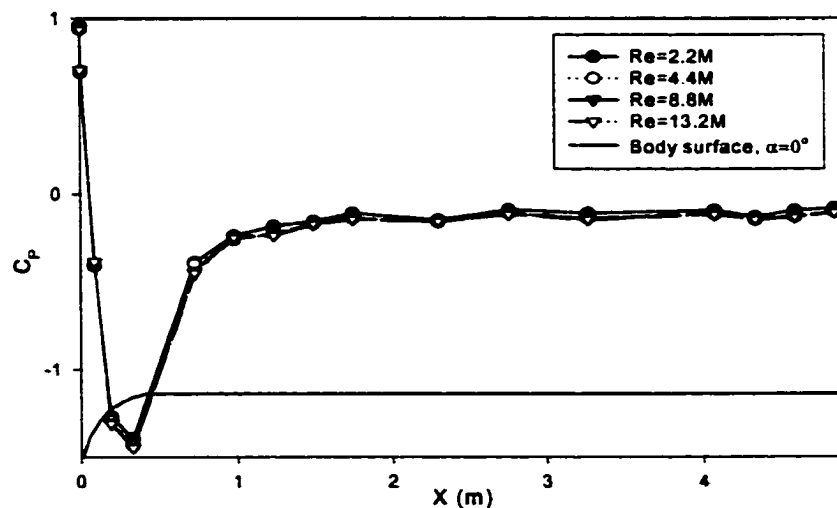
Figure 4.7 Reynolds number effect on pressure coefficient (zero yaw angle).

Since the experimental model is symmetric and the free stream flow is parallel to the model, pressure coefficient variation is supposed to be same on the right and left sides of the model. In order to prove this assumption and validate the model symmetry, pressure coefficients along the centerline of left and right side walls were measured and plotted in Figure 4.8. Figure shows a clear match in between right and left pressure coefficient distribution. Especially, increasing Re number makes the agreement even closer.
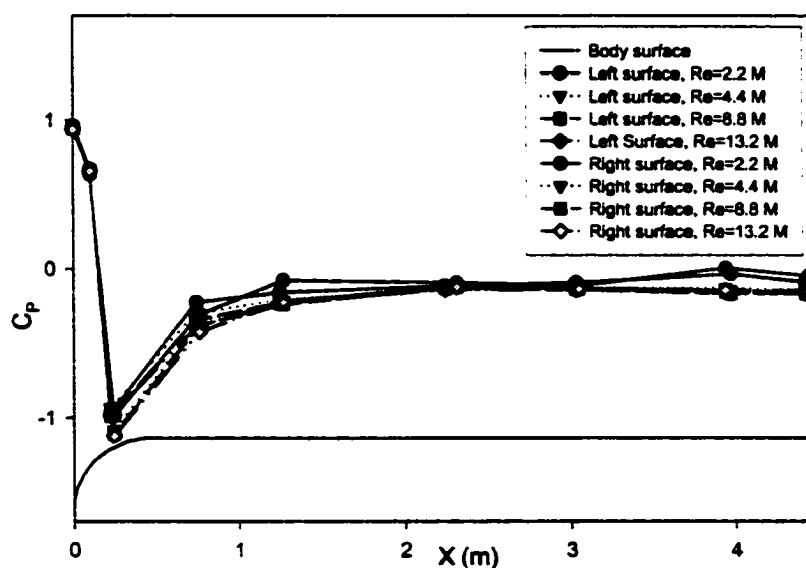
Figure 4.8 Pressure coefficient variation on the side surfaces (zero yaw angle).

Shown in Figure 4.9 is the dependency of the drag and lift coefficients on the Reynolds number. In general, drag coefficient decreases and lift coefficient stays relatively constant with Reynolds number. As Reynolds number ranges from 2.2M to 13.2M, C_D differs up to ± 0.0052. The C_L variation in this range stays within ± 0.0024 except for the 0-deg back-angle case. Although the biggest change on C_L occurs at 0-deg back-angle case with ± 0.017, the overall change on C_L versus Reynolds number is barely evident.
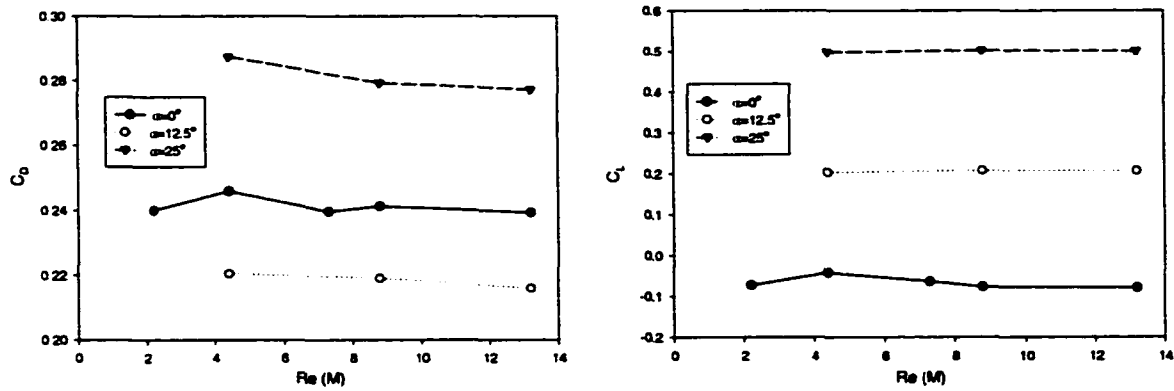
Figure 4.9 Effect of varying the flow Reynolds number on drag and lift coefficients (zero yaw angle).

Backlight angle is another important parameter in the present study. Figure 4.10 shows the time averaged pressure coefficient distribution along the top surface centerline for different backlight angle configurations. Although the values for different back angles collapse on each other during the expansion followed by the recompression near the front, the rates of the second expansion and their recovery vastly differs.
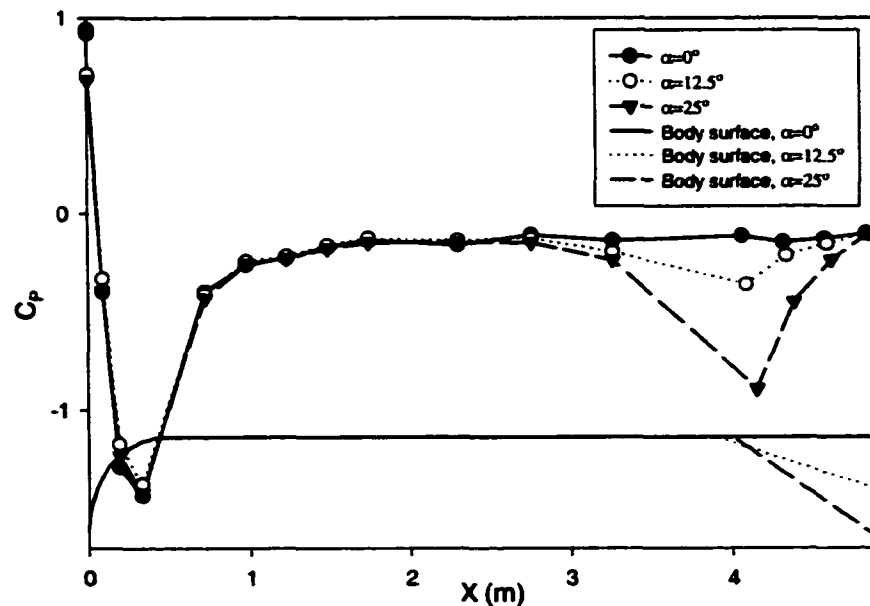
Figure 4.10 Experimental pressure coefficient distributions on the top surface at body symmetry plane for various backlight angles.

Figure 4.11 shows the variation of the drag coefficient versus the yaw angle. The wind averaged drag coefficients provide a true measure of vehicle performance under road conditions found in nature (Hucho, 1998). When comparing the drag values of the three backlight angle configurations in Figure 4.11, they appear to be consistent in that the difference in C_D between cases at zero-yaw is closely matched by the difference in wind-averaged drag results. One interesting feature is the asymmetry found in the 12.5° backlight angle case. The difference between right and left yaw measurements may indicate flow hysteresis. Flow that is separated from the body at −15° may not become attached over the same area as the body is yawed through +15° under continuous flow conditions in the wind tunnel. This effect is of course common in airfoil testing as an airfoil's angle-of-attack is increased beyond stall and then decreased back to a value where flow was previously attached(Abbott and VonDoenhoff, 1959). The influence of the trailing vortex system may also play a role in the flow physics.
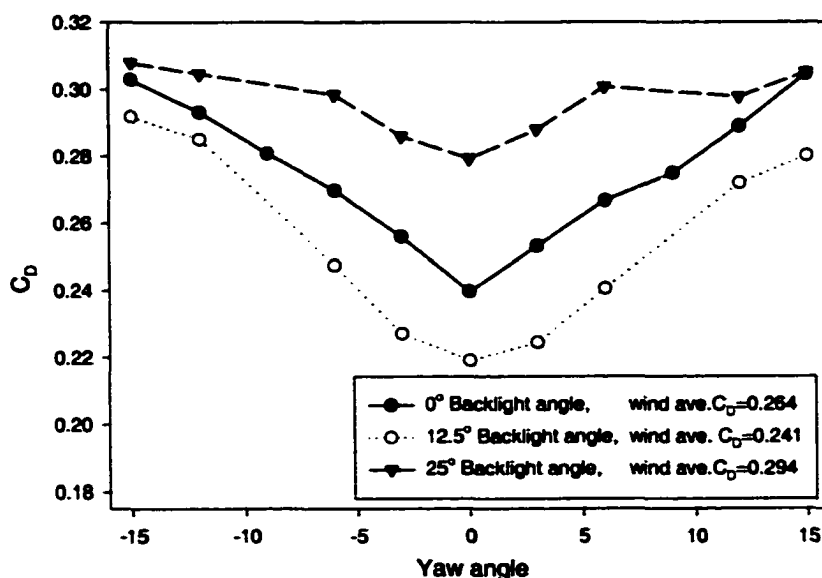
Figure 4.11 Wind-averaged drag coefficients for bodies with three different backlight angles (Re=8.8M) (with permission, from SAE 2001-01-2742).

Figure 4.12 shows time-averaged drag and lift coefficients that were measured with LFST Trapeze Force Balance System. As expected, the lift increases with the increasing backlight angle almost linearly. Minimum drag occurs at 12.5-deg backlight angle case. However, the drag is fairly insensitive to backlight angle changes.
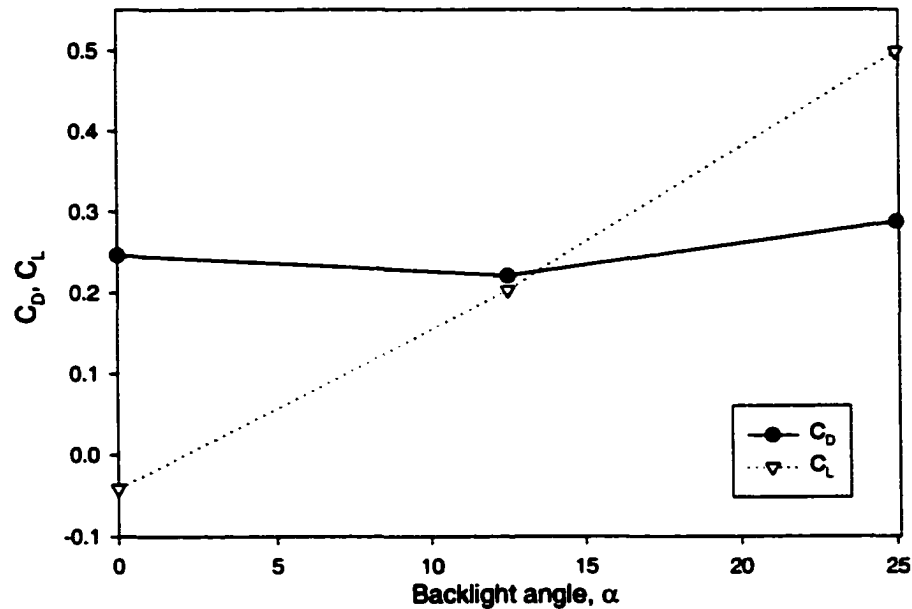
Figure 4.12 Drag and lift coefficients versus backlight angle (Re=8.8M).

Force coefficient measurements and flow visualization with tuft presented aerodynamic characteristics Ahmed Body in terms of ground vehicle. After current experimental measurements, a benchmark case was prepared for the numerical calculation. Computational results and comparison with experimental outcome for Ahmed Body are discussed in the following chapter.

CHAPTER 5

COMPUTATIONS OF AHMED BODY AERODYNAMICS

In the course of this chapter, we explore the case of bluff body aerodynamics using the Computational Fluid Dynamics (CFD) technique described in Chapter 3. Experimental measurements, which were used to build a benchmark case for numerical calculations, were highlighted before in the previous chapter. In this chapter, the Ahmed body geometry is submitted to the computational solution procedure and results are compared.

The computer simulation of such a flow field requires solving its governing equations. First, the computer-aided-design (CAD) model of the vehicle-like-body was developed. Then, a hybrid unstructured mesh, consisting of prismatic and tetrahedral cells, was generated for the computational domain. The details of the computer code are given in Chapter 3, and its implementation for ground vehicle aerodynamics is given in recent publications (Baysal and Bayraktar 2000, Baysal and Bayraktar, 2001).

The present investigation looks at the problem and studies the Ahmed body as a comparison and validation case. Therefore, the external aerodynamics of the Ahmed body that is representative of a car or light truck is investigated in detail. The numerical calculations used a Reynolds-averaged, unsteady Navier-Stokes formulation. Computational results are presented for backlight angles of 0-, 5-, 15-, 20-, 25- and 30-degrees, then compared with the experimental results and the data available in the literature.

Since the flowfield being considered herein is in ground proximity and can be unsteady, it requires time-accurate solutions of the viscous-flow equations. Therefore, the set of equations solved for the present study are the time-dependent, Reynolds-averaged,

Navier-Stokes equations in their conservative form. Reynolds-averaged quantities are obtained through a time-averaging process. To achieve these simulations within the currently available computer resources and the project milestones, the effects of turbulence needed to be "modeled." It was realized, however, that none of the existing turbulence models was developed for unsteady flows. Therefore, the present time-accurate, finite-volume CFD methodology with its RNG k-ε turbulence model was previously benchmarked using a series of well-documented flows (Han, 1989, Baysal and Bayraktar, 2001). Iterative solvers, such as the incomplete lower upper (ILU) factorization technique used herein, by themselves tend to rapidly decrease in performance as the number of computational mesh elements increases, or if there are large element aspect ratios present. Therefore, the performance of the solver was greatly improved by employing a multigrid technique (see section 3.3.3 above).

There are several parameters affect on CFD calculations. Proposed method and procedure are vulnerable to most of them indeed. Before proceeding further, these parameters on the numerical solution need to be investigated. Easy-producible bluff body shape and availability of the experimental results made the Ahmed Body one of the best choices for this investigation. Following, we enumerate the variable conditions and investigate their effect on the numerical results.

5.1 COMPUTATIONAL DOMAIN SIZE

Domain size influence on the results is not desired in any CFD calculation. Therefore, computational domain needs to be defined carefully. Domain size not only has an effect on numerical results, it also changes the mesh size. Size of the domain in current calculations is primarily selected with experience, and then refined with cut-and-try

approach. Selecting far field boundary is also taken into the consideration, because subsonic boundary conditions and their location could influence the solution in entire domain.

Figure 5.1 illustrates the three different computational domains for the Ahmed body case. Because primary calculations present no unsteady effect in the front and side regions, attention is given to the wake flow. Although all domains predicted pressure distribution on the model very well, unsteady calculations were conducted at model 5.1(b).
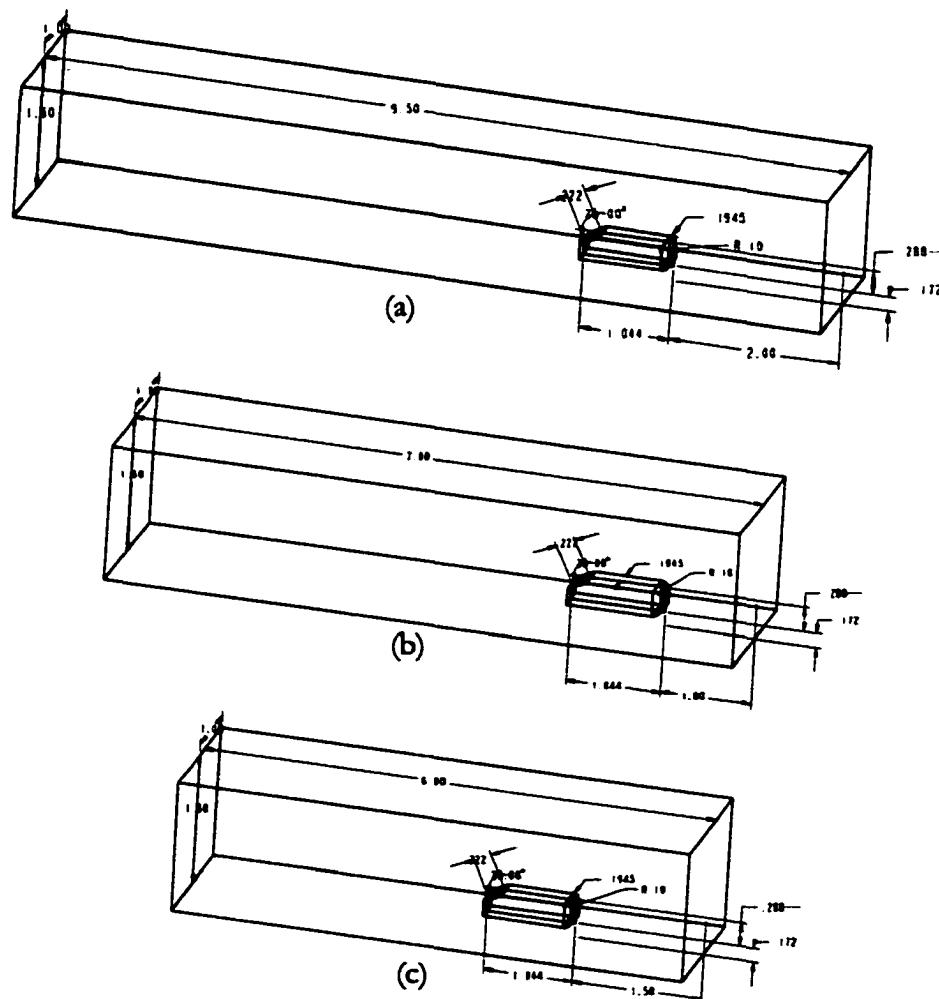
Figure 5.1 Computational domains and their dimensions (all units in meters).

5.2 MESH SENSITIVITY ANALYSIS

To study the attainment of mesh independence, several cases were run with sequentially refined meshes. Presented in Figure 5.2 are the drag coefficients computed on these meshes, the value measured in the wind tunnel and the discrepancy between the computed and measured values (ΔC_D). Based on this study, the mesh employed for the cases presented herein had 150x70x60 cells on the body and the total mesh contained about 5.4 million cells. In order to improve the computational accuracy, the final mesh was also adapted to the flow with hierarchical adaptation process (Grosso and Greiner, 1998). Adaptation variables were selected as pressure and total velocity. Figure 5.3 shows the initial and the final mesh distribution after 3-step adaptation for zero- deg backlight angle case.

For the computational study, six cases based on different values of the backlight angle α (0-deg, 5-deg, 15-deg, 20-deg, 25-deg and 30-deg) have been considered.
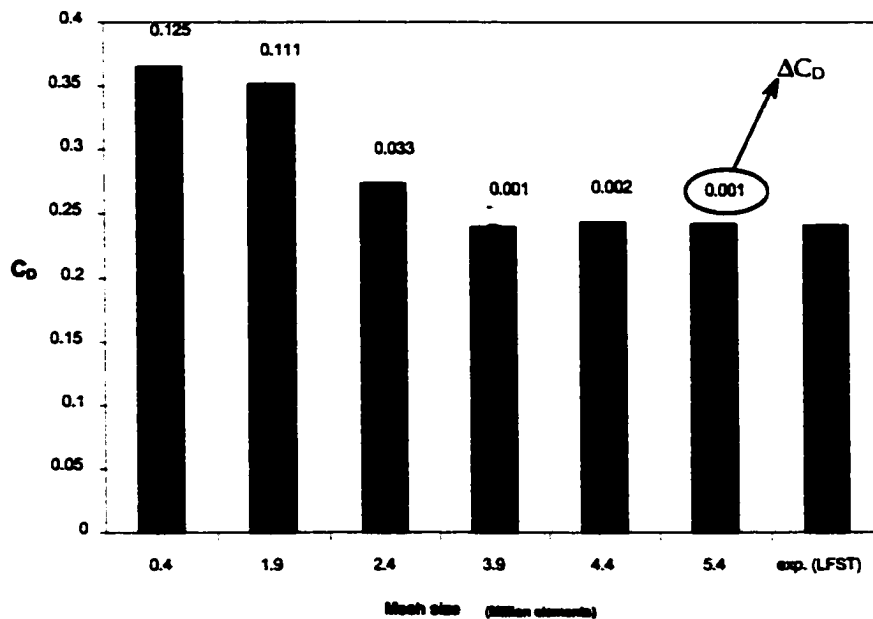
Figure 5.2 Improvement in drag computations by increasing mesh density and their comparison with wind-tunnel measurements (0-deg. backlight angle, Re=4.4 M). (with permission, from SAE 2001-01-2742).
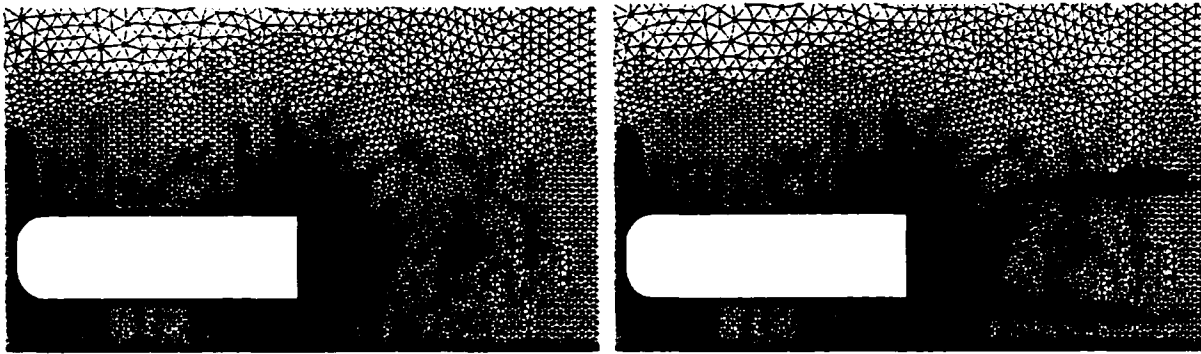
Figure 5.3 Initial mesh and refined mesh on longitudinal symmetry plane (side view) after three flow adaptations

5.3 INVESTIGATION OF FLOW SYMMETRY

The size of the computational domain (Figure 5.1b) was determined after several test runs with outer boundaries at varying distances. Although the shape is symmetric with respect to its longitudinal center plane and the oncoming flow is at zero yaw by virtue of the shape bluffness and the blunt base, the flow is expected to develop some asymmetry. To determine the extent of asymmetry, computations were performed for both full-body and half-body geometries (Figure 5.4). The asymmetry detected via the base pressure coefficients was deemed small (Baysal and Bayraktar, 2001). Despite this finding, all unsteady computations were performed on the full body configuration.
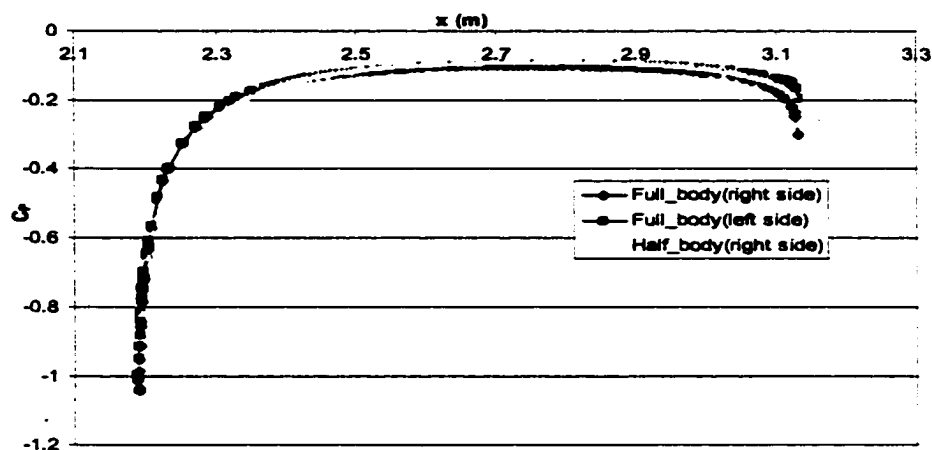
Figure 5.4 Half body versus full body comparison: Pressure coefficient variation on side walls.

5.4   PARALLEL COMPUTATIONAL EFFICIENCY

All the computations were performed in parallel mode on the 64-processor SUN HPC 10000 multiprocessor computer of Old Dominion University. Mesh partition was obtained by using Metis algorithm (AEA Tech., 1999). Figure 5.5 shows mesh partitioning on a Ahmed body computational domain. Documented by Figure 5.6 is the speed up achieved by increasing the number of the processors in comparison to the ideal speed-up. It was observed that parallel computation efficiency does not go up linearly when the number of CPU is increased. This kind of parallel computation response is mainly because of the overlapped regions in mesh partitions and communication overhead between the processors. Moreover, benchmark results about parallel performance of the computer systems that were used in this study are available in Appendix A.
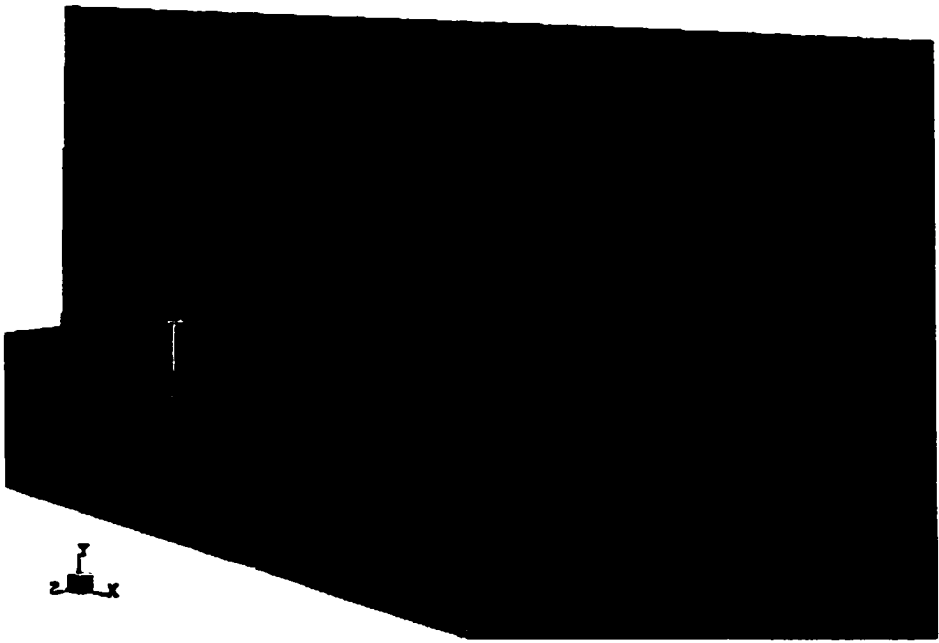
Figure 5.5 Domain partitioning using Metis algorithm
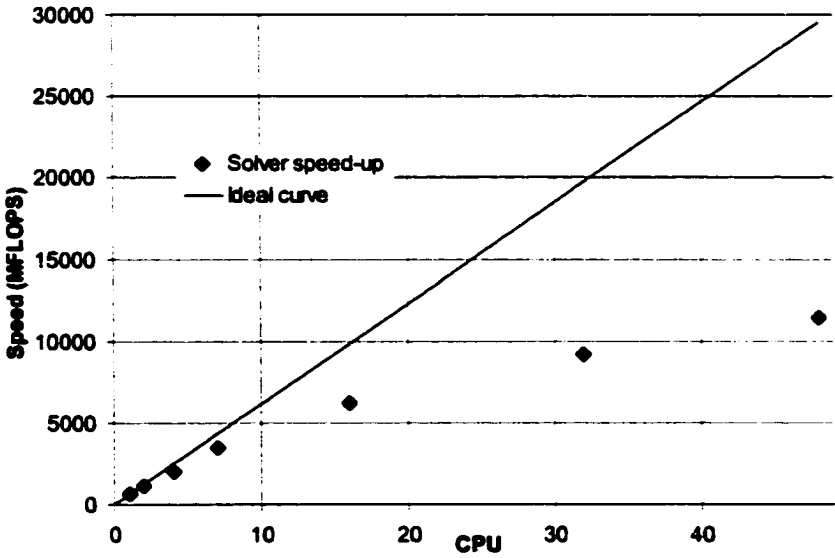
Figure 5.6 Expedite efficiency gained from parallel computations.

5.5 COMPUTED RESULTS

Presented in Figure 5.7 are the instantaneous pressure coefficient values on the top surface of the body at its symmetry plane. Although the values for different backlight angles collapse on each other during the expansion followed by the recompression near the front, the rates of the second expansion and their recovery vastly differ. These results indicate very similar trends to those reported in Ahmed et al. (1984). Further, the present computational and experimental results agree with each other fairly well.
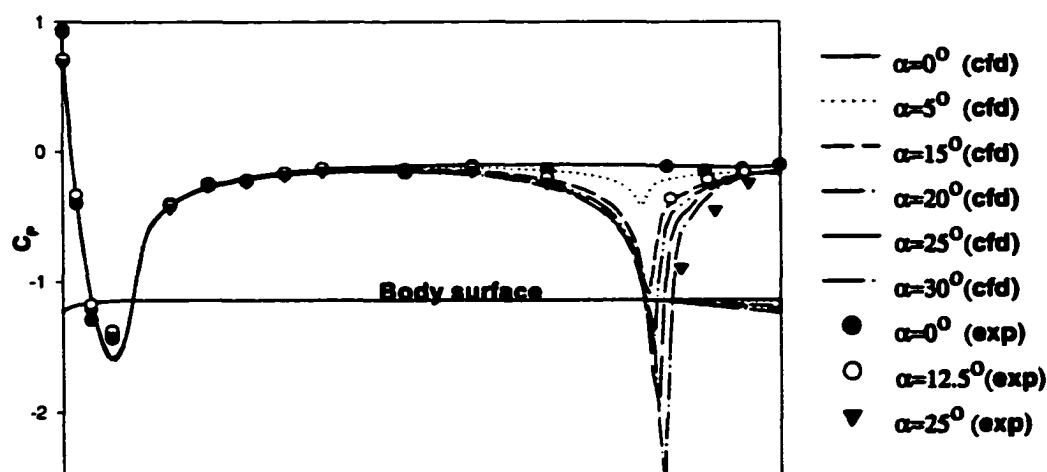
Figure 5.7 Experimental (exp) and computational (CFD) pressure coefficient distributions on the top surface at body symmetry plane for various backlight angles (with permission, from SAE 2001-01-2742).

The instantaneous force coefficients from the computations and the measurements were time averaged and plotted in Figure 5.8. As expected, the lift increases with the increasing backlight angle almost linearly. However, the drag coefficient does not show a linear change with backlight angle, and it stays in 30% range except when the backlight angle is at 30-deg. The difference between present computations and experimental measurements is less than 5%. Even though the ground clearance for present study is 3.44 times larger than Ahmed's model (Ahmed et al., 1984), the difference on drag coefficient from present

computations and Ahmed's data (Ahmed et al., 1984) is about 15%. In conclusion, the

present computations agree reasonably well with the present measurements as well as the

data from Ahmed et al. (1984).
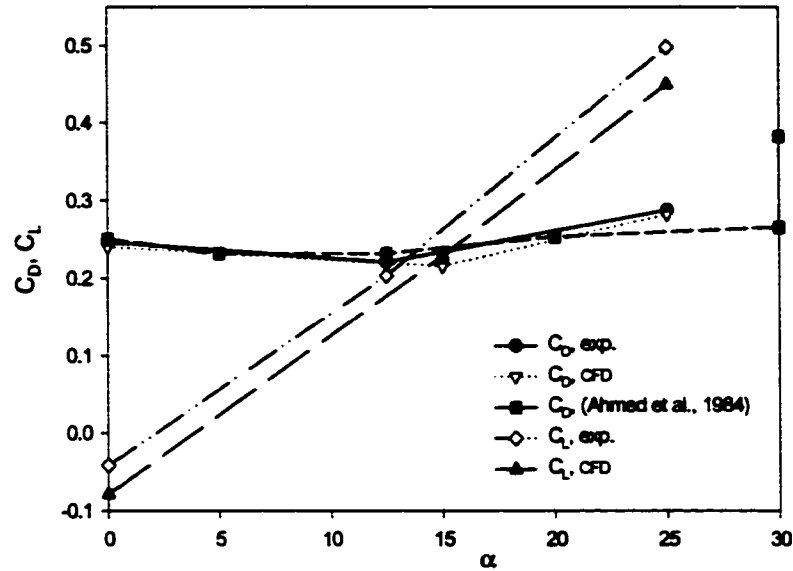
Figure 5.8 Comparisons of time-averaged drag and lift coefficients from present
computational and experimental (exp) studies and the experimental data from Ahmed et al.
(1984) (Re=4.4M) (with permission, from SAE 2001-01-2742).
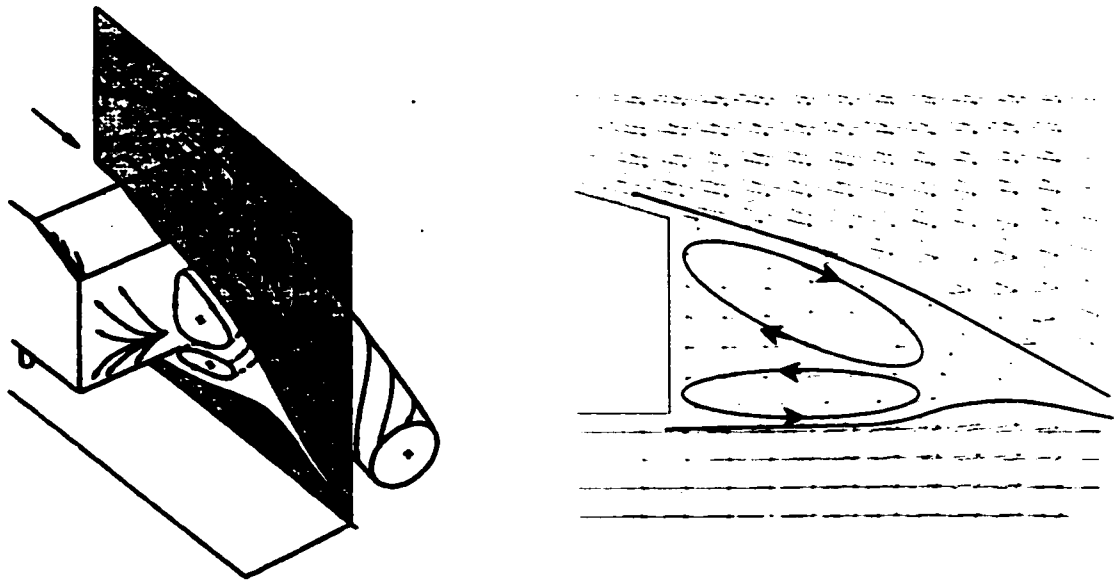
Figure 5.9 (a) Schematic view of wake flow pattern (with permission, from the Annual Review of Fluid
Mechanics, Volume 25, ©1993, by Annual Reviews www.AnnualReviews.org), (b) Velocity vector plot at longitudional
symmetry plane and recirculation regions (α=25°, Re=4.4M).

Variation of force coefficients in Figure 5.8 can be explained with the help of Figure 5.9. A schematic view of the wake pattern and a velocity vector plot at longitudinal symmetry plane of present bluff body cases are presented in Figure 5.9. Typically, two trailing vortices that come from each upper corner and two circulating regions in front of the back surface are the basis of the drag coefficient variation. Increasing backlight angle α causes stronger trailing vortices resulting drag force increase on the back surface. On the contrary, the other two circulating regions help the pressure recovery and keep the flow attached on the back surface. Induced drag also cause more drag force with higher backlight angle. In result, the total drag changes with respect to the summation of these opposite forces. Interestingly, around the 30° backlight angle, trailing vortices reach into their strongest power and generate extraordinary drag force. At that point, a small perturbation in the flow or small increase in backlight angle could lead tailing vortices to take off from model surface and lessen the drag force (Ahmed et al., 1984, Hucho, 1993). Therefore, two different drag coefficients are presented at 30° backlight angle by Ahmed (Ahmed et al., 1984).

Although six cases with different backlight angles were computed (Figure 5.10), for brevity, only the cases with backlight angles of 0-deg and 25-deg are presented herein via their instantaneous pressure contours at 0.01 sec. intervals (Figure 5.11). Since most of the unsteady phenomena occur in the back region, only one top view from both cases was plotted in Figure 5.12. Among the salient features of the flow is the clearly visible shedding of the wake vortices. The shedding from the upper and lower corners is non-symmetric due to the effect of the ground. Further, the shear layer emanating from the lower corner is weaker by the presence of the ground, which in turn weakens the vorticity concentration. The instantaneous velocity streamlines around the body at t = 0.23 sec. for 0-deg backlight

angle and Re=4.4 M flow are presented in Figure 5.13. The formation of a very formidable

wake is now visualized in three dimensions. Another visualization is presented in Figure

5.14, from both the experiments and the computations, for the top surface. The flowfield is

fairly uniform on the top surface.
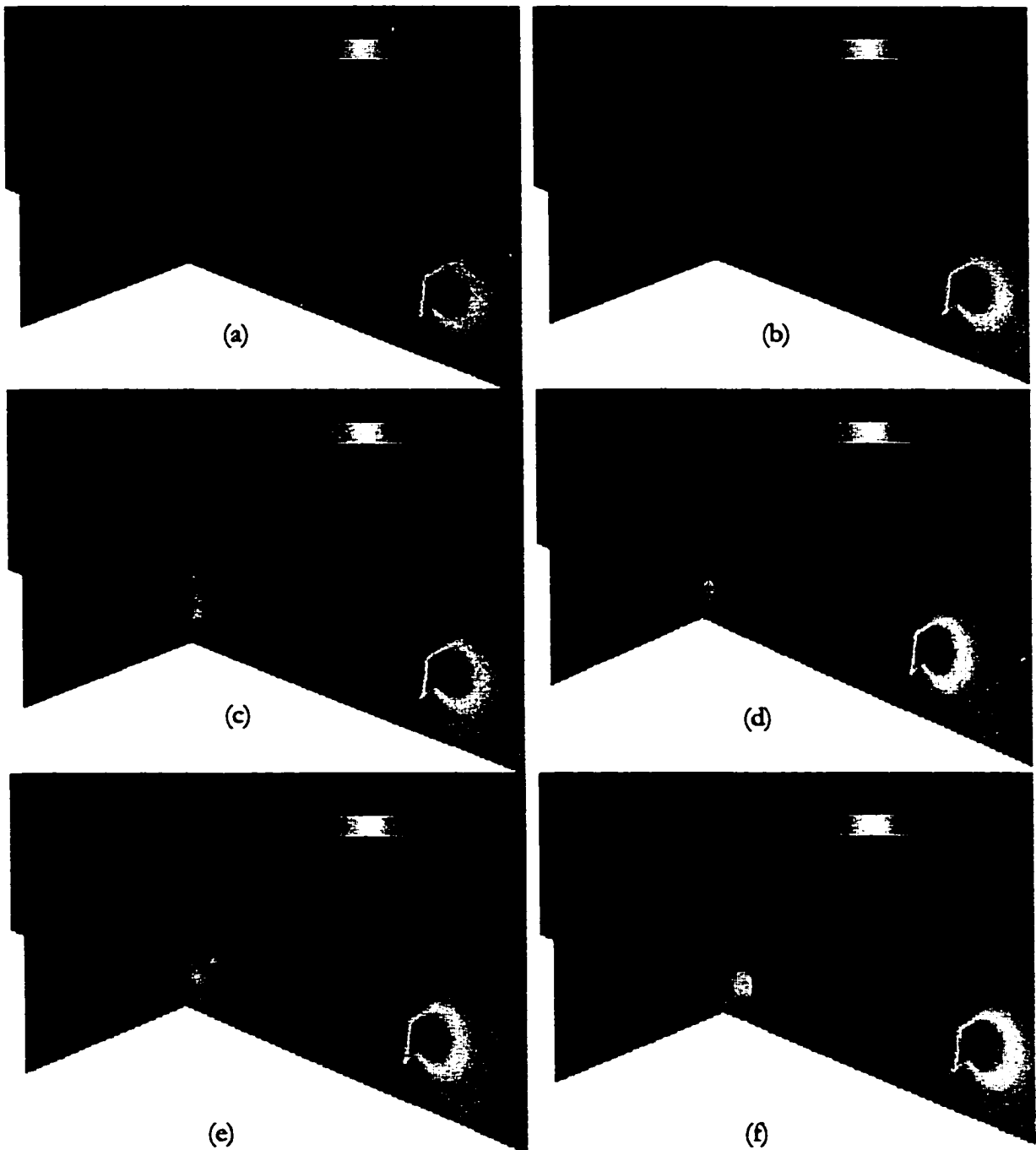
Figure 5.10 Computed instantaneous pressure contours of the longitudinal symmetry plane
(a) α=0°, (b) α=5°, (c) α=15°, (d) α=20°, (e) α=25°, (f) α=30°.
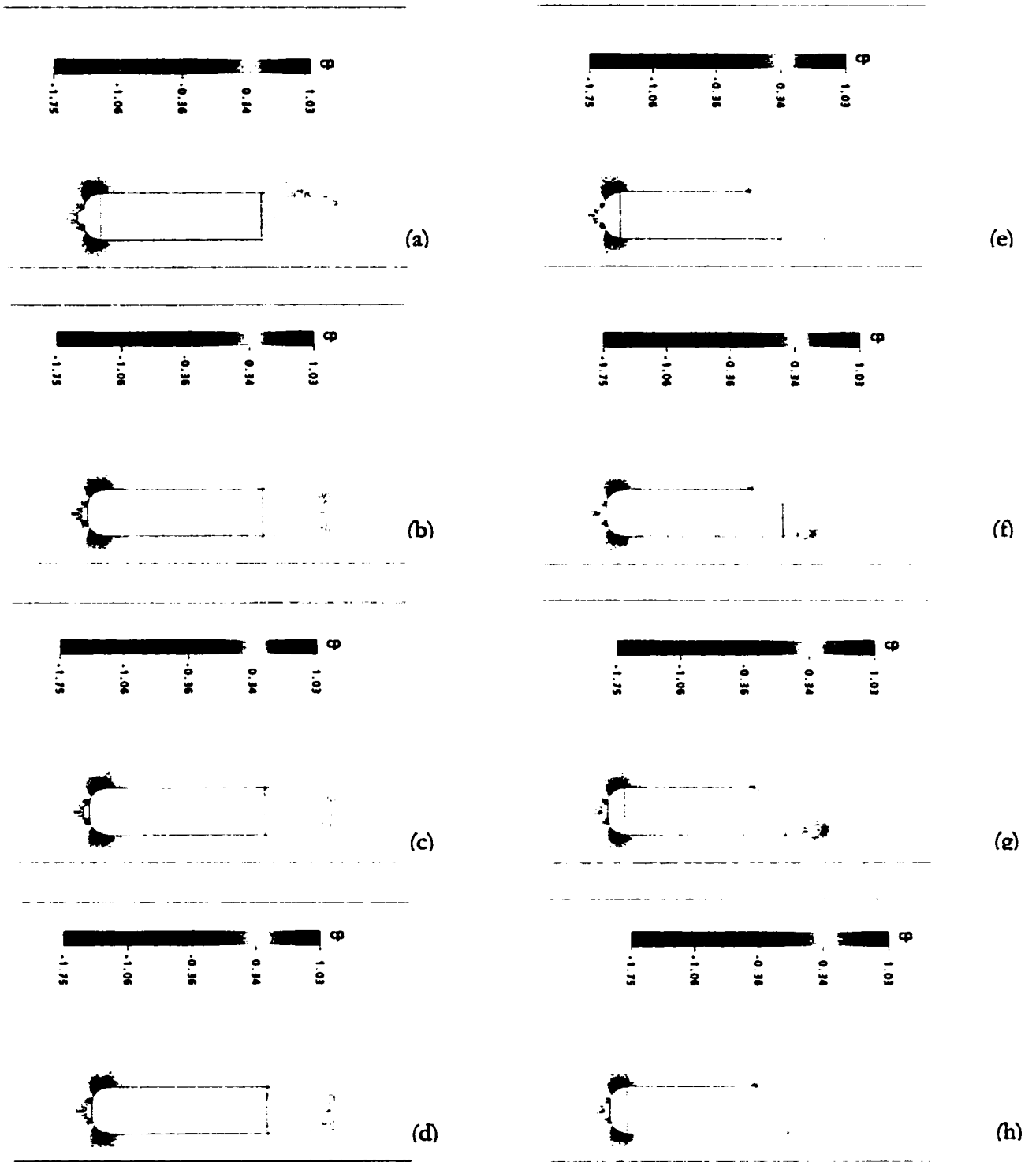
Figure 5.11 Computed instantaneous pressure contours of the longitudinal symmetry plane at t = 0.20, 0.21, 0.22, and 0.23 sec. (a)-(d) α=0°, (e)-(h) α=25° (with permission, from SAE 2001-01-2742).

(a)   (b)
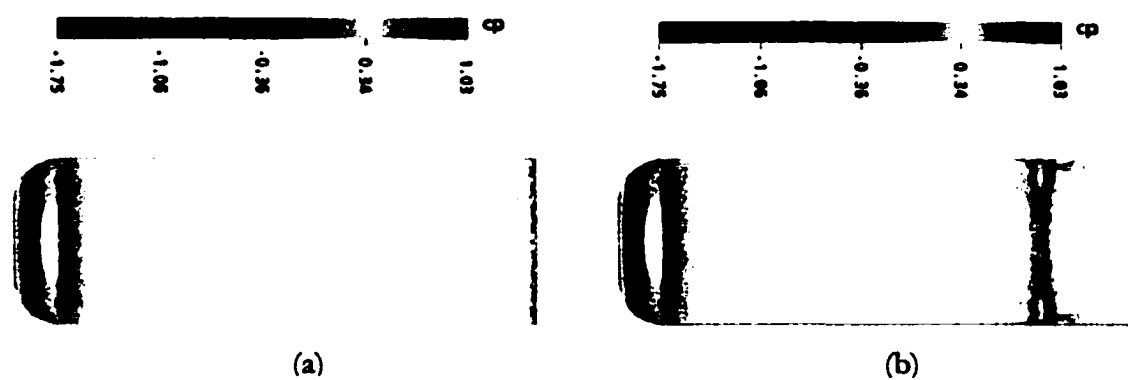
Figure 5.12 Instantaneous pressure contours on the top surface at t=0.23 sec. (a) α=0°, (b) α=25°
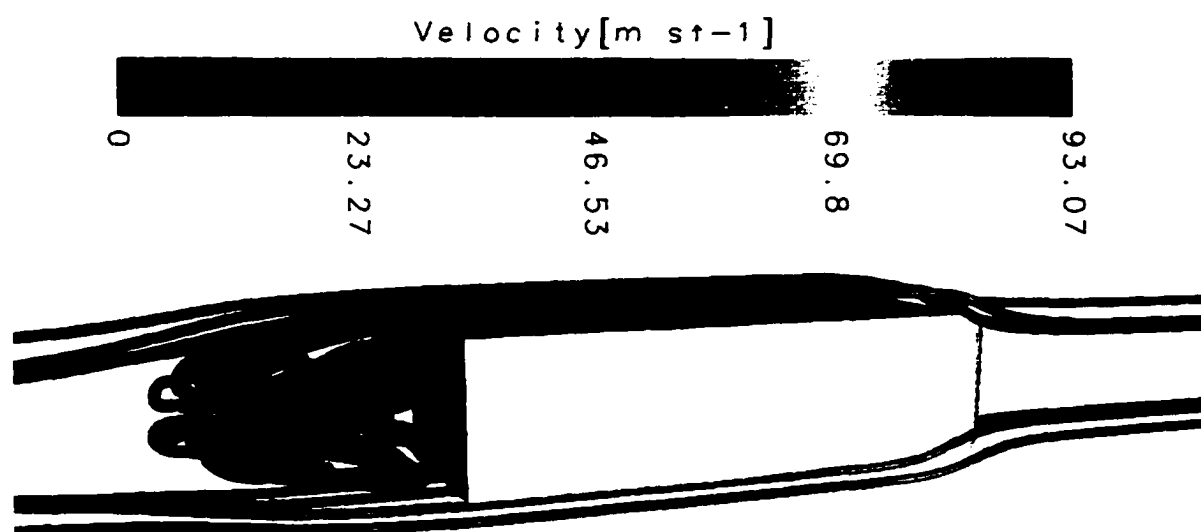
Figure 5.13 Computed instantaneous velocity streamlines at t=6.3050 sec.
(0-deg backlight angle, 60m/s freestream velocity, Re=4.4M).
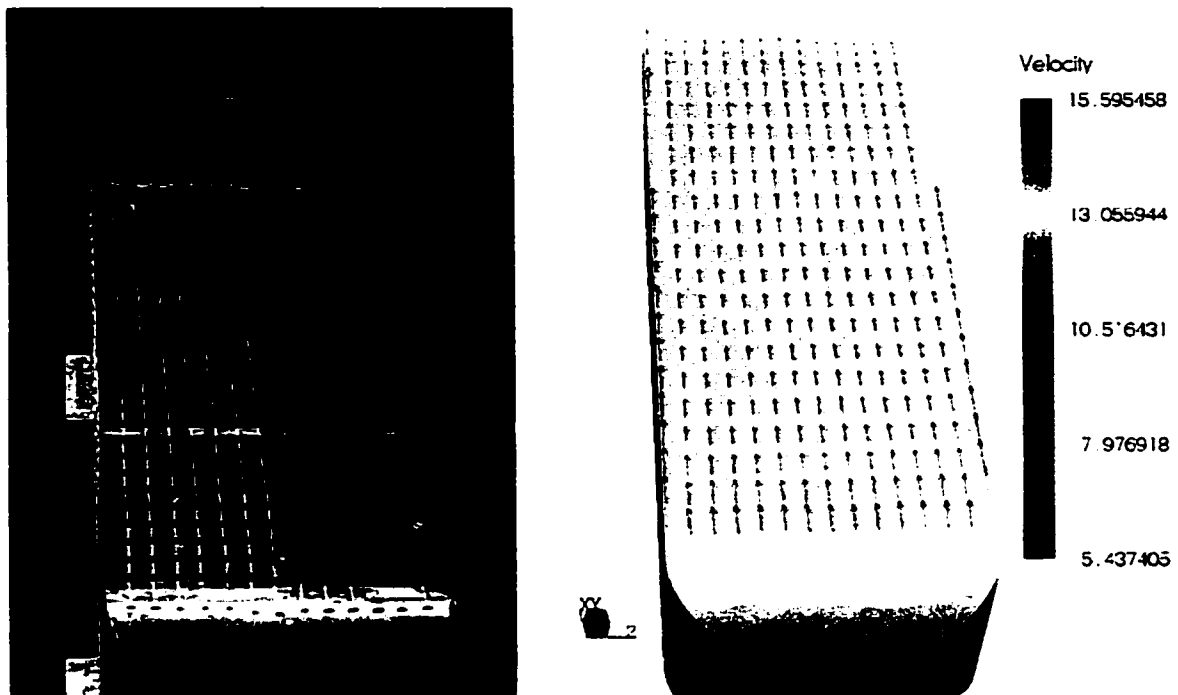
Figure 5.14 Tuft visualization from the wind tunnel and computed instantaneous vector plots on the top surface (0-deg backlight angle, Re=8.8M) (with permission, from SAE 2001-01-2742).

5.6   ANALYSIS OF TIME-DEPENDENT DATA

A time history of the unsteady forces on the body is generated during a time-accurate computational run. Figure 5.15 shows force components on the model surface versus simulation time. Although computed drag force represents the biggest component of the total aerodynamic force, fluctuations on lift force are bigger than drag force oscillation. In addition, magnitude of the side force is much smaller than the other two force components.
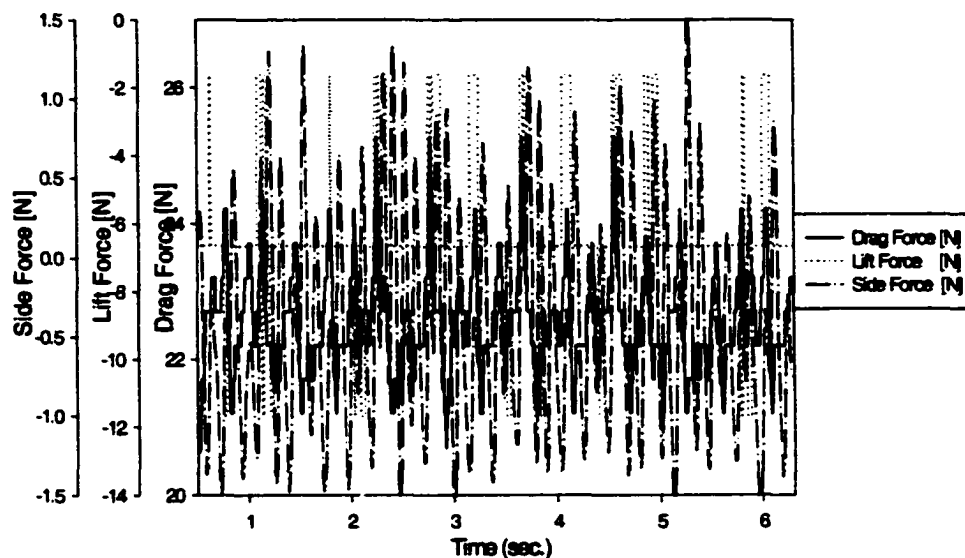
Figure 5.15 Time variation of force components on the body (0-deg backlight angle, Re=4.4 M) (with permission, from SAE 2001-01-2742).

These forces, shown in Figure 5.15, are then analyzed in the frequency domain. The power spectral density from the case with 0-deg backlight angle and Re = 4.4M, is presented in Figure 5.16 for the lift, drag and side forces. The dominant frequencies can then be used to calculate the Strouhal numbers,

$$St = \frac{f \cdot H}{U} \tag{4.2}$$

where H is the body height and U is the flow speed. The Strouhal numbers for the lift and the side force for the case in Figure 5.16 are calculated to be 0.106 and 0.086, respectively. To provide some reference values, the values from (Khalighi et al., 2001) and (Krajnovic and Davidson, 2001b) will be considered. The Strouhal number reported in (Khalighi et al., 2001b) for a similar flow but computed from its pressure fluctuations is 0.070. The Strouhal numbers reported in (Krajnovic and Davidson, 2001b), again for a similar flow but computed from its trapped vortices and trailing vortices, were 0.073 and 0.110, respectively. Therefore, the present values can be deemed in qualitative agreement with these reported results.
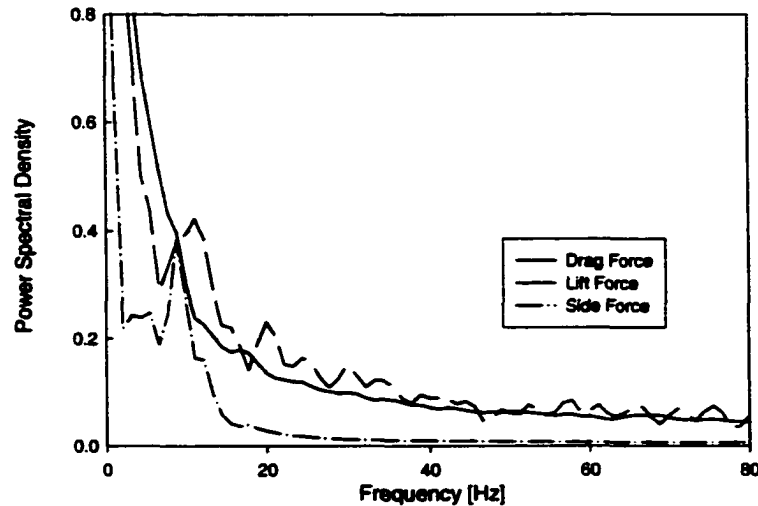
Figure 5.16 Power spectral density variation on the force data (0-deg backlight angle, Re=4.4 M) (with permission, from SAE 2001-01-2742).

Benchmark case on Ahmed Body is completed in this chapter. Computational and experimental results were presented together. Quantitative results were compared and the computational model was validated. Furthermore, tuft visualization of experimental measurements and unsteady pressure variations from computational calculations were presented for qualitative purpose. The next chapter simulates a heavy truck model based on the procedure that was followed for Ahmed Body. Knowledge obtained from this chapter lights the way for full-scale heavy truck simulations.

CHAPTER 6

COMPUTATIONS OF EXTERNAL AERODYNAMICS FOR HEAVY TRUCK

In this chapter, the computational results for the external aerodynamics of a tractor-trailer configuration are discussed. Computational procedure, which was highlighted in the previous chapter, is applied to a very complex geometry. CAD model was created using a CAE package (ProEngineer$^©$) and then imported to the CFD solver. In addition, parametric work on external geometry is conducted, and the results are presented with the help of computer visualization.

Some of the salient features of external flow of tractor-trailer configuration manifest themselves in: i) the flow conditions immediately ahead of the trailer's front grill; ii) the flow inside the gap between the tractor and the trailer; iii) the undercarriage flow; iv) the wake behind the trailer. A stagnation flow is formed immediately ahead of the tractor. An accurate computation of this region is highly dependent on the distance at which the inlet boundary is placed. The stagnation is followed by a series of expansions over the tractor resulting in the highest velocities over the canopy with their values exceeding that of the freestream. A recirculating flow with low pressures is formed in the gap region between the tractor and the trailer. This gap clearly contributes to a significant increase in the drag. The undercarriage flow resembles a distorted Couette flow due to the suction by the gap and the effects of the tires. A significant wake is formed at the trailing end of the trailer with non-symmetrical expansions from the top and the bottom corners. This further contributes to the vortex shedding as a consequence of a blunt base. In what follows, the procedure

starting from CAD model, mesh generation and boundary conditions on the computational domain will be highlighted.

6.1 COMPUTATIONAL DOMAIN AND MESH

Tractor-trailer geometry was modeled at true scale with the dimensions of 19.5m×2.5m×3.9m. The size of the computational domain is shown in Figure 6.1. Computational domain for tractor-trailer simulation was selected with the experience from the previous validation case with the dimensions of 71.0m×11.0m×12.5m. The distance between the model and farfield domain boundaries are carefully selected to minimize the spurious boundary effects.
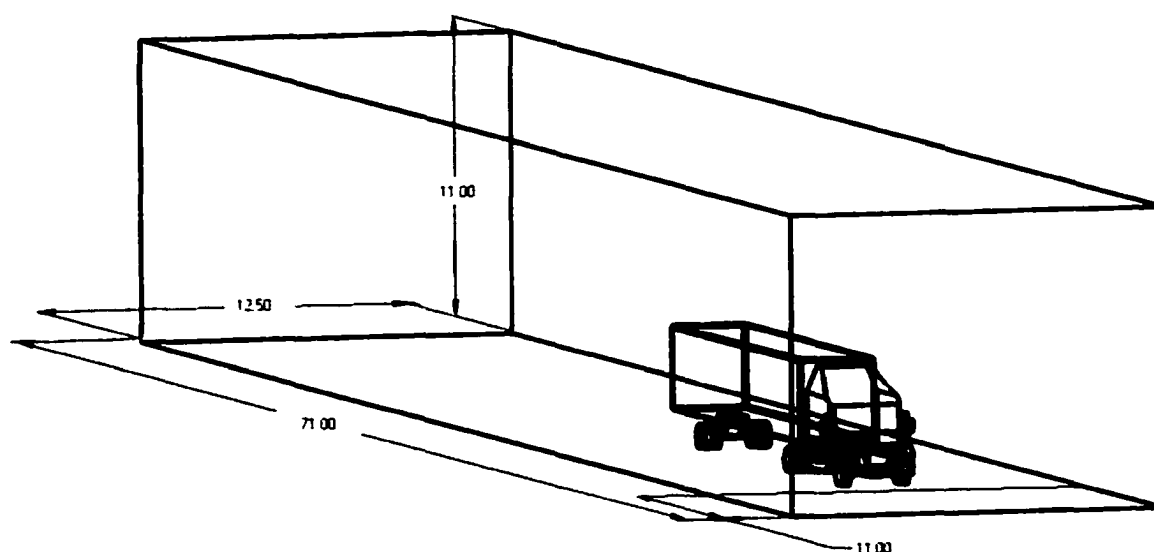
Figure 6.1 Computational domain for the tractor-trailer simulations (all units are meters).

A computer-aided-design (CAD) model of the truck is developed with the aforementioned dimensions, and then a domain mesh is generated (Sorrells, 1999). After importing these solid surfaces into a mesh generator, the volume between these surfaces and the outer boundaries is discretized using 16 million cells of hybrid shapes containing

tetrahedra, prisms and hexahedra. A view of the surface mesh is presented in Figure 6.2. Because of the boundary layer growth on the solid surfaces, this hybrid mesh has stretched prismatic elements close to the body, which are, in turn, connected to the tetrahedral cells off the surfaces. Far from the body, hexahedral elements have been used all the way to the outer boundaries (see section 3.4.1 for details).

Figure 6.2 A partial view of the computational mesh.

6.2 BOUNDARY CONDITIONS

As this is a simulation of the external flows, the size of the computational domain, shown in Figure 6.1, delineated by its outer boundaries, is a compromise between accuracy and computational efficiency. Figure 6.3 shows boundary conditions in the computational domain. The domain is bounded by the ground plane, the flow inlet boundary, the flow outlet boundary and three free-slip wall boundaries (two sides and the top). The conditions imposed at these boundaries are required to represent the effect of the events outside of the domain. The surface of the tractor and the trailer provides the internal boundaries (walls).

Floor $U_{Wall} = U_{spec}i + V_{spec}j + W_{spec}k$

Body $U_{Wall} = 0$

Outlet $\partial P/\partial n = 0$

Inlet $U_{Inlet} = U_{spec}i + V_{spec}j + W_{spec}k$

Outer walls $U_{n,Wall} = 0$, $\tau_w = 0$
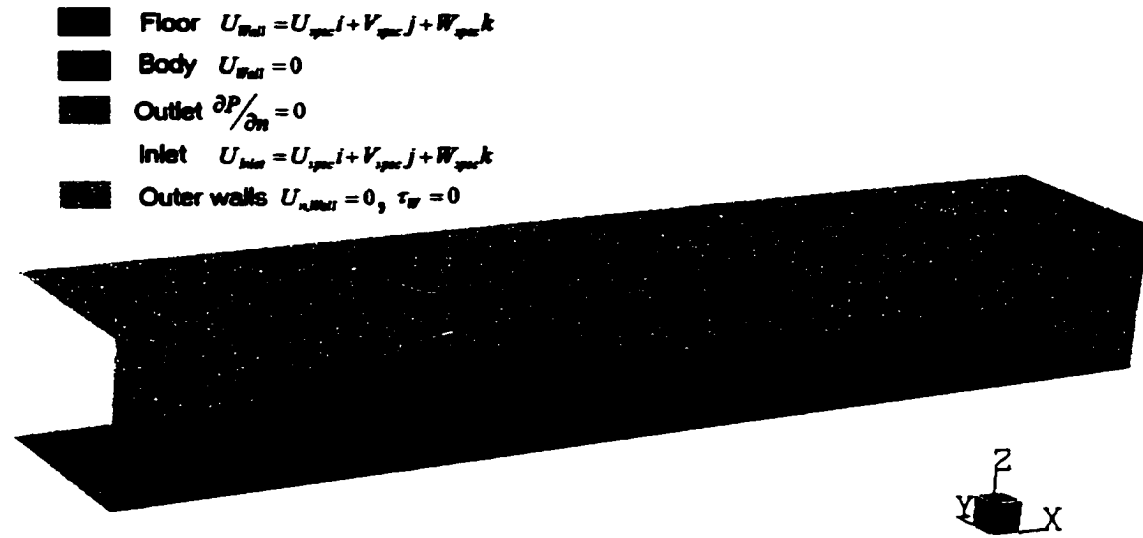
Figure 6.3 Boundary conditions for tractor-trailer configuration.

The inlet plane is located at about one-half body length ahead of the model and the magnitude of the inlet velocity (30 m/s) is specified with the direction taken to be normal to this boundary (as in a wind tunnel). Here, a uniform velocity profile is prescribed, that is, the boundary layer thickness is assumed to be zero. The prescribed condition at an open boundary allows for the fluid to cross the boundary surface in either direction. For example, all of the fluid might flow into the domain at the opening, or all of the fluid might flow out of the domain, or a mixture of the two might occur. The velocity of the fluid on the surface of the tractor and the trailer is set to zero to satisfy the no-slip condition.

On the ground boundary, the velocity of the flow is set to be equal to the flow at the inlet boundary. This emulates the ground moving with respect to the truck, as is the case on the road. In the case of wind tunnel testing, it emulates a moving conveyor belt floor.

6.3   COMPUTED RESULTS

In the aerodynamic simulation of tractor-trailer assembly, two commonly practiced engineering simplifications, tire and moving ground affects, are investigated. First, the external flow past the tractor-trailer assembly was computed with tires and moving ground boundary condition. Then, stationary ground relative to the truck (Case 2) (see, e.g., Summa (1992), Fukuda et al. (1995), Horinouchi et al. (1995) and other results from wind tunnels without moving belts) and truck without the tires (Case 3) (see, e.g., Perzon et al. (1999) for this simplification) were simulated. Table 6.1 shows case descriptions for each tractor-trailer configuration.

Table 6.1 Descriptions of truck simulation cases.

Case	1	2	3
Tires	Yes	Yes	No
Moving ground	Yes	No	Yes

Sample results are presented in Figs. 6.4-6.6, which can be contrasted to observe the effects of tires and the moving ground. As expected, the undercarriage flow is significantly different when the tires are removed. Interestingly, the flow in the gap between the tractor and the trailer is also dramatically altered. Because of the gap, there is a significant pressure loss in that region. Even more significant differences are clearly observed in the regions, where tires are located (Figure 6.6). Different pressure coefficient distributions in between Case 1 and Case 3 present that tire effect on undercarriage flow even effective on longitudinal symmetry plane. In addition, undercarriage flow is also getting affected from ground motion. When the ground is stationary with respect to the truck (Case 2), the boundary layer on the ground thickens to alter the entire undercarriage flow. The velocities

in this region are less than 10% of the freestream. The trailer wake is now skewed and driven towards the ground.
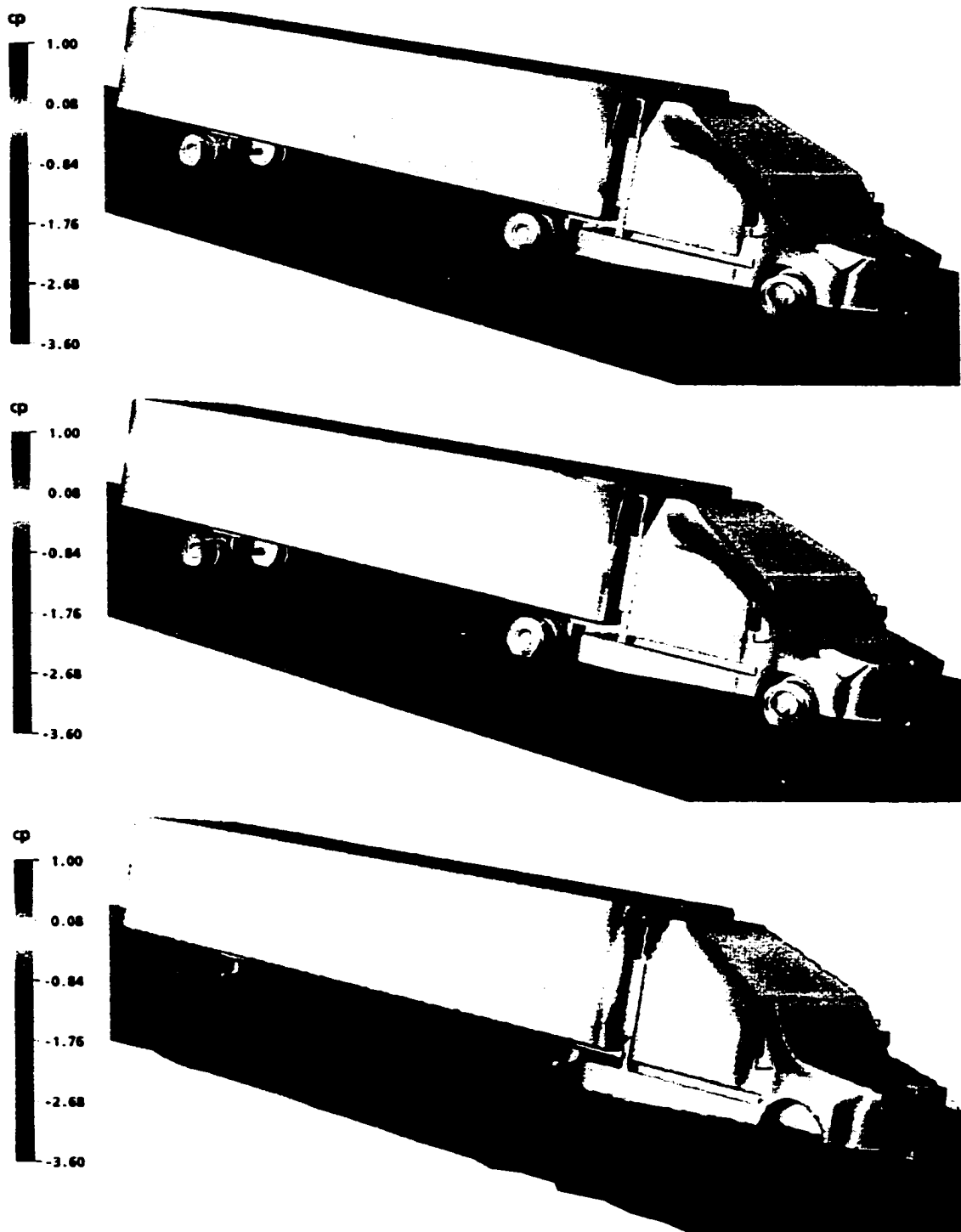
Figure 6.4 Isometric view of instantaneous pressure coefficient contours on longitudinal symmetry plane and on surface of tractor-trailer assembly. (a) Case 1, (b) Case 2, (c) Case 3.
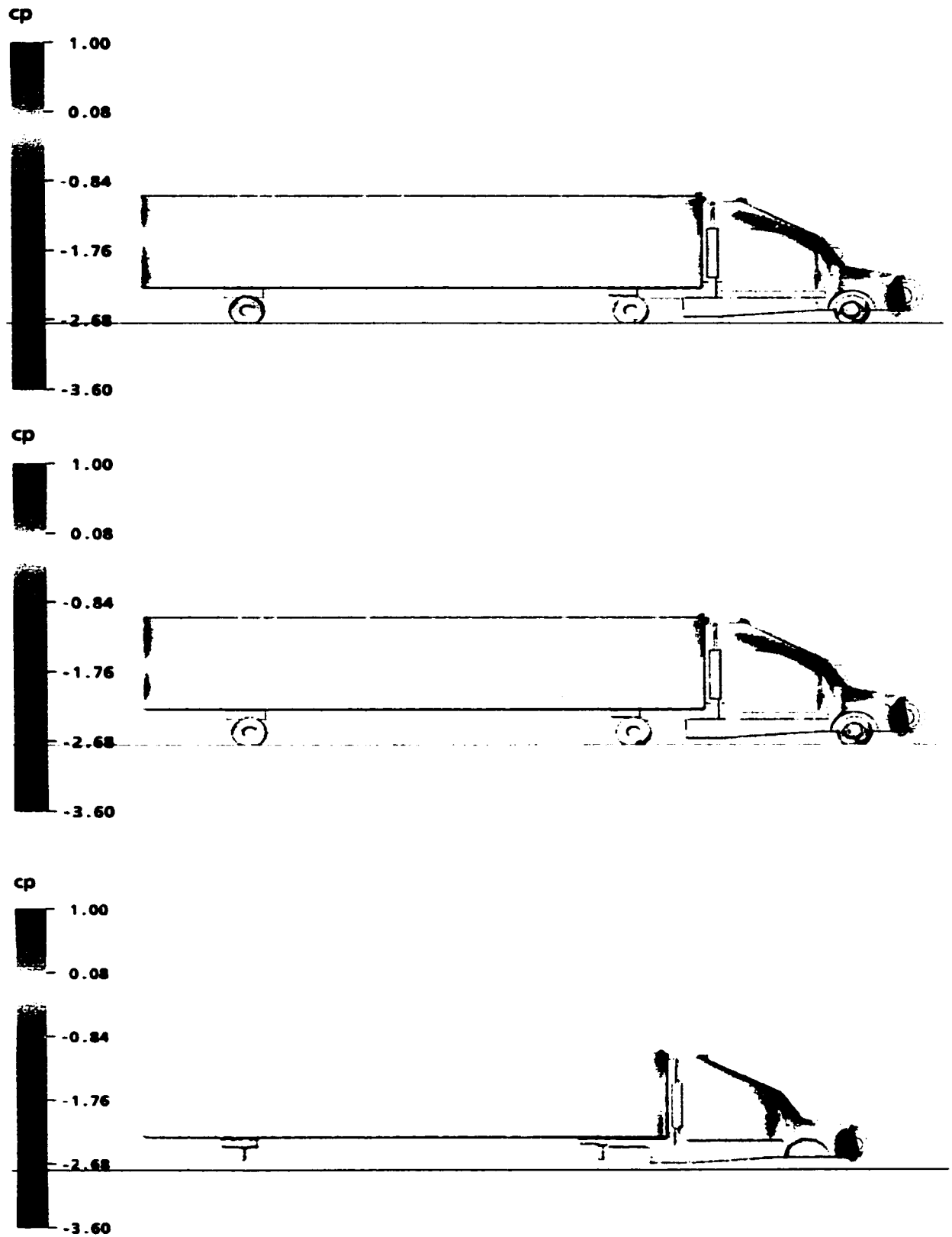
Figure 6.5 Side view of instantaneous pressure coefficient contours on longitudinal symmetry plane and on surface of tractor-trailer assembly. (a) Case 1, (b) Case 2, (c) Case 3.

Pressure coefficient distributions on the longitudinal symmetry plane of computational domain in Figure 6.4 and 6.5 are reduced on tractor-trailer assembly symmetry surface and plotted in Figure 6.6. Although the values for different configurations collapse on each other, the values for Case 3 are slightly differs on lower surface because of the tire effect. The biggest pressure jump in the symmetry plane occurs at the tractor-trailer gap region causing huge expansion and recompression on pressure coefficient values.
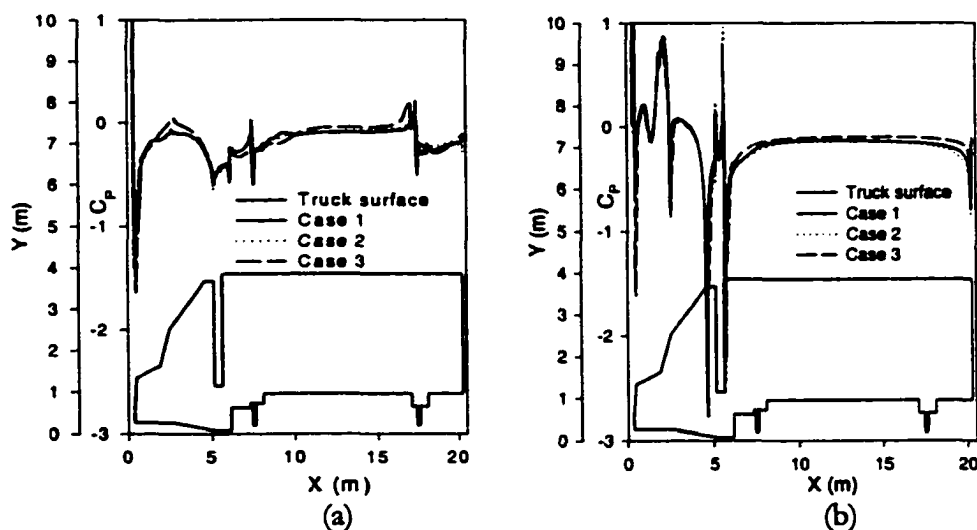
Figure 6.6 Pressure coefficients on the longitudinal symmetry plane of tractor-trailer configuration. (a) lower surface, (b) upper surface.

After summation of the force data on the surfaces of the tractor-trailer assembly, drag coefficient values are presented in Figure 6.7. The results show that the computed drag value at Case 3 is about 13.3% less as a result of removing the tires. Drag difference occurs in Case 2 because of the stationary ground (simulates wind tunnel without a moving belt), thus, the total computed drag value reduces by 4.8%. In addition, total drag coefficient is split up to its components to analyze the local drag force on the body, the tires and the mirrors (Figure 6.7). As expected, most of the drag (82.9%) comes from tractor-trailer body. Tires and mirrors contribute 12.5% and 4.6% respectively, of the total drag coefficient.

Although the effect of the local components on drag coefficient depends on the overall vehicle design, present study shows that presence of tires and moving ground increase the drag coefficient. The similar results were also obtained in the literature (Hucho, 1998).
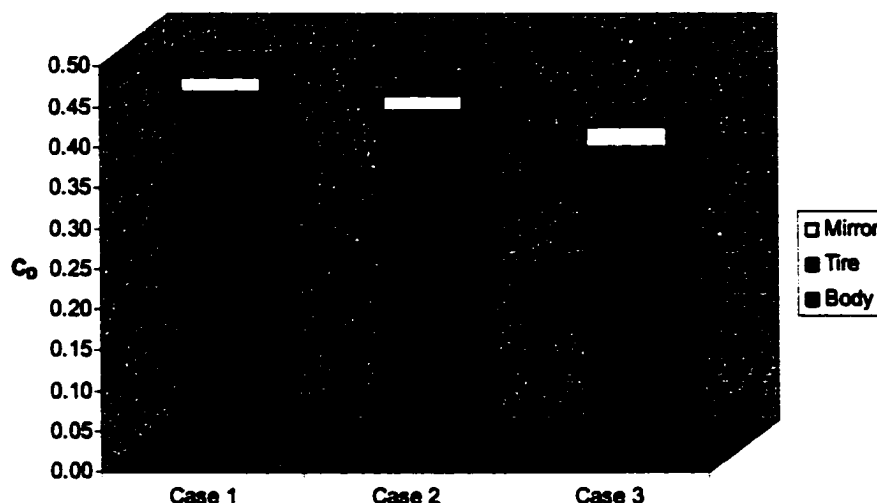
Figure 6.7 Drag coefficients and their components for each tractor-trailer configuration case.

The wake flow, which is one of the most important features of bluff body aerodynamics, is presented in Figure 6.8 and Figure 6.9. Superimposed in Figure 6.8 are the instantaneous velocity streamlines in the computational domain and the pressure coefficient contours on the model surface and the floor. When steady ground (Case 2) and moving ground (Case 1) cases are compared, it is observed that moving ground generates a larger wake region while the other wake vanishes on the steady ground. On the other hand, because of the relatively higher undercarriage velocities, the wake region is more off the ground in the case without the tires (Case 3) than it is with the tires (Case 1). This phenomenon is also clearly seen in Figure 6.9.

In order to visualize complex wake flow behind the tractor-trailer assembly, velocity vectors in the wake region are plotted on cross-section planes. The first at cross-section is

taken just before the rear end of the trailer, and all of the others follow at one-meter intervals. A total of eleven cross-section planes are plotted for each case, and each column in Figure 6.9 represents a different case.
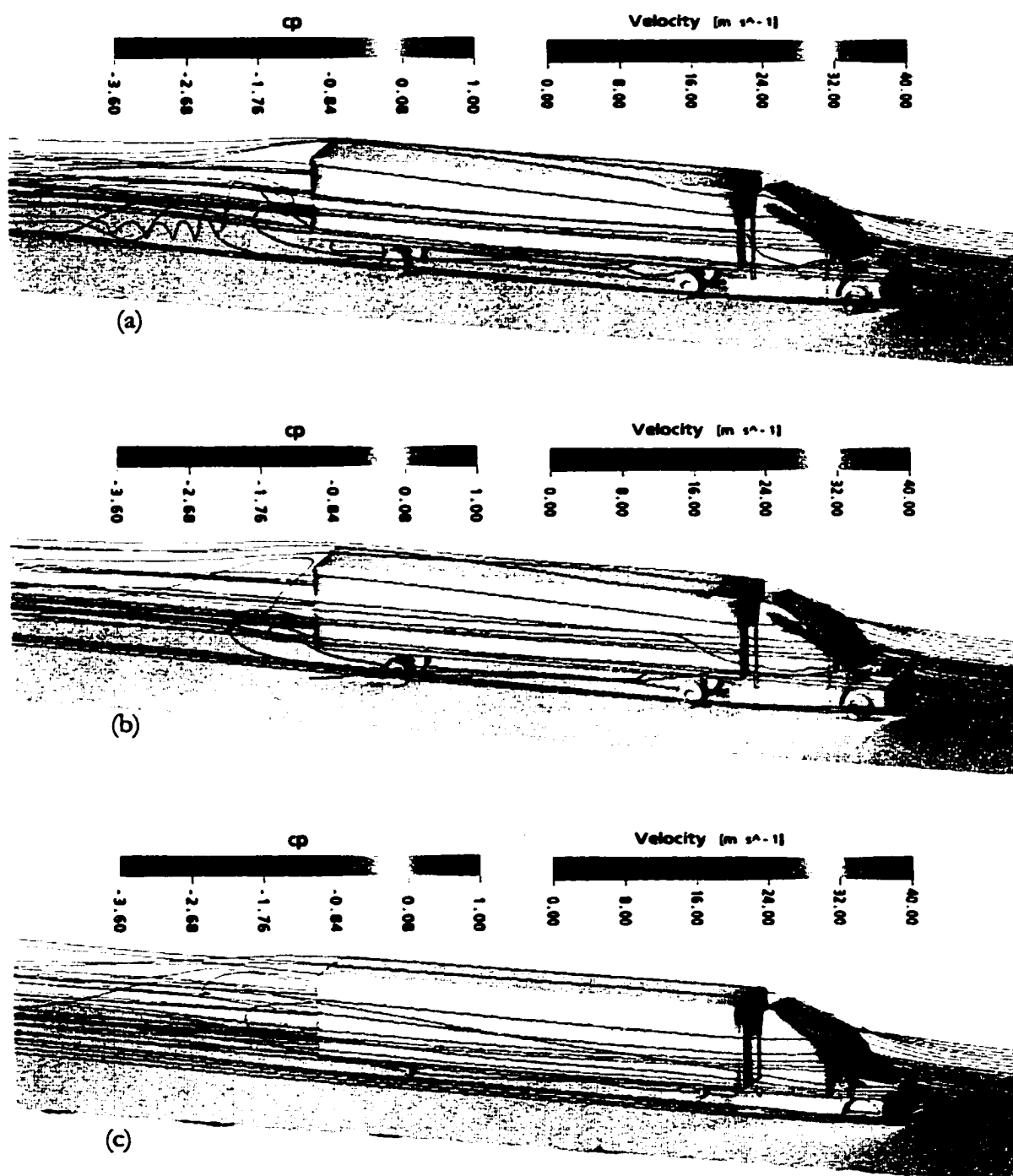
Figure 6.8 Instantaneous pressure coefficient contours on the surface of tractor-trailer assembly and instantaneous velocity streamlines. (a) Case 1, (b) Case 2, (c) Case 3.
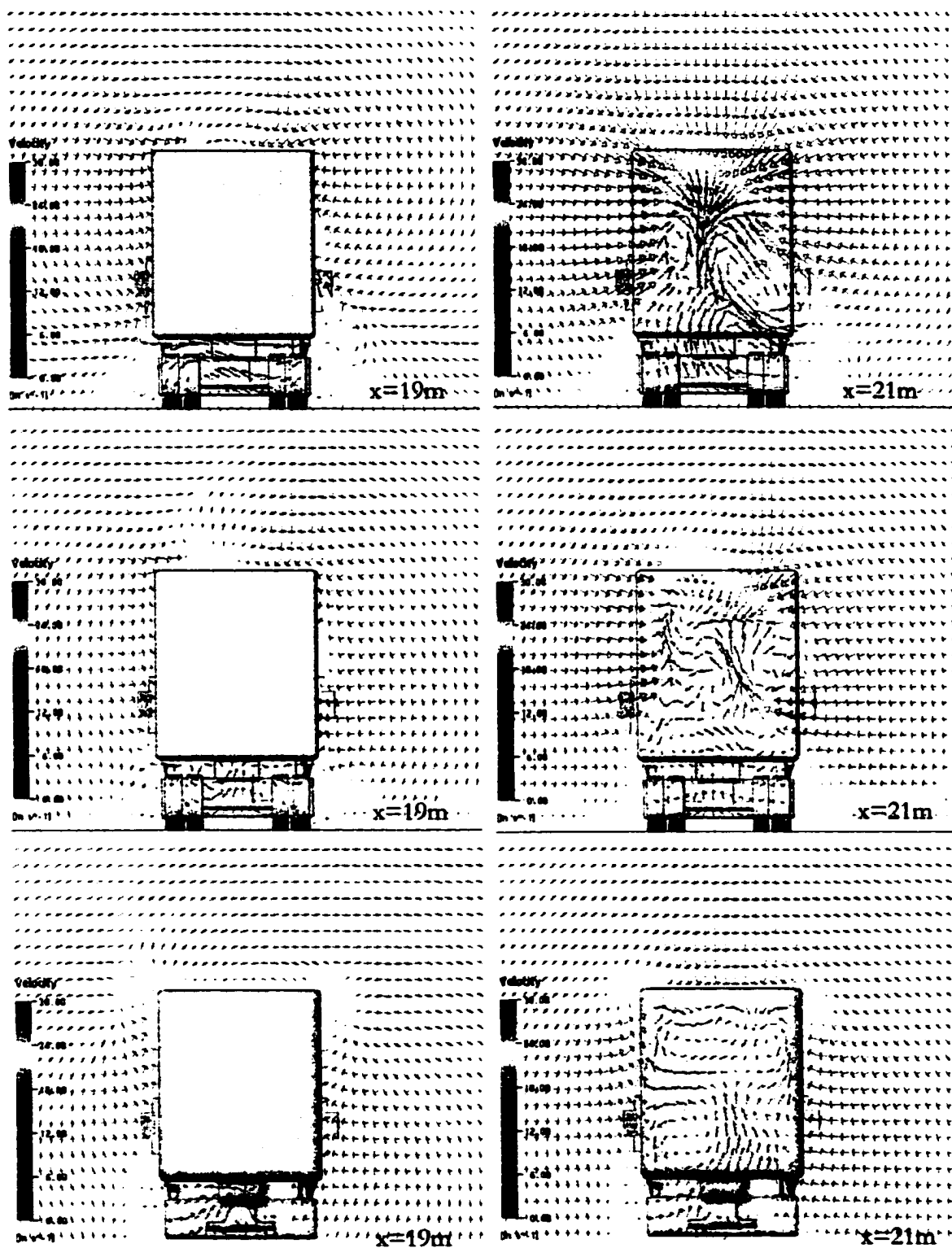
Figure 6.9 Instantaneous velocity vectors in the wake region of tractor-trailer assembly at different distances from the model base. First row: Case 1, Second row: Case 2, Third row: Case 3 (continued).
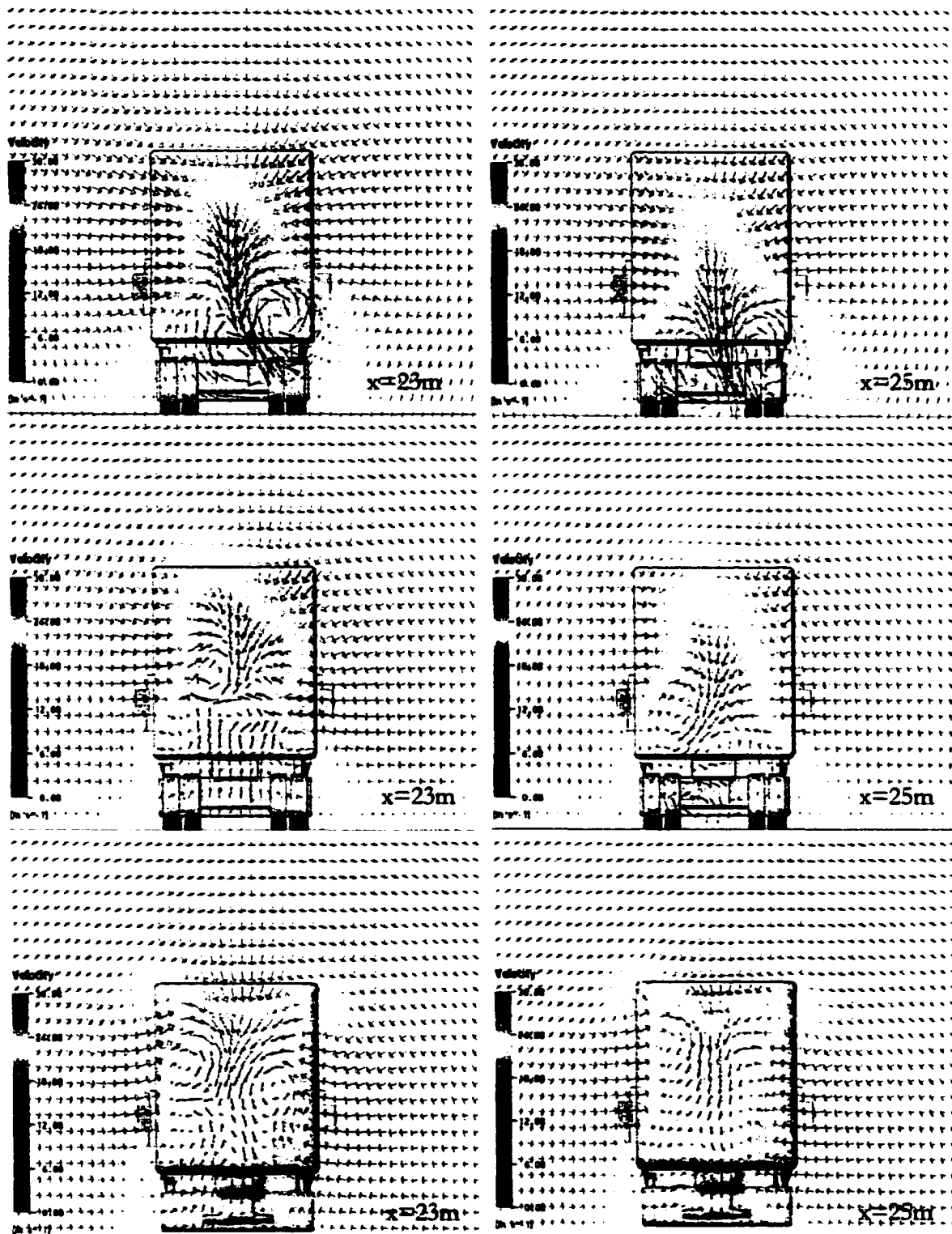
Figure 6.9 Instantaneous velocity vectors in the wake region of tractor-trailer assembly at different distances from the model base. First row: Case 1, Second row: Case 2, Third row: Case 3 (continued).

Figure 6.9 Instantaneous velocity vectors in the wake region of tractor-trailer assembly at different distances from the model base. First row: Case 1, Second row: Case 2, Third row: Case 3 (concluded).

The first thing that attracts attention is the wake structure, which is completely three-dimensional in all cases. Even the formation and dissipation of side vortices are clearly seen, especially in Case 1 and Case 3. Because of the sudden expansion, the secondary circulations regions are remarkably noticeable. In addition, the steady ground boundary condition unveils itself when closer to the ground in Case 2. Case 1 and Case 3 show no boundary layer region on the ground, while the lower velocities exist in Case 2. Another interesting feature is noticed in Case 3. After 10 meters behind the rear end of the model, the wake regions in Case 1 and Case 2 start to dissipate onto the ground. However, wake flow in Case 3 holds off ground with the help of stronger undercarriage flow.

CHAPTER 7

CONCLUSIONS AND RECOMMENDATIONS FOR FUTURE WORK

Understanding external aerodynamics of a ground vehicle is a prerequisite for low-drag ground vehicle design. With this impetus, the external aerodynamics of a tractor-trailer assembly was simulated using computational fluid dynamics and the external flow was presented using computer visualization.

In this dissertation, a method of Computational Fluid Dynamics (CFD) has been setup and successfully applied to ground vehicle aerodynamics. In the course of the computations, experimental validations of each case, procedures and implementations to the problem have been discussed. In the following, a summary of the achievements and conclusions in each of the aforementioned cases is presented.

7.1 SUMMARY

In the first half of this dissertation, a brief introduction and a literature survey for the ground vehicle aerodynamics are presented, which are followed by, motivation and the objectives of the present work. Following the description of the computational methodology for the external aerodynamics of an Ahmed body was studied. In the computational portion of the study, time-dependent, three-dimensional, Reynolds-averaged Navier Stokes (RANS) equations were solved using a finite volume method. The RNG k-ε model was elected for the closure of the turbulent quantities. Several concerns, such as mesh density, far field boundary location, validity of flow symmetry and parallel computational efficiency, were also investigated.

In the experimental aspect of the Ahmed body case, full-scale wind tunnel experiments were conducted at Langley Full Scale Wind Tunnel. The pressure distributions on the longitudinal symmetry plane and the side planes were measured. Reynolds number dependency and wind averaged drag coefficients were also calculated for each of the experimental cases. The results from both experimental and computational methods were presented for different backlight angles and compared with each other. Then, pressure and force coefficients along with qualitative measurements were compared, and the computational method was validated for ground vehicle aerodynamics.

Discussed in the second half of the dissertation are the computational method, its application to a full-size tractor-trailer assembly and the conducted parametric study. In order to analyze tire and moving ground effects for the sake of wind tunnel testing, a case without tires, and another case with steady ground were simulated. Results were contrasted with each other. Drag coefficients for each case were calculated and the errors, which come from the removal of tires and the stationary ground simplifications, were estimated. In addition, drag force on mirrors and tires were calculated separately, so the components of drag coefficient could be presented. Furthermore, the wake flow for tractor-trailer assembly was simulated and depicted with velocity vector plots in the region, and the flow characteristics in the wake were compared to understand the effects of tire and moving ground.

7.2 CONCLUSIONS

In the section on computational code validation, a comprehensive analysis was conducted on Ahmed Body geometry. Parallel computations, domain and mesh size efficiency studies were conducted. About 5.4 million mesh elements were used for parallel Ahmed Body computations. Pressure and force coefficients were determined both from

CFD and the experimental measurements. The computed and measured pressure coefficients presented a good agreement with each other. Although C_D was slightly underpredicted, variations with backlight angle followed the same trend as observed in the experimental data. It was observed that C_L increased very rapidly with increasing backlight angle with a switch from downward force to an upward force at about 3°. During the analysis of time dependent force data, Strouhal number for lift and side force were calculated to be 0.106 and 0.086, respectively. Moreover, Reynolds number dependency was investigated in the experimental part of the study, and interestingly, it was observed that drag coefficient only changes about 3.5% in the range of Reynolds numbers from 2.2 million to 13.2 million.

In the computations of external aerodynamics of heavy trucks, two commonly practiced engineering simplifications, removal of tires and moving ground effects, were investigated. In order to compare their influence on drag coefficient, the external flow of the tractor-trailer assembly was computed with and without the tires, then with or without ground motion. It was concluded that differences were −13.3% for the tires and −4.8% for steady ground. From the surface pressure distributions, it was noted that tractor-trailer gap caused big pressure losses, and even tires on the side of the body had significant affect on the pressure in the longitudinal symmetry plane. When drag values were investigated, it was shown that most of the drag force (82.9%) come from tractor-trailer body. Tires and mirrors contributed 12.5% and 4.6%, respectively, of total drag.

7.3 RECOMMENDATIONS FOR FUTURE WORK

Based on the experience gained in this work with ground vehicle aerodynamics, an extension to the under-the-hood flow and heat transfer studies remains to be investigated. Conceivably, present external flowfield simulations can be used as initial conditions for

detailed simulation of add-on devices, such as mirrors, antenna and windshield design. Also, these results can be used to determine the truck's stability for safe handling and the minimization of adverse interactions with other vehicles on the road.

For the computational studies, turbulence modeling for such bluff body flows is an open area for further investigations. Since none of the turbulence models is designed for unsteady flows, accurate turbulence modeling of unsteady wake behind a ground vehicle remains as a future study.

Mesh adaptation in the present study was not time dependent. Therefore, time-dependent mesh adaptation would be beneficial for wake flow simulation of such bluff body problems. Furthermore, since resolving the wake flow requires smaller mesh size, time-dependent mesh refinement reduces the computation time and improve accuracy.

The 4-gigabyte memory allocation limit for 32-bit operating systems remains a limit for large-size computations on PC based computers. At the time of the present study, there are some operating systems are available for 64-bit calculations. Although large eddy simulation and direct numerical simulation of such complex geometries are still not possible today, fast development on computational hardware and parallel computation in the near future seems promising.

REFERENCES

Abbott, I.H., and Von Doenhoff, A.E., 1959, Theory of Wing Sections, Dover Publishers, New York, NY.

AEA Tech., 1999, CFX-5 Solver and Solver Manager, AEA Technologies, Pittsburgh, PA.

Ahmed, S. R., Ramm, G., and Faltin, G., 1984, "Some Salient Features of the Time-Averaged Ground Vehicle Wake," SAE Paper 840300, SAE International Congress and Exposition, Detroit, MI.

Anagnost, A., Alajbegovic, A., Chen, H., Hill, D., Teixeira, C., and Molving, K., 1997, "Digital Physics Analysis of Morel Body in Ground Proximity," SAE Paper 970139, SAE International Congress and Exposition, Detroit, MI.

Aoki, K., Ohbayashi, T., Zhu, M., and Miyata, H., 1993, "Finite-Volume Simulation of 3-D Vortical Flow-Fields About Road Vehicles with Various After-Body Configuration," SAE Paper 931896, SAE International Congress and Exposition, Detroit, MI.

Axon, L., Garry, K., and Howell, J., 1999, "The Influence of Ground Condition on the Flow Around a Wheel Located Within a Wheelhouse Cavity," SAE Paper 1999-01-0806, International Congress and Exposition, Detroit, MI.

Bauer, T. B., and Servais, R. A., 1974, "An Experimental and Analytical Investigation of Truck Aerodynamics,"

Bayraktar, I., Landman, D., and Baysal, O., 2001, "Experimental and Computational Investigation of Ahmed Body for Ground Vehicle Aerodynamics," SAE Paper, 2001-01-2742, International Truck and Bus Meeting and Exposition, Chicago, IL.

Baysal, O., 1999, "Aerodynamic Shape Optimization: Methods and Applications," *SAE Transactions: Journal of Aerospace*, **108**, Section 1, pp. 794-802.

Baysal, O., and Bayraktar, I., 2001, "Unsteady Wake Behind a Bluff Body in Ground Proximity," FEDSM2001-18208, ASME Fluids Engineering Division Summer Meeting, New Orleans, LA.

Baysal, O., and Bayraktar, I., 2000, "Computational Simulations for External Aerodynamics of Heavy Trucks: Effects of Tires and Moving Ground," SAE Paper 2000-01-3501, *Journal of Commercial Vehicles*, **109**, sec. 2, pp. 813-819.

Baysal, O., and Luo, X., 1999, "Dynamic Unstructured Method for Relative Motion of Multibody Configuration at Hypersonic Speeds," *Journal of Aircraft*, **36**, No. 4, pp. 725-728.

Baysal, O., and Meek, T. L., Jr., 2002, "Computational Aerodynamics of a Winston Cup Series Race Car," FEDSM 2002-31371, Proceedings of ASME Fluids Engineering Division Summer Meeting, Montreal, CA.

Bradley, R., 2000, "Technology Roadmap for the 21st Century Truck Program, A Government-Industry Research Partnership," DOE Technical Report 21CT-001.

Duell, E.G, and George A. R., 1992, "Unsteady Wake Flow of Ground Vehicle Bodies," AIAA-92-2641-CP, 10th AIAA Applied Aerodynamics Conference, Palo Alto, CA.

Elankumaran, K., 1997, "Numerical Investigation of an Inflatable Aerodynamic Boattail for Tractor-Trailers," Master Thesis, Mechanical Engineering Department, Texas Tech University.

Englar, R. J., 2000, Development of Pneumatic Aerodynamic Devices to Improve the Performance, Economics and Safety of Heavy Vehicles," SAE Paper 2000-01-2208, Government/Industry Meeting, Washington, DC.

Fukuda, H., Yanagimoto, K., China, H., and Nakagawa, K., 1995, "Improvement of vehicle aerodynamics by wake control," *JSAE Review*, **16**, pp. 151-155.

Gatski, T. B., Hussaini, M. Y., and Lumley, J. L., 1996, Simulation and modelling of turbulent flows, Oxford University Press, Oxford, UK.

Galperin, B. A., and Orszag, S. A., 1993, Large Eddy Simulation of Complex Engineering and Geophysical Flows, Cambridge University Press.

Gleason, M., Hackett, J., Han, T., and Sumantran, V., 1998, Developments in Vehicle Aerodynamics, SP-1318, Society of Automotive Engineers, Inc.

Grosso, R., and Greiner, G., 1998, "Hierarchical Meshes for Volume Data," Proceedings of Computer Graphics International '98, Hannover, Germany.

Gutierrez, W. T., Hassan, B., Croll, R. H., and Rutledge, W. H., 1996, "Aerodynamics Overview of the Ground Transportation Systems (GTS) Project for Heavy Vehicle Drag Reduction," SAE Paper 960906, International Congress and Exposition, Detroit, MI.

Han, T., 1989, "Computational Analysis of Three-Dimensional Turbulent Flow Around a Bluff Body in Ground Proximity," *AIAA Journal*, **27**, No. 9, pp.1213-1219.

Hassan, B., Gutierrez, W. T., Wolfe, W. P., Walker, M. A., Ruefer, B. G., and Hurt, W., 1995, "Numerical Prediction of Aerodynamic Drag for Heavy Ground Transportation Vehicles," AIAA-95-1913-CP, 12th AIAA Computational Fluid Dynamics Conference, San Diego, CA.

Horinouchi, N., Kato, Y., Shinano, S., Kondoh, T., and Tagayashi, Y., 1995, "Numerical Investigation of Vehicle Aerodynamics with Overlaid Grid System," SAE Paper 950628, SAE International Congress, Detroit, MI.

Hucho, W. H., 1998, Aerodynamics of Road Vehicles, SAE Publishing, Warrendale, PA.

Hucho, W. H., Janssen, L. J., and Emmelmann, H. J., 1976, "The Optimization of Body Details – a Method for Reducing the Aerodynamic Drag of Vehicles," SAE Paper 760185.

Hucho, W. H., and Sovran, G., 1993, "Aerodynamics of Road Vehicles," *Annual Review of Fluid Mechanics*, **25**, pp. 485-537.

Hwang, J., Lee, B. S., Park, Y., and Lee, D. H., 2001, "Numerical Investigations on the Flowfield Around a Square Cylinder at Ground Proximity," AIAA 2001-0600, 39th Aerospace Sciences Meeting and Exhibition, Reno, NV.

Hytopoulos, E., Andra, R., Kumar, K., and Sun, R. L., 1998, "The Effect of Boundary and Geometry Simplification on the Numerical Simulation of Front-End Cooling," SAE Paper 980395, International Congress and Exposition, Detroit, MI.

Kamm, W., Schmid, C., Riekerd, P., and Huber, L., 1934, "Einfluss der Reichsautobahn auf die Gestaltung der Kraftfahrzeuge," *Automobiltech Z.*, **37**, pp. 341-354.

Katz, J., 1995, New Directions in Race Car Aerodynamics, Robert Bentley Publishers, Cambridge, MA.

Kettinger, J. N., 1982, "Tractor-Trailer Fuel Savings with an Aerodynamic Device – A Comparison of Wind Tunnel and On-Road Tests," SAE Paper 820376, International Congress and Exposition, Detroit, MI.

Khalighi, B., Zhang, S., Koromilas, C., Balkanyi, S., Bernal, L., Iaccarino, G., and Moin, P., 2001, "Experimental and Computational Study of Unsteady Wake Flow behind a Bluff Body with a Drag Reduction Device," SAE Paper 2001-01-1042, SAE World Congress, Detroit, MI.

Kim, M. S., and Geropp, D., 1998, "Experimental Investigation of the Ground Effect on the Flow Around Some Two-Dimensional Bluff Bodies with Moving-Belt Technique," *Journal of Wind Engineering and Industrial Aerodynamics*, **74-76**, pp. 511-519.

Klemperer, W., 1922, "Luftwiderstandsuntersuchungen an Automobilmodellen," *Zeitschrift für Flugtechnik und Motorluftschiffahrt*, 13, pp. 201-206.

Koenig-Fachsenfeld, R., 1951, Aerodynamik des Kraftfahrzeugs, Umschau Verlag, Frankfurt.

Krajnovic, S., and Davidson, L., 2001a, "Large Eddy Simulation of the Flow Around a Three Dimensional Bluff Body," AIAA Paper 2001-0432, 39th Aerospace Sciences Meeting & Exhibition, Reno, NV.

Krajnovic, S., and Davidson, L., 2001b, "Large-Eddy Simulation of the Flow Around a Ground Vehicle Body," SAE Paper 2001-01-0702, SAE World Congress, Detroit, MI.

Landman, D., 2000, "Road Simulation for NASCAR Vehicles at the Langley Full-Scale Tunnel," SAE Paper 2000-01-3550, Motorsports Engineering Conference & Exposition, November, Dearborn, MI.

Landman, D., and Britcher, C. P., 1998, "Development of Race Car Testing at the Langley Full-Scale Tunnel," SAE Paper 983040, Motorsports Engineering Conference & Exposition, Dearborn, MI.

Lanser, W. R., Ross, J. C., and Kaufman A. E., 1991, "Aerodynamic Performance of a Drag Reduction Device on a Full-Scale Tractor/Trailer," SAE Paper 912125, International Congress and Exposition, Detroit, MI.

Launder, B.E., Reece, G.J., and Rodi, W., 1975, "Progress in the developments of a Reynolds-stress turbulence closure". *J. Fluid Mechanics*, 68, pp.537-566.

Lay, W.E., 1933, "Is 50 Miles per Gallon Possible with Correct Streamlining," *SAE Journal*, 32, pp. 144-156 and 177-186.

Mason, W. T., 1975, "Wind Tunnel Development of the Dragfoiler – A System for Reducing Tractor-Trailer Aerodynamic Drag," SAE Paper 750705.

McCallen, R., Flowers, D. L., Dunn, T. A., Salari, K., Rutledge, W. H., Ross, J. T., Heineck, Bell, J. H., and Browand, F., 2000, "Aerodynamic Drag of Heavy Vehicles (Class 7-8): Simulation, Experimental Validation, and Development of an Aerodynamic Device," SAE Paper 2000-01-2209, Government/Industry Meeting, Washington, DC.

McLandress, A. S., Wiese, W., Turney, J., and Loczi, J., 2001, "A Two-Dimensional External Aerodynamics Tool (EAT) for Simulating Airflow around Tractor-Trailer Combinations," SAE Paper 2001-01-2743, International Truck and Bus Meeting and Exhibition, Chicago, IL.

Modi, V. J., Ying, B., and Yokomizo, T., 1992, "Effect of Momentum Injection and Fences on the Drag of a Tractor-Trailer Tuck Configuration," AIAA-92-2640-CP, 10th AIAA Applied Aerodynamics Conference, Palo Alto, CA.

Morel, T., 1978, "Aerodynamic Drag of Bluff Body Shapes Characteristic of Hatch-Back Cars," SAE Paper 780267.

Okumura, K., and Kuriyama, T., 1995, "Practical Aerodynamic Simulations (CD, CL, CYM) Using a Turbulence Model and 3rd-Order Upwind Scheme," SAE Paper 950629, International Congress and Exposition, Detroit, MI.

Perzon, S., Janson, J., and Hoglin, L., 1999, "On Comparisons Between CFD Methods and Wind Tunnel Tests on a Bluff Body," SAE Paper 1999-01-0805, International Congress and Exposition, Detroit, MI.

Ramnefors, M., Perzon, S., and Davidson, L., 1994, "Accuracy in Drag Predictions on Automobiles," Conference on Vehicle Aerodynamics, Loughborough University of Technology, UK.

Rhie, C. M., and Chow, W. L., 1982, "A Numerical Study of the Turbulent Flow Past an Isolated Airfoil with Trailing Edge Separation," *AIAA Journal*, 21, No. 11, pp. 1525-1532.

Sims-Williams, D. B., and Dominy, R. G., 1998, "Experimental Investigation into Unsteadiness and Instability in Passenger Car Aerodynamics," SAE Paper 980391, International Congress & Exposition, Detroit, MI.

Sorrells, M.C., 1999, Private communications, Volvo Trucks of North America, Greensboro, NC.

Speziale, C.G., Sarkar, S., and Gatski, T.B., 1991, "Modelling the pressure-strain correlation of turbulence: an invariant dynamical systems approach" *J. Fluid Mechanics*, Vol. 277, pp. 245-272.

Sumantran, V., and Han, T., 1995, Investigations into Vehicle Aerodynamics, SP-1078, Society of Automotive Engineers, Inc.

Summa J. M., 1992, "Steady and Unsteady Computational Aerodynamics Simulations of the Corvette ZR-1," SAE Paper 921092, SAE International Congress, Detroit; MI.

Yakhot V., and Orszag S. A., 1986, "Renormalization Group Analysis of Turbulence," *Journal of Scientific Computing*, 1, pp. 3-51.

APPENDIX A

PARALLEL COMPUTATION EFFICIENCY

Numerical calculations in this dissertation were conducted on a Sun HPC 10000 supercomputer and a 12-CPU PC cluster. The following figures present the performance of these computer systems. Parallel computation performance was calculated using PMB software from Pallas. More information about benchmark procedure can be obtained from ftp://ftp.pallas.de/pub/PALLAS/PMB/PMB-MPI1.pdf.

Compared Systems:

PC, 933 MHz CPU, (MPICH) and Sun HPC 10000, 400 MHz CPU, (Sun MPI),
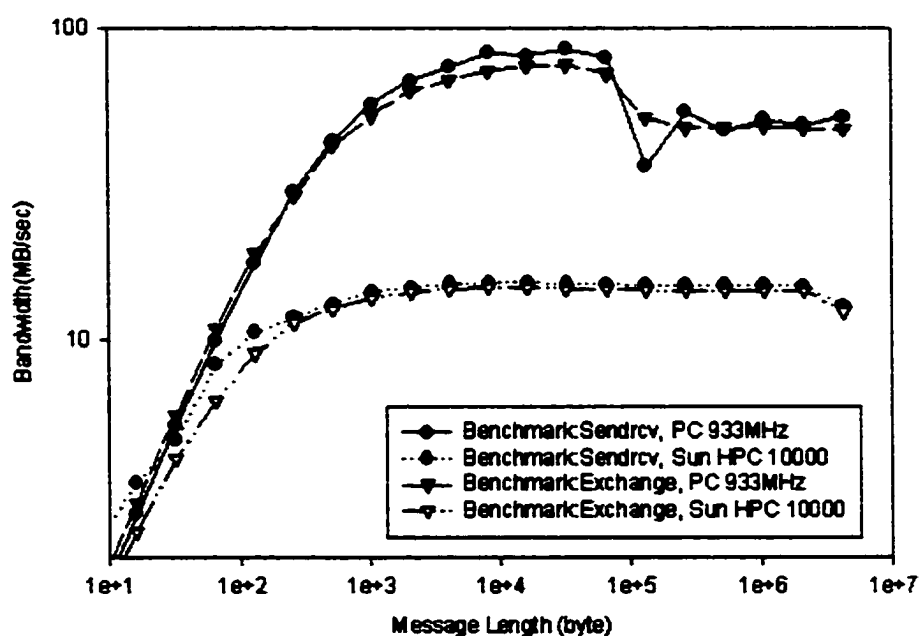
Figure A.1 Send-receive and exchange benchmark results (message length versus bandwith).
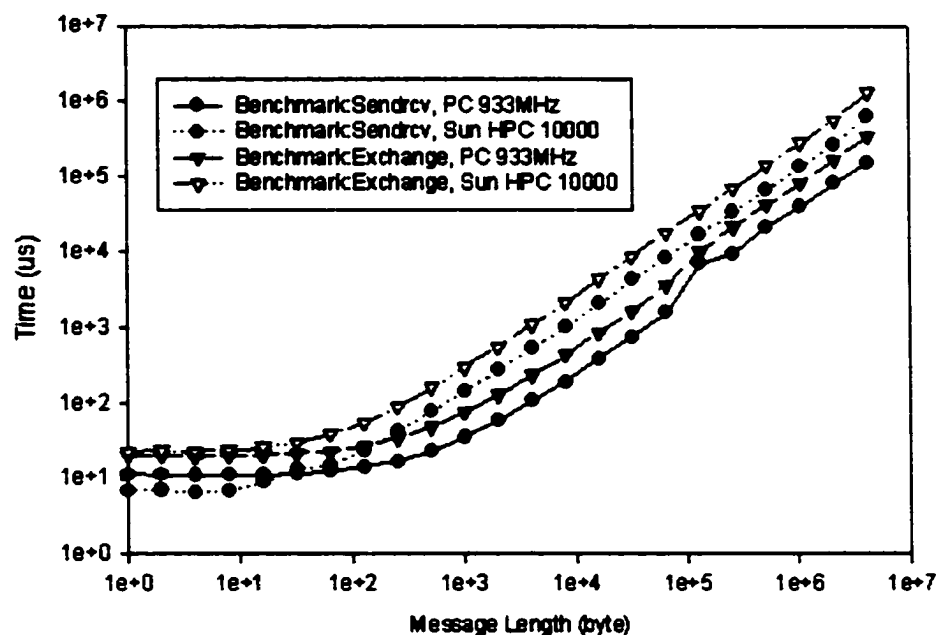
Figure A.1 MPI_Send-receive and Exchange communication benchmark results (message length versus communication time).
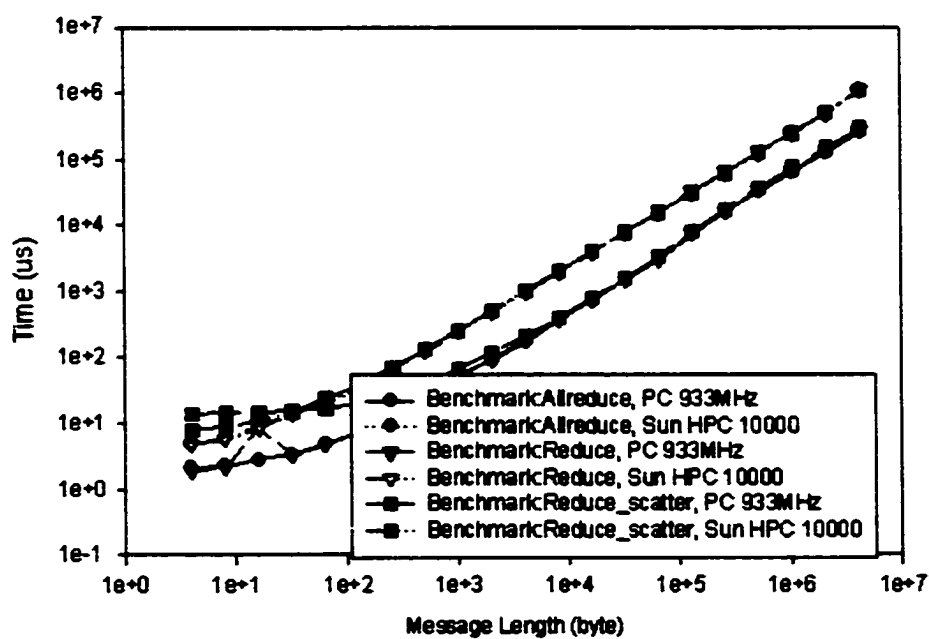

Figure A.2 MPI_Allreduce, MPI_Reduce and MPI_Reduce scatter function benchmark results (message length versus communication time).
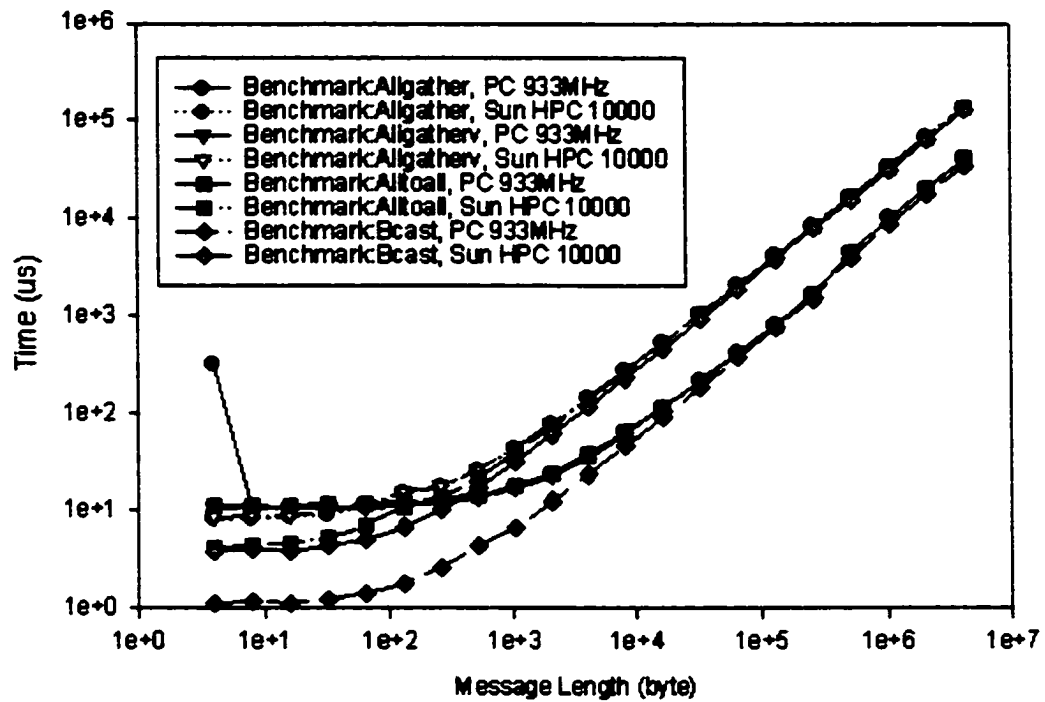
Figure A.3 MPI_Allgather, MPI_Allgatherv, MPI_All-to-all and MPI_Broadcast benchmark results (message length versus communication time).

APPENDIX B

AERODYNAMIC DEVICES – FEDERAL REGULATIONS

Federal Register: August 18, 2000 (Volume 65, Number 161)
Section: Proposed Rules
Agency: FEDERAL HIGHWAY ADMINISTRATION
Title: Truck Length and Width Exclusive Devices
Action: Notice of proposed rulemaking (NPRM); request for comments.
Page: 50471-50479
FEDERAL HIGHWAY ADMINISTRATION
DEPARTMENT OF TRANSPORTATION 23 CFR Part 658
[FHWA Docket No. 1997-2234 (formerly 87-5 and 89-12)] RIN 2125-AC30
Truck Length and Width Exclusive Devices
AGENCY: Federal Highway Administration (FHWA), DOT.

ACTION: Notice of proposed rulemaking (NPRM); request for comments. SUMMARY: The FHWA is requesting comments on proposed criteria for excluding safety or efficiency enhancing devices from measurement of vehicle length and width.

Background

Section 411(h)of the Surface Transportation Assistance Act of 1982 (STAA) (Public Law 97-424, 96 Stat. 2097) gave the Secretary of Transportation (Secretary) authority to exclude from the measurement of vehicle length any safety and energy conservation devices found necessary for the safe and efficient operation of commercial motor vehicles (CMVs). That authority is now codified at 49 U.S.C. 31111(d). Section 416(b), now 49 U.S.C. 31113(b), authorized similar exclusions when measuring vehicle width. Section 411(h) also provided that no device excluded from length measurement by the Secretary could have, by design or use, the capability to carry cargo.

Since enactment of the STAA, four Federal Register notices have identified some 55 devices as length or width exclusive. Copies of all of them are available on-line under the FHWA docket number cited at the beginning of this document. (See 52 FR 7834, March 13, 1987; 54 FR 52591, December 26, 1989; 55 FR 10468, March 21, 1990; and 55 FR 25673, June 22, 1990.)

Prior to 1979, the FHWA operated under an administrative definition of the term "vehicle" that included the main structure of the vehicle with attachments unless an exception or tolerance was allowed by State law as of July 1, 1956. The width limit for trucks and buses at that time was 96 inches (2.44 meters) on the Interstate System, as established by the Federal-Aid Highway Act of 1956 (Public Law 84-627, 70 Stat. 374, at 381). However, it was the practice of the States to

allow certain exceptions to that limit for mirrors, hand holds, and turn signals. The maximum width limit of buses was increased from 96 inches (2.44 meters) to 102 inches (2.6 meters) by the Federal-Aid Highway Act of 1976 (Public Law 94-280, 90 Stat. 425, at 438).

The States' practice of allowing exceptions to the width limit was acknowledged and endorsed in the American Association of State Highway Officials' (AASHO) 1963 "Recommended Policy on Maximum Dimensions and Weights of Motor Vehicles to be Operated Over the Highways of the United States." Width was defined as follows:

Width: The total outside transverse dimension of a vehicle including any load or load-holding devices thereon, but excluding approved safety devices and tire bulge due to load. This definition

has been part of AASHO, now the American Association of State Highway and Transportation Officials (AASHTO), recommended practice since it was adopted in 1963.

The difference between the AASHO/AASHTO recommended policy and the FHWA's administrative interpretation generated inquiries which were answered in a Notice of Interpretation (NOI) published on June 28, 1979 (44 FR 37710). The FHWA adopted the AASHO/AASHTO definition of width and allowed the States to exclude certain safety devices from the measurement of a vehicle's width. These consisted of load-induced tire bulge, rearview mirrors, turn signal lamps, and hand holds for cab entry/egress. A subsequent NOI published on January 2, 1981 (46 FR 32), allowed States to expand the list of safety devices which could extend beyond the 96-inch (2.44-meter) load surface. A final rule published on June 5, 1984 (49 FR 23302) and codified in part 658, reiterated the FHWA's previous policy of allowing States to exclude from vehicle width measurements those safety devices that do not extend more than 3 inches (76 millimeters) from either side. The rule interpreted the 102-inch width limit to include its approximate metric equivalent of 2.6 meters. In addition, it defined length exclusive devises as all non-cargo carrying appurtenances at the front or rear of a CMV semitrailer or trailer whose function is related to the safe and efficient operation of the semitrailer or trailer. Two additional NOI's on length and width exclusive devices were issued on January 13, 1986, (51 FR 1367) and on March 13, 1987 (52 FR 7834). While these documents remain active, they simply represent FHWA's interpretations of statutory provisions and have no binding regulatory effect, either on the States or the motor carrier industry.

The January 13, 1986, NOI specifically excluded from any length measurement 6-inch and 8-inch (152mm and 203mm) front locking devices (bolsters) and a 12-inch (0.30-meter) rear lift tailgate in the "up" position. The NOI declined to exclude a 7-foot (2.13-meter) front trailer frame extension from length measurements on grounds that it was load bearing, but reiterated that this did not necessarily preclude its use because States could recognize it as a length exclusive device.

The March 13, 1987, NOI held that lift gates not over 24 inches (0.61 meters) from the rear of the trailer in the "up" position, B-train assemblies, and about 35 other devices qualified as length or width exclusive devices. It also provided that the width of a trailer be measured across the sidemost load-carrying structures, support members, and structural fasteners, and that the length of a semitrailer be measured from the front vertical plane of the foremost transverse load-carrying structure to the rear vertical of the rearmost traverse load-carrying structure.

The STAA required States to allow 102-inch (2.6-meter) wide CMVs on the National Network (NN). The NN consists of the Interstate System and other highways designated in 23 CFR part 658, appendix A. Hawaii, however, was allowed to keep its 108-inch (2.74-meter) width limit.

In addition, the STAA set minimum length limitations for semitrailers operating in a truck tractor-semitrailer combination on the NN. The States were required to allow semitrailers with a length of 48 feet (14.63-meters), unless the State allowed a longer semitrailer on December 1, 1982. In that case, the longer length was grandfathered and the State must continue to allow the use of semitrailers up to that length on the NN. A list of grandfathered semitrailer lengths is published in 23 CFR part 658, appendix B.

The minimum length limit for each semitrailer or trailer in a truck tractor-semitrailer-trailer combination was established at 28 feet (8.53 meters), or 28.5 feet (8.69 meters) if in legal operation on December 1, 1982, within an overall length of 65 feet (19.81 meters). States may not limit the overall length of a truck tractor semitrailer, or truck tractor-semitrailer-trailer combination, on the NN.

Pursuant to its authority under section 411(d) of the STAA, the FHWA designated several CMV combinations with unique characteristics as "specialized equipment" and established length parameters for their operation on the NN. The most common of these specialized vehicles are automobile transporters. Minimum length limits established include 65 feet (19.81 meters) for standard automobile transporters and 75 feet (22.86 meters) for stinger steered units, i.e., the fifth wheel is located on a drop frame located behind and below the rear-most axle of the power unit.

Boat transporters are also allowed the same lengths based on the fifth wheel connection location. In addition, all automobile and boat transporters are allowed cargo overhangs of up to 3 feet (0.91 meters) in front of the truck tractor and 4 feet (1.22 meters) beyond the rear of the semitrailer.

Other combinations considered specialized equipment include truck tractor-semitrailer-semitrailer vehicles with a "B-train" connection, Maxi-cubes, and beverage semitrailers. The length requirements established for these combinations are described in 23 CFR 658.13.

The Intermodal Surface Transportation Efficiency Act of 1991 (ISTEA), Public Law 102-240, 105 Stat. 1914, established a minimum length limit for buses of 45 feet (13.72 meters) on the NN. There are no Federal laws or regulations regarding the length of straight trucks.

The ISTEA also prohibited the States from allowing the cargo-carrying units of CMVs with two or more such units to exceed the length allowed and in actual use on the NN on June 1, 1991. It also provided that the length of the cargo-carrying units is to be measured from the front of the first unit to the rear of the last unit. These provisions did not affect the authority of the Secretary to exclude devices from the measurement of length and width if the vehicles are subject to Federal size requirements.

Today's proceeding was originally initiated through an advance notice of proposed rulemaking (ANPRM) issued on December 26, 1989 (54 FR 52951), which requested information on a series of issues. The comment period, originally established at 90 days, was subsequently extended to August 21, 1990 (55 FR 25673). After considering the comments received in response to the ANPRM, the statutory language on length and width exclusive devices in 49 U.S.C. 31111(d), 31113(b), and developments in the industry since 1990, the FHWA is proposing regulatory changes to 23 CFR part 658. The FHWA is requesting comments on proposed criteria for excluding safety or efficiency enhancing devices from measurement of vehicle length and width.

In 1997, the FHWA rearranged its docket system in accord with the electronic system adopted by the Department of Transportation. A new docket was established to receive the information with the number FHWA Docket 1997-2234. Material previously submitted to Docket Nos. 87-5 and 89-12 was transferred and scanned into FHWA Docket 1997-2234.

Sixty-eight comments were submitted in response to the ANPRM (FHWA Docket Nos. 87-5 and 89-12). Those commenting fell into the following groups: States--17, automobile transporter companies--14, trade associations--6, trailer manufacturers--5, bus and truck manufacturers--4, tarp and tarp hardware manufacturers--3, individuals--3, port authorities--1, carpet manufacturer--1, walkway and platform manufacturers--1, employees union--1, U.S. Government agencies--1, and comments relating to extending the comment period--2. Several respondents commented more than once. Questions in the ANPRM and Comments from Respondents from the measurement of length and width of vehicles would be necessary.

Further details can be found on the following website:

http://fr.cos.com/cgi-bin/getRec?id=20000818a19

APPENDIX C

REYNOLDS AVERAGING

Like laminar flow, turbulence is governed by the unsteady Navier-Stokes equations. Turbulence consists of small-scale fluctuations in the flow characteristics over time. It is a complex process, mainly because it is three dimensional, unsteady and chaotic, and it can have a significant effect on the characteristics of the flow.

Turbulence occurs when the inertia forces in the fluid become significant compared to viscous forces, and is characterized by a high Reynolds number.

Turbulence generally involves length scales much smaller than the smallest finite volume mesh, which can be practically used in a numerical analysis. To resolve the features of the flow at this level directly would require, even in the simplest cases, an extremely large number of small mesh elements. Although direct numerical simulation (DNS) of the unsteady flow equations is possible for very simple cases, for most practical cases it is not performed due to current limits on computer memory and processor speed.

To enable the effects of turbulence to be predicted, a large amount CFD research has concentrated on methods that make use of turbulence models. Turbulence models have been specifically developed to account for the effects of turbulence without recourse to a prohibitively fine mesh. In general, turbulence models seek to modify the governing equations by inclusion of additional terms or equations to account for turbulence effects.

A number of models have been developed that can be used to approximate turbulence. Some have very specific applications, while others can be applied to a wider class of flows with a reasonable degree of confidence.

Turbulence models solve transport equations for the Reynolds averaged quantities. For example, a velocity U may be divided into an average component, U, and a time varying component, u, in the following way:

$$U = \overline{U} + u \quad \text{where} \quad \overline{U} = \frac{1}{\Delta t} \int_t^{t+\Delta t} U dt \qquad \text{(C.1)}$$

and Δt is a time scale large relative to the turbulent fluctuations, but small relative to the time scale to which the equations are solved.

In the following equations, the bar is dropped for time-averaged quantities, except for products of fluctuating quantities. By substituting the time-averaged quantities, the Reynolds averaged equations then become:

$$\frac{\partial \rho}{\partial t} + \nabla \bullet (\rho U) = 0 \qquad \text{(C.2)}$$

$$\frac{\partial \rho U}{\partial t} + \nabla \bullet (\rho U \otimes U) = \nabla \bullet (\sigma - \overline{u \otimes u}) + S_M \qquad \text{(C.3}$$

$$\frac{\partial \rho \Phi}{\partial t} + \nabla \bullet (\rho U \Phi) = \nabla \bullet (\Gamma \nabla \Phi - \overline{\rho u \Phi}) + S_E \qquad \text{(C.4)}$$

The continuity equation has not been altered, but the momentum and scalar transport equations contain turbulent flux terms additional to the molecular diffusive fluxes. These are the Reynolds stress, $\overline{\rho u \otimes u}$, and the Reynolds flux, $\overline{\rho u \phi}$. These terms arise from the non-linear convective term in the un-averaged equations, not the linear diffusive one. They reflect the fact that convective transport due to turbulent velocity fluctuations will act to enhance mixing over and above that caused by thermal fluctuations at the molecular level. At high Reynolds numbers, turbulent velocity fluctuations occur over a length scale much larger than the mean free path of thermal fluctuations, so that the turbulent fluxes are much larger than the molecular fluxes.

Turbulence models close the Reynolds-averaged equations by providing models for the computation of the Reynolds stresses and Reynolds fluxes. So, turbulence models can be broadly divided into two classes: eddy viscosity models and Reynolds stress models.

In eddy viscosity models, the Reynolds stresses and fluxes are modeled algebraically in terms of known mean quantities. The eddy viscosity hypothesis assumes that the Reynolds stresses can be linearly related to the mean velocity gradients, in a manner analogous to the relationship between the stress and strain tensors in laminar Newtonian flow:

$$-\rho \overline{u \otimes u} = -\frac{2}{3}\rho k \delta - \frac{2}{3}\mu_t \nabla \bullet U \delta + \mu_t \left(\nabla U + (\nabla U)^T \right) \tag{C.5}$$

Here, μ_t is the eddy viscosity or turbulent viscosity. This has to be prescribed.

Analogous to the eddy viscosity hypothesis is the eddy diffusivity hypothesis, which states that the Reynolds fluxes of a scalar are linearly related to the mean scalar gradient:

$$-\rho \overline{u \phi} = \Gamma_t \nabla \phi \tag{C.6}$$

Here, Γ_t is the eddy diffusivity, and this has to be prescribed. The eddy diffusivity can be written:

$$\Gamma_t = \frac{\mu_t}{Pr_t} \tag{C.7}$$

where Pr_t is the turbulent Prandtl number. Eddy diffusivities are then prescribed using the turbulent Prandtl number. Subject to these hypotheses, the Reynolds averaged momentum and scalar transport equations become:

$$\frac{\partial \rho U}{\partial t} + \nabla \bullet (\rho U \otimes U) = B - \nabla p' + \nabla \bullet \left(\mu_{eff} \left(\nabla U + (\nabla U)^T \right) \right) \tag{C.8}$$

$$\frac{\partial \rho \phi}{\partial t} + \nabla \bullet \left(\rho U \phi - \Gamma_{eff} \nabla \phi \right) = S \tag{C.9}$$

where μ_{eff} is the Effective Viscosity, and Γ_{eff} is the Effective Diffusivity, defined by,

$$\mu_{eff} = \mu + \mu_t \tag{C.10}$$

and,

$$\Gamma_{eff} = \Gamma + \Gamma_t \tag{C.11}$$

and p' is a modified pressure, defined by:

$$p' = p + \frac{2}{3}\rho k + \nabla \bullet U\left(\frac{2}{3}\mu_{eff} - \zeta\right) \tag{C.12}$$

The Reynolds averaged energy equation becomes:

$$\frac{\partial(\rho h)}{\partial t} - \frac{\partial P}{\partial t} + \nabla \bullet \rho U h_{tot} = \nabla \bullet \left(\lambda\nabla T + \frac{\mu_t}{Pr_t}\nabla h\right) + S_E \tag{C.13}$$

Note that although the transformation of the molecular diffusion term may be inexact if enthalpy depends on variables other than temperature, the turbulent diffusion term is correct, subject to the eddy diffusivity hypothesis. Moreover, as turbulent diffusion is usually much larger than molecular diffusion, small errors in the latter can be ignored.

The Reynolds averaged transport equation for additional variables (non-reacting scalars) becomes:

$$\frac{\partial\rho\Phi}{\partial t} + \nabla \bullet \left(\rho U\Phi - \left(\Gamma_\Phi + \frac{\mu_t}{\sigma_\Phi}\right)\nabla\Phi\right) = S \tag{C.14}$$

Eddy viscosity models are distinguished by the manner in which they prescribe the eddy viscosity and eddy diffusivity.

Reynolds stress turbulence models solve an equation for the transport of Reynolds stresses in the fluid. Algebraic Reynolds stress models solve an algebraic equation for the Reynolds stresses, whereas differential Reynolds stress models solve a differential equation.

The Reynolds averaged momentum equations for the mean velocity are:

$$\frac{\partial \rho U}{\partial t} + \nabla \bullet (\rho U \otimes U) - \nabla \bullet (\mu \nabla U) = -\nabla p'' - \nabla \bullet (\rho \overline{u \otimes u}) + B \qquad \text{(C.15)}$$

where p'' is a modified pressure, B is the sum of body forces and the fluctuating Reynolds stress contribution is $\rho \overline{u \otimes u}$. Unlike eddy viscosity models, the modified pressure has no turbulence contribution and is related to the static (thermodynamic) pressure by:

$$p'' = p + \nabla \bullet U \left(\frac{2}{3}\mu - \zeta\right) \qquad \text{(C.16)}$$

In the differential stress model, $\overline{u \otimes u}$ is made to satisfy a transport equation. A separate transport equation must be solved for each of the six Reynolds stress components of $\rho \overline{u \otimes u}$. The differential equation Reynolds stress transport is:

$$\frac{\partial \rho \overline{u \otimes u}}{\partial t} + \nabla \bullet (\rho \overline{u \otimes u} \otimes U) - \nabla \bullet \left(\rho C \frac{k}{\varepsilon} \overline{u \otimes u} (\nabla \overline{u \otimes u})^T\right) = P + G + \phi - \frac{2}{3}\rho \varepsilon \delta \text{ (C.17)}$$

where P and G are shear and buoyancy turbulence production terms of the Reynolds stresses respectively, ϕ is the pressure-strain tensor and C is a constant. Next, let look at the Reynolds stress models (RSM).

These models do not use the eddy viscosity concept, but use transport equations for the individual Reynolds stresses. The Reynolds stress model transport equations are solved for the individual stress components.

Reynolds stress models are more suited to flows where the strain fields are complex, and reproduce the anisotropic nature of turbulence itself. They are particularly useful where there is strong flow curvature, separation or swirl.

Their general use has been limited because of the additional number of equations requiring solution and hence additional loads on computational resources and subsequent

increases in solution times. They are also less numerically robust than the previously described eddy viscosity models.

In the differential Reynolds stress model, differential transport equations are solved individually for each Reynolds stress component. The exact production term and the inherent modelling of stress anisotropies give superior results for flows with streamline curvature and in rotating systems.

The CFD solver calculates the following equations for the transport of the Reynolds stresses:

$$\frac{\partial \rho \overline{u \otimes u}}{\partial t} + \nabla \bullet \left(\rho U \otimes \overline{u \otimes u} \right) = P + \phi - \left[\nabla \bullet \left(\left(\mu + \frac{2}{3} c_s \rho \frac{k^2}{\varepsilon} \right) \nabla \right) \right] \bullet \left(\rho \overline{u \otimes u} \right) - \frac{2}{3} \rho \varepsilon \delta \quad \text{(C.18)}$$

which can be written in index notation as

$$\frac{\partial}{\partial t} \left(\rho \overline{u_i u_j} \right) + \frac{\partial}{\partial x_k} \left(U_k \rho \overline{u_i u_j} \right) = P_{ij} + \phi_{ij} + \frac{\partial}{\partial x_k} \left[\left(\mu + \frac{2}{3} c_s \rho \frac{k^2}{\varepsilon} \right) \frac{\partial \rho \overline{u_i u_j}}{\partial x_k} \right] - \frac{2}{3} \delta_{ij} \varepsilon \rho \quad \text{(C.19)}$$

where ϕ is the pressure-strain correlation, and P, the exact production term, is given by:

$$P = -\rho \left(\overline{u \otimes u} (\nabla U)^T + (\nabla U) \overline{u \otimes u} \right) \quad \text{(C.20)}$$

As the turbulence dissipation appears in the individual stress equations, an equation for ε is still required. This now has the form:

$$\frac{\partial \rho \varepsilon}{\partial t} + \nabla \bullet \left(\rho U \varepsilon \right) = \frac{\varepsilon}{k} \left(c_{\varepsilon 1} P - c_{\varepsilon 2} \rho \varepsilon \right) + \nabla \bullet \left[\frac{1}{\sigma_{\varepsilon RS}} \left(\mu + \rho C_{\mu RS} \frac{k^2}{\varepsilon} \right) \nabla \bullet \varepsilon \right] \quad \text{(C.21)}$$

In these equations, the anisotropic diffusion coefficients of the original models are replaced by an isotropic formulation, which increases the robustness of the Reynolds stress model. The model constants are listed below for each model.

One of the most important terms in Reynolds stress models is the pressure-strain correlation, ϕ.

The pressure strain correlations can be expressed in the general form

$$\phi = \phi_1 + \phi_2 \tag{C.22}$$

where

$$\phi_1 = -\rho\varepsilon\left(C_{s1}a + C_{s2}\left(aa - \frac{1}{3}a\bullet a\delta\right)\right) \tag{C.23}$$

$$\phi_2 = -C_{r1}Pa + C_{r2}\rho kS - C_{r3}\rho kS\sqrt{a\bullet a} +$$
$$C_{r4}\rho k\left(aS^T + Sa^T - \frac{2}{3}a\bullet S\delta\right) + C_{r5}\rho k\left(aW^T + Wa^T\right) \tag{C.24}$$

and

$$a = \frac{\overline{u\otimes u}}{k} - \frac{2}{3}\delta \tag{C.25}$$

$$S = \frac{1}{2}\left(\nabla U + (\nabla U)^T\right) \tag{C.26}$$

$$W = -\frac{1}{2}\left(\nabla U - (\nabla U)^T\right) \tag{C.27}$$

In this formulation, a is the anisotropy tensor, S is the strain rate and W is the vorticity. This general form can be used to model linear and quadratic correlations by using appropriate values for the constants. The model constants are listed below.

There are three different Reynolds stress models available in the solver. These are known as LRR-IP, LRR-QI and SSG. Each model has different model constants.

The LRR-IP and LRR-QI models were developed by Launder et al. (1975). "IP" stands for Isotropisation of Production, and "QI" stands for Quasi-Isotropic. In these

models, the pressure-strain correlation is linear. The LRR-IP model is a simpler version which is less accurate but a little more stable.

The SSG model was developed by Speziale et al. (1991). This model uses a quadratic relation for the pressure-strain correlation. The Table 3.1 below shows the values of the constants for each model.

Table C.1 Coefficient list for Reynolds Stress Models.

Model	$C_{\mu RS}$	$\sigma_{\epsilon RS}$	C_s	$C_{\epsilon 1}$	$C_{\epsilon 2}$	C_{s1}	C_{s2}	C_{r1}	C_{r2}	C_{r3}	C_{r4}	C_{r5}
LRR-IP	0.1152	1.10	0.22	1.45	1.90	1.8	0.00	0.0	0.8	0.00	0.600	0.600
LRR-QI	0.1152	1.10	0.22	1.45	1.90	1.8	0.00	0.0	0.8	0.00	0.873	0.655
SSG	0.1000	1.36	0.22	1.45	1.83	1.7	-1.05	0.9	0.8	0.65	0.625	0.200

CURRICULUM VITA

for

ILHAN BAYRAKTAR

DEGREES:

Master of Science (Mechanical Engineering), Istanbul Technical University,
Istanbul, TURKEY, March 1998
Bachelor of Science (Mechanical Engineering), Istanbul Technical University,
Istanbul, TURKEY, June 1995

PROFESSIONAL CHRONOLOGY

Department of Aerospace Engineering, Old Dominion University, Norfolk, Virginia.
Research Assistant, August 1998-present.
Environmental and Applied Fluid Dynamics Department, von Karman Institute for Fluid Dynamics,
Brussels, Belgium, Stagiare, March 1998- June 1998.
Department of Mechanical Engineering, Istanbul Technical University, Istanbul, Turkey.
Teaching & Research Assistant, June 1995-August 1998.

SCIENTIFIC AND PROFESSIONAL SOCIETIES MEMBERSHIP:

American Society of Mechanical Engineers (ASME)
American Institute of Aeronautics and Astronautics (AIAA)
Society of Automotive Engineers (SAE)

HONORS AND AWARDS:

"Plot of the Month," Amtec Engineering Inc., November 2001
"Dominion Scholarship," Old Dominion University, 2000
"Meritorious Service Award," ITU Alumni Association International, 1997
"Meritorious Service Award," ITU Alumni Association International, 1996

SCHOLARY ACTIVITIES COMPLETED:

- **Bayraktar, I.**, Durmaz, T., 2002, "Computational Study on Fluid Flow in Hyperbaric Chamber," ESDA2002-ATF053, 6th Biennial Conference on Engineering Systems Design and Analysis, Istanbul, Turkey.

- **Bayraktar, I.**, Landman, D. and Baysal, O., 2001, "Experimental and Computational Investigation of Ahmed Body for Ground Vehicle Aerodynamics," SAE-2001-01-2742, International Truck and Bus Meeting& Exposition, Chicago, IL.

- **Bayraktar, I.**, 2001, "Correlation Between External and Internal Pressure of Porous Box Placed in Turbulent Flow," FEDSM2001-18108, 2001 ASME Fluids Engineering Division Summer Meeting, New Orleans, LA.

- Baysal, O., and **Bayraktar, I.**, 2001, "Unsteady Wake Behind a Bluff Body in Ground Proximity," FEDSM2001-18208, 2001 ASME Fluids Engineering Division Summer Meeting, New Orleans, LA.

- Baysal, O., and **Bayraktar, I.**, 2000, "Computational Simulations for External Aerodynamics of Heavy Trucks," *SAE Transactions: Journal of Commercial Vehicles*, Vol. 109, Section 2, pp. 813-819.

- Baysal, O., and **Bayraktar, I.**, 2000, "Computational Simulations for External Aerodynamics of Heavy Trucks," SAE-2000-01-3501, International Truck and Bus Meeting& Exposition, Portland, OR.